Department of Exploration Geophysics

Borehole Seismic Methods in High Permeability Sandstone

Majed Ahmed Almalki

This thesis is presented for the Degree of
Doctor of Philosophy
of
Curtin University

November 2014

Declaration of Academic Integrity

To the best of my knowledge and belief this thesis contains no material previously published by any other person except where due acknowledgment has been made. This thesis contains no material which has been accepted for the award of any other degree or diploma in any university.

Signature:

Date: 20-2-2014

To my parents and my respected sisters and brothers.

Acknowledgements

I'm grateful to the many scientists who shared their time and knowledge with me during my PhD. As it would be hard to mention them all, indeed everyone who contributed has my sincere gratitude.

To King Abdulaziz City for Science and Technology KASCT, thank you for granting me a PhD scholarship. Many thanks to the Saudi Arabia Cultural Mission for nominating me for the excellency award during my PhD.

I would like to thank my supervisor Dr Brett Harris for accepting me into a research program supported by a grant from the Premiers Water Foundation (a joint research project including: The Water Corporation of Western Australia, CSIRO and Curtin University, with the Department of Water administering the project for the State of Western Australia). Throughout my PhD, Dr Brett Harris' suggestions and motivation have always been of great value. The field experimental work during my PhD would have not been possible without his assistance.

I am also very thankful to the thesis Chair, Professor Boris Gurevich, for reviewing my publication in *Geophysics*, as well for as his ongoing support. My research owes a lot to other members of my thesis committee too: Dr Anderj Bona, Dr Roman Pevzner and Dr Milovan Urosevic, who helped me out, especially with virtual source analysis. Also, my special, sincere gratitude goes to Dr Christian Dupuis, Dr Bruce Hartley and Dr Robert Galvin for their comments and constructive discussions.

I want to thank the Department of Water and the Water Corporation of Western Australia for providing the permeability data and screened casing specifications used in this thesis. I am thankful to G. Maesepp, S. Higginson, and M. Martin from the Department of Water and the Water Corporation of Western Australia for their technical assistance and to Moyra Wilson and Marala Garcia for their valuable analysis of the petrophysics and sedimentary structure of the core samples at cored hole NG3. I would like to express my appreciation to the Faculty of Graduate Studies Committee (FGSC) for financially supporting my attendance at the 73rd EAGE Conference in Vienna 2011. I would like to thank Curtin University for providing financial support for fieldwork, conference attendance and other project-related costs.

I am also grateful to other PhD students: Elmar Strobach, Andrew Greenwood, Bai Chun Sun, Putri Wisman, Eva Caspari, Faisal Alonaizi, Mamdoh AlAjmi, Abdulaziz AlAsbali, Yousuf AlJabri, Mehdi Asgharzadeh, Andrew Pethick, Sergei Tcherkashnev and Jamal Esttaifan for their strong motivation and a serene working environment.

I would like to express my gratitude to Mr Robert Verstandig for proofreading my thesis and to the secretarial and department staff: Melanie Troebinger, Rhiannon Howe, Deirdre Hollingsworth, Tanya Wallace, Judith Tournay and Jennifer McPherson for their continuous assistance.

List of Publications

Journals

Almalki, M., B. Harris, and C.J. Dupuis, 2013, Multifrequency full-waveform sonic logging in the screened interval of a large-diameter production well: Geophysics, **78** (5), B243-B257.

Almalki, M., B. Harris, and C.J. Dupuis, 2013, Field and synthetic experiments for virtual source crosswell tomography in vertical wells; Perth Basin, Western Australia: Journal of Applied Geophysics, **98**, 144-159.

Almalki, M., B. Harris, and C.J. Dupuis, 2013, Changes in P-wave velocity with different full waveform sonic transmitter centre frequency: for Exploration Geophysics.(Under Review)

Expanded Abstracts

Almalki, M., B. Harris, and C.J. Dupuis, 2010a, Seismic signature of high permeability sandstone: Perth Basin, Western Australia: 21st International Geophysical Conference and Exhibition, Extended Abstracts, Sydney, 1-4.

Almalki, M., B. Harris, and C.J. Dupuis, 2010b, Multi-frequency full waveform sonic in the screened interval of a large diameter production well: Curtin Reservoir Geophysics Consortium CRGC annual meeting, 10-11 December 2010, Rottnest Island, Western Australia.

Almalki, M., B. Harris, and J.C. Dupuis, 2011, Simultaneous Vertical Seismic Profiling in Two Wells and the Virtual Source Method; Perth Basin, Western Australia: 73rd EAGE conference and exhibition, F045.

Almalki, M., B. Harris, and C.J. Dupuis, 2011, 3D visualization and analysis of Stoneley wave velocity-frequency dependence in a large diameter screened well: Curtin Reservoir Geophysics Consortium CRGC annual meeting, 8-9 December 2011, Rottnest Island, Western Australia.

Almalki, M., B. Harris, and J.C. Dupuis, 2012, Numerical and field experiments for virtual source tomography, Perth Basin, Western Australia: 22nd International Geophysical Conference and Exhibition, Extended Abstracts, Brisbane, 1-4.

Almalki, M., B. Harris, and C.J. Dupuis, 2012, Stoneley wave dispersion in a high permeability sandstone; Perth Basin, Western Australia: 22nd International Geophysical Conference and Exhibition, Extended Abstracts, Brisbane, 1-4.

Almalki, M., B. Harris, and C.J. Dupuis, 2012, Case study of acoustic logging in a sand-screened production well: KACST-JCCP 1st Joint International Workshop for the Earth's Surface and Subsurface 4D Monitoring, Riyadh, Saudi Arabia.

Squelch, A., B. Harris, and M. Almalki, 2012, Estimating porosity from CT scans of high permeability core plugs: 22nd International Geophysical Conference and Exhibition, Extended Abstracts, Brisbane, 1-3.

Harris, B., C. Dupuis, M. Almalki, Q. Li, , M. Martin, and H. Prommer, 2010, Near Well Seismic Methods for Managed Aquifer Recharge; Perth Basin, Western Australia: 7th Annual International Symposium on Managed Aquifer Recharge ISMAR7, 9-13 October 2010, Abu Dhabi, United Arab Emirates.

Statement of candidate about the contribution of others

I am the main author for all the publications used as a part of this thesis. In all these papers, I am the principal investigator.

List of Additional Publications not Relevant to the Thesis

Al-Anezi, G.T., M. Almalki, and T. Alkhalifa, 2013. Mapping of bedrock using the high-resolution seismic reflection technique at Wadi Al Dawasir Region, Saudi Arabia: Arabian Journal of Geosciences, **6**, 235-245.

Almalki, M. and A. Al-Amri, 2013. Seismic zones regionalization and hazard assessment of SW Arabian Shield and Southern Red Sea Region. In: Lithosphere Dynamics and Sedimentary Basins: The Arabian Plate and Analogues, pp. 317-331. Springer, ISBN 364229278X.

Abstract

One of the challenges in both the oil and groundwater industries is to establish direct or indirect relationships between signals recorded by seismic methods and hydraulic parameters. There is some potential to address this challenge; however, the signals must be acquired with sufficient energy distribution over a wide range of frequencies. Development of new borehole seismic methods may pave the way to more robust links between seismic, mechanical and hydraulic properties for sandstone dominated sedimentary formations.

It is common for sandstone aquifers in many sedimentary basins around the world to be penetrated by thousands of wells. Borehole seismic methods have considerable, but often under-utilized, or unrealized, potential for application in these wells. This thesis tackles the challenge of developing new borehole seismic applications in high-permeability sandstone aquifers. Under this general theme, three particular areas of research are presented. In every case, research spans the full, acquisition, processing and interpretation workflow. The three research areas are: (i) multifrequency full waveform sonic logging (FWS) in sand-screened intervals of production wells, (ii) P-wave apparent dispersion analysis and (iii) virtual source crosswell tomography using dual well walkaway vertical seismic profiling (WVSP).

A further motivation for my research is to find field methods to extract value from the more esoteric rock physics and borehole seismic theories. In particular I have examined the practical short comings of dispersion analysis for the many wave modes generated during full waveform sonic logging. In addition, I have examined seismic interferometry as a method for recovering crosswell P-wave velocities between vertical well pairs using surface sources only. In each case, the challenge commenced with field acquisition. Field experiments often had to be completed within a limited time immediately after drilling in fragile sand-dominated formations prone to collapse. This is one reason why so little research of a practical nature can be found in the literature on the application of borehole seismic methods in weakly consolidated high-permeability sandstone aquifers.

The first of my field experiments consisted of repeated multifrequency full waveform sonic logging in both a simple open drill hole and a high-yield large

diameter production well completed with wire-wound sand screens at an aquifer storage and recovery site in Perth, Western Australia. Phase-shift transform methods were applied to obtain phase-velocity dispersion images for frequencies up to 4 kHz. Dispersion images from FWS logging in the large diameter sand-screened production well and the open hole were highly comparable. Sandstone and clay intervals presented with highly characteristic dispersion images for both leaky P and Stoneley wave modes in both the open hole and production well. A 3D representation of phase-velocity dispersion was developed to assist in the analysis of possible connections between low-frequency wave propagation modes and the distribution of hydraulic properties. The highest hydraulic conductivity intervals were typically correlated with the lowest phase velocities for the leaky P wave modes.

Multifrequency full waveform sonic logging was completed in an open cored drill hole penetrating weakly consolidated sandstone sediments immediately after drilling. Repeated logs were completed over the key interval with transmitter centre frequencies set to 1, 3, 5, and 15 kHz. Two sediment types (cross-bedded and non-cross-bedded sandstone) appeared to exhibit different empirical correlations between the apparent P-wave dispersion and permeability. This indicates that permeability in combinations of sedimentary structures may partially contribute to the apparent P-wave dispersion. In the end, there were many other factors that combined to dictate the apparent P-wave dispersion, and a rock physics model will be required to unravel the relative importance of these factors.

The final set of completed experiments included field and synthetic dual well walkaway vertical seismic profiling in vertical well pairs. The experiments were designed to test methods of obtaining crosswell velocity based on interferometry. The synthetic experiments highlight the potential of virtual source crosswell tomography, where large numbers of closely spaced receivers can be deployed in multiple wells. The field experiment was completed in two monitoring wells at an aquifer storage and recovery site near Perth, Western Australia. For this site, the crosswell velocity distribution obtained from inversion of travel times between in-hole virtual sources and receivers is highly consistent with what was expected from sonic logging and detailed zero-offset vertical seismic profiling. When compared to conventional walkaway vertical seismic profiling, the only additional effort required

to complete dual well walkaway vertical seismic profiling is the deployment of seismic sensors in the second well.

I have developed new borehole seismic techniques for assessing high-permeability sandstone aquifers between and in existing wells. The techniques that I presented would be highly suitable for time-lapse applications in high-volume production wells or for reassessing formation properties behind or between existing production and monitoring wells. The thousands of new and old wells that exist in large sedimentary basins are all amenable to the borehole seismic technologies that I have presented.

Contents

LIST OF FIGURES

LIST OF TABLES

CHAPTER 1 : Introduction

Borehole seismic methods are used in many applications. In particular they provide a valued and necessary means of calibrating surface seismic reflection methods for hydrocarbon exploration and production; however, they have not evolved as quickly for shallow applications or in high permeability sands or sandstones. These environments present new challenges and opportunities for the application of borehole seismic methods. For example, full waveform sonic data are rarely used and only in cases where P-wave velocity is recovered, usually by first break picking. However, I believe that the full wavetrain contains considerable untapped information about the mechanical and possibly hydraulic properties of the formation around the logged well. This thesis is concerned with the development of new borehole seismic applications for shallow (and often high permeability) settings. The most obvious application is for groundwater; however, the geothermal, geotechnical, and hydrocarbon industries (including unconventional gas) may also find the outcomes of my research highly beneficial.

A key part of this research is related to the development of borehole applications for groundwater and in particular, aquifer management. Aquifer storage and recovery is a rapidly growing research activity. As the fate of injected water sources can be critical, a higher level of aquifer characterisation is often required and therefore new borehole seismic methods for characterisation and monitoring are needed.

In Western Australia, the rapidly increasing population combined with very dry weather conditions during the last few decades have resulted in potential impacts on the sustainability of drinking water resources. After developing key understandings of the environmental and social aspects of this issue, the Western Australia government decided to use aquifer storage and recovery (ASR) strategies to manage and maintain groundwater capacity for future demands. This research is part of the Premier's Water Foundation grant, which is a joint research project that includes the Water Corporation of Western Australia, Commonwealth Scientific and Industrial Research Organisation (CSIRO) and Curtin University, with the Department of Water administering the project for Western Australia. At ASR sites, treated recycled water is injected into the aquifer during the wet season for later recovery during the summer. This research is firmly based on collecting and understanding complex

measurements at a range of frequencies from carefully selected field sites in the northern part of the city of Perth.

The first location is the Mirrabooka ASR trial site, which consists of five monitoring wells and one production well. The production well penetrated the key target interval of the Leederville Formation to a depth of 400 m and is made of plain-steel and sand-screen casing. The injection and extraction interval is in the Leederville Formation between depths of 300 and 400 m. This part of the aquifer consists of highly heterogeneous sandstone, claystone and siltstone sequences. The screened interval allows for investigation of the site heterogeneity and hydraulic parameters, which play a significant role in in-hole wave propagation.

The second field location is at the NG3 regional monitoring site. Here a core hole was drilled to penetrate the Yarragadee Formation at a depth of 200 m. Beds of weakly indurated sandstone and unconsolidated sand are encountered in this borehole. A number of methods are used to develop an understanding of the sedimentology of the formation, which include core analysis, permeability measurement and regional seismic surveys. These data provide a key input to the study of the P-wave velocities acquired at various frequencies.

During my research I conducted many in-situ borehole experiments. The outcomes and core research are presented in three chapters, which describe (i) multifrequency full waveform sonic (FWS) logging in a large diameter sand-screen production well, (ii) the analysis of apparent dispersion of P-wave velocity and (iii) virtual source crosswell tomography in vertical well pairs. Each chapter discusses the developments in both acquisition and processing for borehole seismic methods.

1.1 Motivation

There are thousands of wells around the world constructed using sand screens in both the groundwater and hydrocarbon industries. Production wells are installed to move fluids in or out of the ground. The efficiency with which a well performs these tasks can change with time and may depend on many factors. At the earliest stage in the lifecycle of a production well, immediately after installation of the casing but before development by airlifting or jetting, there are few methods that can be applied

to assess the mechanical and hydraulic properties in the near-well setting. A method that has potential is low-frequency FWS logging.

FWS data acquired using various transmitter central frequencies in sand-screen production wells may provide meaningful information for assessing the relationship between hydraulic conductivity and propagated wave modes. Clogging during ASR is a common risk. It may depend on (i) geochemical interactions between the injected water and formation sediments, (ii) biological fouling or (iii) precipitation from ions in solution onto the well screens. Clogging often has a strong dependence on entrance and exiting flow velocity (i.e., flow rate). Clogging may cause dramatic changes in near-well hydraulic conductivity and may result in a decrease in well efficiency. A time-lapse wireline logging method that has the potential to identify changes in the near-well environment in a completed production well may be of considerable value in understanding the rate and mechanisms associated with well clogging. This thesis will present new low-frequency wireline logging applications suitable for completed active production wells.

One of the challenges in the oil and groundwater industries is to establish relationships between wave propagation and hydraulic parameters. Often the most valuable result of applying geophysical methods to soft sediments is information regarding the formation's hydraulics. There is some potential to address this challenge with sonic borehole methods; however, the signals must be acquired with sufficient energy distribution over a wide range of frequencies. Furthermore, while the acquisition of P-wave velocity is considered routine, there are many reasons why P-wave velocity may vary with frequency. This calls into question the exact meaning of the P-wave velocity recovered by conventional methods. Studying the behaviour of P-waves in high permeability sandstone with various sedimentary structures will provide a new insight into what is superficially considered routine but, in detail, is complex. Such field studies are rare because weakly-consolidated sands, even flowing sands, collapsing formations and extremes in hydraulic conductivity, are ever present threats during the drilling and the logging processes. The integrity of the mud rotary drilled holes begins to deteriorate soon after the driller pulls the bit out of the hole. As a result, there is typically a short period of time in which FWS logging can be completed**.**

Sets of two or more vertical wells are commonly completed for production and monitoring. A cost-effective and low-impact method for determining the seismic velocity distribution between vertical wells would be of considerable interest to the groundwater, geothermal, geotechnical and conventional/unconventional hydrocarbon industries. As a potential solution, the application of seismic interferometry may offer new insight into the elimination of near-surface effects and significantly, opens up opportunities to acquire time-lapse signals. It is my intent to test the potential of a method of recovering crosswell velocity distribution that may assist in constraining the geometry of subsurface models required for hydraulic or reactive transport modelling. What may be achieved using crosswell tomography and seismic interferometry? To answer this question I explore the challenges and limitations of these techniques in both synthetic and field investigations.

1.2 Objectives

The main theme of my research concerns the development of new innovative practical borehole seismic applications in shallow sandstone environments. More specific objectives include:

i) To investigate application of low-frequency full-waveform sonic acquisition and processing methods within large diameter production wells over any intervals open to the formation (e.g., sand-screened intervals).

ii) To develop multifrequency FWS methods suitable for time-lapse monitoring of changes in the near-well setting.

iii) To develop new ways of processing and imaging phase velocity dispersion obtained from FWS data.

iv) To investigate the sensitivity of P-wave seismic velocities recovered from logging at different transmitter centre frequencies in shallow, weakly consolidated, high permeability and heterogeneous sandstones.

v) To investigate the potential application of seismic interferometry for recovering crosswell velocity distribution between vertical wells using only surface sources.

All the research activities work towards developing borehole seismic methods for subsurface characterisation or time-lapse monitoring of the near-well setting with a particular emphasis on their application at modern aquifer storage and recovery sites.

1.3 Organisation of the thesis

This thesis was organised in the same chronological sequence that the field experiments were completed. It is divided into six distinct chapters. The first chapter consists of an introduction describing the research problem and the objectives. For the benefit of readers, chapter 2 reviews key borehole seismic concepts including a description of wave modes generated during FWS logging, seismic interferometer (SI), crosswell tomography and simultaneous vertical seismic profiling techniques. Field experiments and research outcomes are described in the three subsequent chapters.

Research in the application of multifrequency full waveform sonic in (i) a sand-screened production well and (ii) an open drill hole is examined in chapter 3. The characterisation of the production interval, particularly by searching for possible correlations between hydraulic conductivity and FWS data, is also discussed. The dispersion images are used to identify characteristics of several wave propagation modes (e.g., leaky P and Stoneley waves) in the open hole and completed production well.

Chapter 4 considers differences in P-wave velocity recovered from full waveform sonic data obtained at various transmitter centre frequencies. I consider the possible correlation between apparent P-wave velocity dispersion and sandstone permeability within different sedimentary groupings. Chapter 5 describes synthetic and field experiments investigating the potential of virtual source crosswell tomography (VSCT) in pairs of vertical wells located in highly heterogeneous sandstone aquifers at an ASR site. The chapter describes the resolution of my VSCT method in coarse and thin horizontally layered models. Chapter 6 summarises research outcomes and provides conclusions from the present work. Finally, the appendix contains the copyright release information for the published papers presented in this thesis. Numerical and field data are archived at the Department of Exploration Geophysics, Curtin University.

CHAPTER 2 : Literature Review

Over the last few decades borehole seismic methods have rapidly developed to provide in-situ characterisation of formation properties. The seismic properties of shallow, slow formations differ substantially from those of hard rocks or deep consolidated formations. Low confining pressure, low levels of consolidations and formation heterogeneity are features of shallow formations. A number of borehole seismic techniques have been applied to shallow, high-permeability sandstone aquifers. In the remainder of this chapter I review the basic principles of the set of borehole seismic techniques relevant to my research program.

2.1 Full waveform sonic logging in slow formations

The FWS is a wireline logging tool that has been used for decades. Its techniques are commonly used in open boreholes (i.e., uncased). In this environment there is largely uninterrupted transmission of propagated waves from the tool to the formation. In practice, FWS logging often commences immediately after drilling is completed and before well completion. Typically three conditions are suggested for the successful acquisition of borehole compressional and shear head wave data (Paillet and Cheng, 1986):

i) The borehole diameter is less than or equal to the length of the acoustic wavelet.
ii) The distance between the source and receiver is 1 to 10 times the wavelet.
iii) The formation velocities (i.e., $\boldsymbol{V_p}$ and $\boldsymbol{V_s}$) are greater than the acoustic velocity of water $\boldsymbol{V_f}$, thus allowing acoustic waves to be critically refracted (Figure 2-1).

For example, the seismic wave travelling directly through the water column in the drill hole could potentially arrive before the critically refracted head wave if the hole diameter is large relative to the transmitter receiver offset. Also, the term slow formation often refers to the situations in which the compression wave velocity of the borehole fluid is higher than the shear velocity of the formation. In this case it is unlikely that the shear wave velocity can be directly recovered from full waveform

sonic records. However, the waveform in slow formations is composed of many wave modes that have potentially useful application in soft sediments. Such modes include the leaky P and Stoneley waves. I will briefly review these modes, emphasising insights into their possible applications.

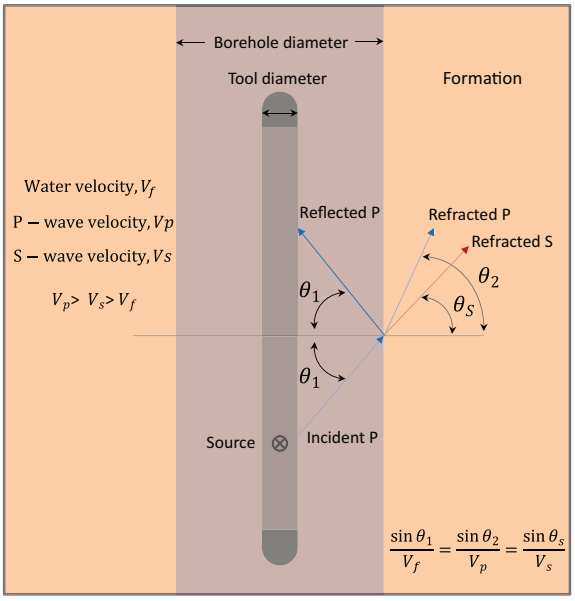

Figure 2-1. The reflection and refraction at the borehole wall and Snell's law. The velocity of sound in water V_f is less than the compressional wave V_p and shear wave V_s velocities in fast formations ($V_p > V_s > V_f$). θ_1 is the angle of incident and reflected compressional waves. θ_2 and θ_s are the angles of refracted compressional and shear waves respectively.

2.1.1 The leaky P mode

The leaky P mode is known from early earthquake studies by Oliver and Major (1960), who described this mode as a near-surface phenomenon that is normally dispersive. The particle motion of this mode is elliptical and its amplitude is no greater than one-fourth the amplitude of Rayleigh waves. The leaky P mode is not completely trapped within the waveguide in layered media. Thus, small amounts of wave energy escape into the underlying media with greater attenuation than that of normal modes (Oliver and Major, 1960). Figure 2-2 shows an early example of the

leaky P mode in a record of earthquake motion passing through deep oceanic crust (Oliver and Major, 1960). Oliver and Major (1960) found that the dispersion characteristic of this leaky mode can be used to estimate the thickness of the water-layer. For the example supplied by Oliver and Major (1960), the leaky P waves in Figure 2-2 begin approximately at time T = 01:10:51 GCT and continue until the arrival of Rayleigh waves.

In FWS experiments the identification of the leaky P mode in slow formations is important. The leaky P mode appears as complex borehole interference patterns on the waveform between the first arrival of P-waves and the Stoneley waves (Paillet and Cheng, 1986). A leaky P mode associated with the water-formation interface would be expected to dominate the borehole FWS.

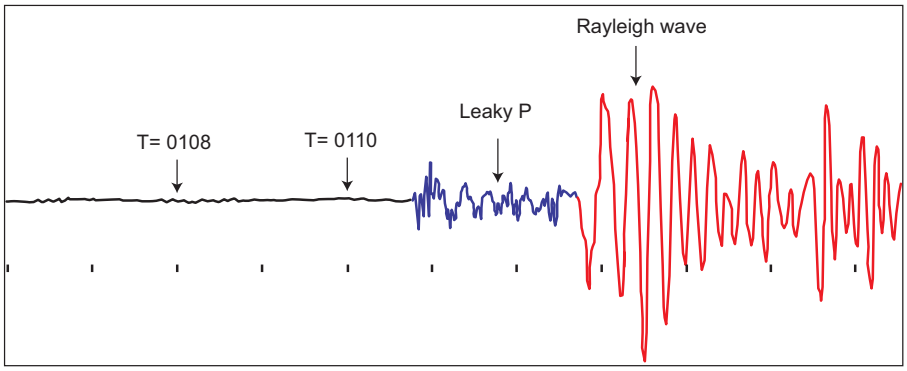

Figure 2-2. Seismogram showing the discovery of the leaky P mode from an earthquake recorded in Fiji in 1958, modified from Oliver and Major (1960).

The amplitude of the leaky P mode, as in the case of Stoneley waves, decays exponentially in the formation material. Cheng and Toksöz (1981) described the leaky mode in synthetic experiments. They indicated that the amplitude of the leaky mode is affected by two main factors including (i) the Poisson ratio of the formation and (ii) the source–receiver separation. The amplitude of the leaky mode is minimal in formations with a small Poisson's ratio of approximately 0.1 and is significant in formations with a Poisson's ratio greater than 0.3. Therefore, the leaky mode appears

to be of practical importance in estimating the shear wave velocity in slow formations. Paillet and Cheng (1986) reported that the amplitude of the leaky mode is slightly decreased if a wide source–receiver spacing of 3.66 m is used when compared to that using a smaller separation of 2.44 m. Thus, using a short-spacing acoustic FWS tool will be beneficial in recovering the energy and possibly information contained in the leaky P mode.

The recorded waveforms in large diameter production wells exhibit a complex pattern of leaky P modes. Figure 2-3 and 2-4 shows respectively, waveforms acquired by four receivers using a central transmitter frequency of 1 kHz and 3 kHz (Almalki et al., 2012). Both data sets were acquired at the same depth interval (345 m) in the Mirrabooka ASR production well. The leaky P mode appears immediately after the compressional head wave is created in the formation. It continues and exists along with the Stoneley wave that arrives later but typically with a larger spectral energy at a lower frequency. The frequency spectrum of these two data sets is displayed in Figure 2-5. Here, the acquisition of FWS data using a 3 kHz transmitter frequency exhibited higher spectral energy in the leaky mode compared to that from the waveform acquired using a frequency of 1 kHz. The maximum energy on the spectrum is associated with the Stoneley wave and is in a lower frequency band centre at approximately 1750 Hz. The spectrum consists of alternate peaks corresponding to leaky P modes at relatively high frequencies from 3100 and 4900 Hz. The characteristic of a leaky P wave mode together with a Stoneley wave is discussed in chapter 3.

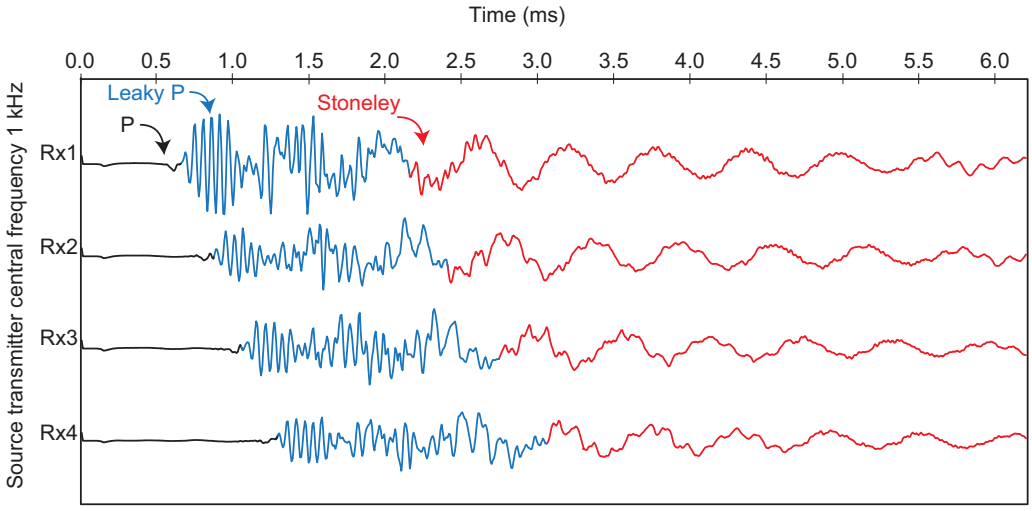

Figure 2-3. An example of waveforms acquired with four receivers (i.e., Rx1, Rx2, Rx3 and Rx4) using a transmitter centre frequency of 1 kHz in the production well at the Mirrabooka ASR site. The leaky P mode (blue) appears immediately after the compressional head wave and continues and exists along with the Stoneley wave arrivals (red).

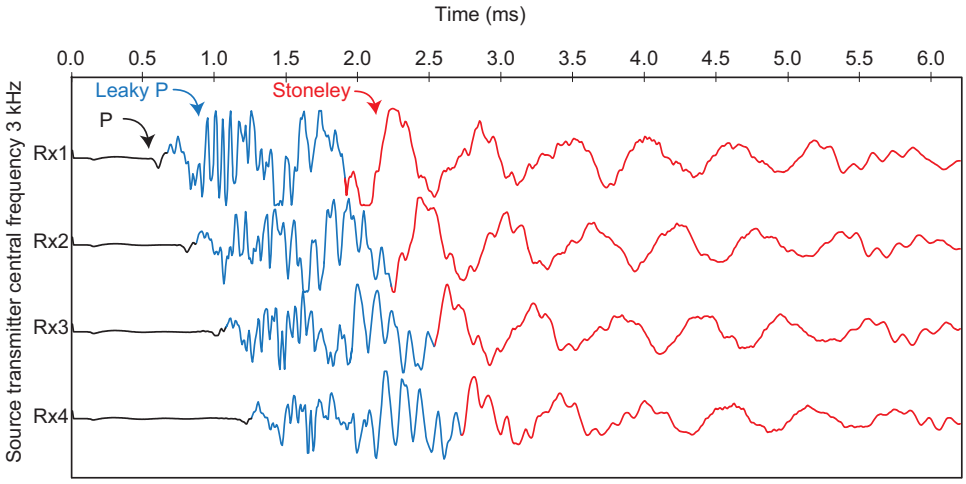

Figure 2-4. Waveforms acquired using the same configuration as in Figure 2-3 but with the transmitter centre frequency set to 3 kHz. The amplitude of the leaky P mode is increased as compared to the data set shown in Figure 2-3.

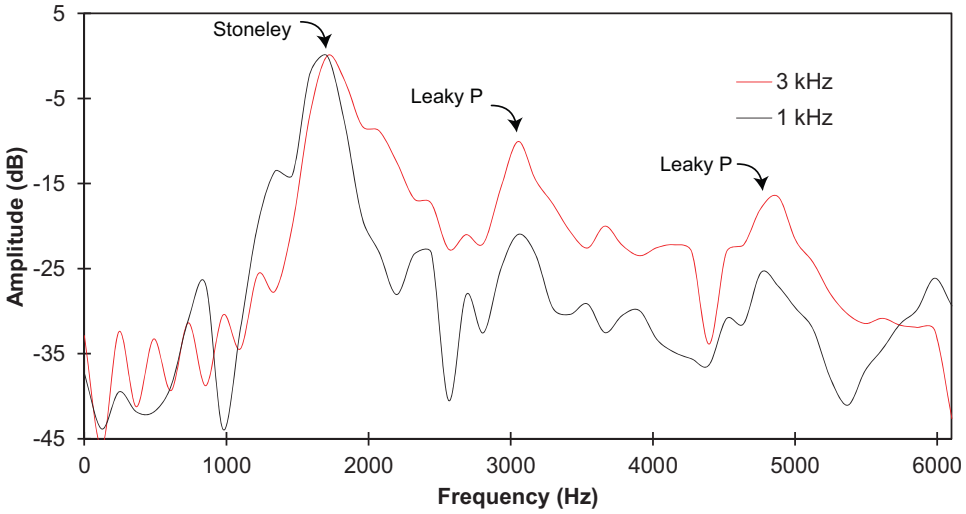

Figure 2-5. Frequency spectrum of FWS data acquired at the Mirrabooka aquifer storage and recovery site using a transmitter centre frequency of 1 and 3 kHz. The spectrum of FWS logging with a 3 kHz transmitter centre frequency exhibits higher energy for the leaky mode compared to FWS data acquired using a 1 kHz transmitter centre frequency.

2.1.2 Stoneley waves

Stoneley waves are a borehole-guided mode dominating the low-frequency band of FWS data. It is a dispersive mode propagating along the fluid–formation interface and has amplitude that attenuates exponentially in the formation. Stoneley waves have a phase and group velocity that is approximately 0.9 of the P-wave velocity in the fluid in fast formations (Cheng and Toksöz, 1981). Particle displacement of the Stoneley waves in the axial direction is much larger in the fluid column than in the formation and the axial displacement is discontinuous across the fluid–well boundary (Hardage, 1985). In contrast, radial displacement is continuous across the boundary and its amplitude decays exponentially in the formation (Hardage, 1985). While the sonic source is emitting waves in a fluid-filled borehole, the fluid column will compress and generate a piston-like motion (Bakulin et al., 2008). As a result the fluid will penetrate into the permeable formation, affecting both the velocity and amplitude of the Stoneley waves. Figure 2-6 shows a schematic of the elliptical particle motion of Stoneley waves in the open hole and completed sand-screened

production well at the Mirrabooka ASR site. The production well has a much larger diameter than the monitoring well, which affects the particle motions of the Stoneley waves and their propagation.

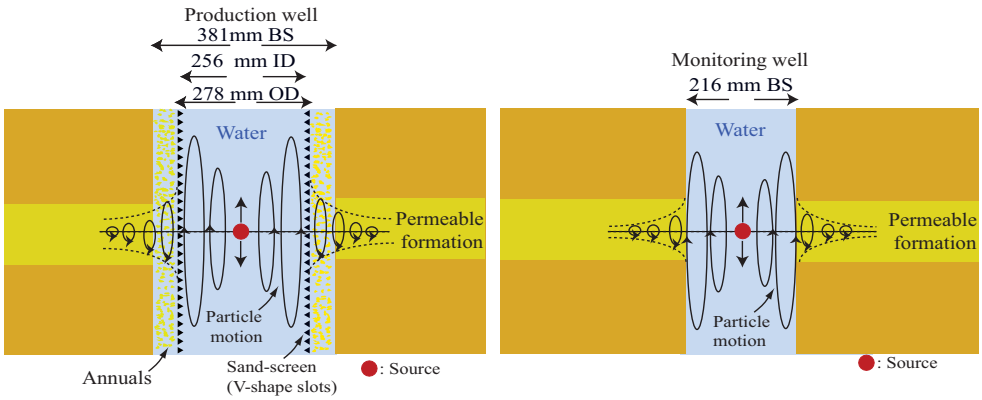

Figure 2-6. Schematic showing the elliptical particle motion of Stoneley waves in (a) the large diameter production well M345-207 and (b) the open monitoring well M345-109 at the ASR site. The particle motions of Stoneley waves decay exponentially away from the fluid/well interface (modified from Hardage (1985)).

Stoneley waves have received increased attention due to their correlation with reservoir permeability. The acoustic wave propagation in the permeable layer was investigated by Rosenbaum (1974). Rosenbaum used Biot's theory (Biot 1956a, 1956b) to describe wave propagation in a fluid-filled borehole surrounded by a porous solid. Tang and Cheng (1993) created a 1D theoretical formulation model of tube wave interactions with permeable porous layers. According to their model, Stoneley waves in a permeable layer can be characterised by the effective wave number k_2 given by

$$k_2 = \sqrt{k_e^2 + \frac{2iR\rho_f\omega\, k(\omega)}{(R^2 - a^2)\mu} \sqrt{\frac{-i\omega}{D}} \frac{k_1(R\sqrt{\frac{-i\omega}{D}})}{k_0(R\sqrt{\frac{-i\omega}{D}})}},$$

2-1

and

$$D = \frac{K(\omega)\rho_f v_f^2}{\phi\eta(1+\xi)} \qquad \textbf{2-2}$$

where D is the pore fluid diffusivity, k_1 and k_0 are modified Bessel functions of the second order m ($m = 0,1$), R and a are the borehole and logging tool radii, respectively, $K(\omega)$ is the dynamic permeability, ρ_f is the pore fluid density, μ is the viscosity, ϕ is the porosity, v_f is the acoustic speed for the pore fluid and ζ is a correction for the pore matrix compressibility (Norris, 1989). k_e is the wavenumber in the case of an elastic layer given by

$$k_e = \omega\sqrt{\rho_f\left(\frac{1}{K_f}+\frac{1}{\mu}\right)}, \qquad \textbf{2-3}$$

where K_f is the fluid bulk modulus and μ is the formation shear rigidity (Bakulin et al., 2005).

Winkler et al. (1989) experimentally and theoretically investigated the dispersion curve of Stoneley waves over a wide range of frequencies from 10 to 100 kHz using the dynamic permeability expression. They found that the permeability effect on Stoneley waves is strongly frequency dependent. This dependency is more significant in the low-frequency region up to 20 kHz (Staal and Robinson, 1977). According to Williams et al. (1984), at frequencies lower than 1 kHz, Stoneley the wave phase velocity is well correlated with core permeability measurements. Numerically, it has been found that dispersion curves of Stoneley waves in open and sealed bores can represent permeability effects at a lower frequency of 1 to 2 kHz for formation permeability values above 1,000 mD (Cheng et al., 1987). Cheng et al. (1991) used Prony's method to transform sonic data from a time to frequency domain and estimate the phase velocity and attenuation of Stoneley waves at a frequency range of 1.5 to 3 kHz.

Overall, the analysis of dispersion curves at low frequencies is considered to be potentially important in the investigation of hydraulic properties from borehole seismic methods. In chapter 3, I describe field experiments to analyse the

characteristics of FWS dispersion at low frequencies in extremely high-permeability, slow formations. Both Stoneley and leaky P modes in open and sand-screen wells were observed and correlated with the formation's hydraulic parameters.

2.2 Seismic interferometry

The main objective of seismic interferometry is to create new seismic records by cross-correlating wavefields received at two locations without knowing the model parameters. The name interferometry has been put forward by radio astronomy, in which radio waves are cross-correlated (Wapenaar et al., 2006; Wapenaar et al., 2010). The idea of seismic interferometry was originally pioneered by the early work of Claerbout (1968), who stated that the autocorrelation of wavefields from a source buried in horizontally layered media is a response to an impulsive source on the surface. This technique requires waves travelling in all directions at each receiver location, which is referred to as equipartioning (Vasconcelos and Snieder, 2008). Another condition is to have many sources surrounding a closed surface, that is, surface sources of equal strength are distributed around the virtual source or receiver pair (Wapenaar et al., 2010). Satisfying these conditions is possible in seismic exploration by recovering long records that contain scattering or multiple reflections near the target area to compensate for the lack of extra sources and equipartioning (Vasconcelos and Snieder, 2008).

The application of seismic interferometry is used in geophysics, such as in seismic exploration using active sources (Bakulin and Calvert, 2006), global seismology using passive sources (Campillo and Paul, 2003), ultrasonic (Weaver and Lobkis, 2001) and ocean acoustic (Sabra et al., 2005). Note that direct-wave interferometry is applicable for crosswell tomography to determine the velocity between two wells.

2.2.1 Seismic interferometry by crosscorrelation

Bakulin and Calvert (2006) developed an approach to redatum ground surface sources in a deviated borehole by cross-correlating the wavefield recorded at two receiver locations. The converted receiver is then called a virtual source (VS). The

authors present a technique for imaging through complex overburden using the time-reversal concept. The time reversal may be described as follows: if the receivers are converted into a source, the second-order time derivative wave equation of the wavefield collected by one receiver gives the same solution when time is reversed (Bakulin and Calvert, 2006). In the ultrasonic scale, time-reversal was first pioneered by Fink (1992) who stated that the time-reversal approach can be used to focus waves on a reflective target behaving as an acoustic source, which then re-emits through inhomogeneous media. This concept is applicable for many types of media, including linearly acoustic, elastic, lossless solids, anisotropic and arbitrarily inhomogeneous media (Wapenaar, 2004). However, for nonlinear or dispersive media (frequency-dependent attenuation) the propagation equation may contain odd-order time derivatives and the time reversed invariance will fail (Fink, 1992).

Bakulin and Calvert (2006) indicated that the best geometry for VS experiments is in deviated or horizontal wells so that sufficient parts of subsurface can be imaged. The algorithm in the virtual source approach is given by

$$D_{ab}(t) = \sum_{k=1}^{N} S_{ka}(-t) * S_{kb}(t), \qquad \textbf{2-4}$$

where $D_{ab}(t)$ is the downhole seismic response at receiver R_a that is assigned to the virtual source, R_b is the selected receiver in which the output trace will be defined, $S_{kb}(t)$ is the response recorded by the R_b receiver from the kth source at the surface, $S_{ka}(-t)$ is the time-reversed portion of the response recorded by R_a from the kth source at the surface and N is the source element. The asterisk denotes the temporal convolution, which turns into correlation after reversing time at the receiver R_a (Wapenaar et al., 2010). Figure 2-7 illustrates the variables that presented in equation 2-4.

In practice, the source wavelets are changing from place to place. Therefore, an additional correction is essential to compensate for the source wavelet and adjust the amplitude of VS data (Bakulin and Calvert, 2006). To do so, first the algorithm in equation 2-4 is applied, then the amplitude shaped by designing the source wavelet from down-going wavefield of $S_{ka}(t)$.

Although 'wavelet-deconvolved crosscorrelation' possesses certain advantages for correcting the amplitude, sophisticated deconvolution is still a subject of ongoing research. Next, I will discuss the advantage of interferometry in crosswell tomography.

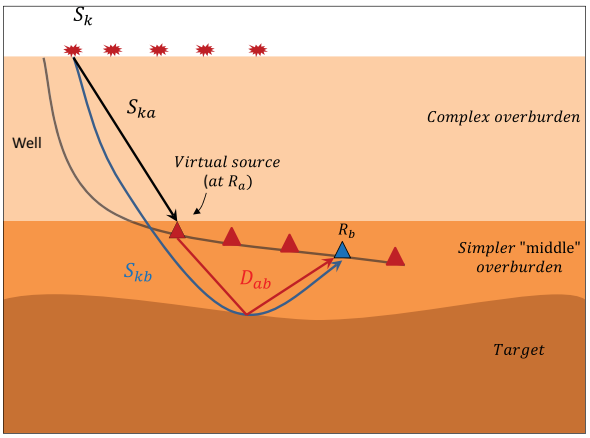

Figure 2-7. The configuration of VS method applied in single borehole (modified from Bakulin and Calvert, 2006). R_a and R_b the receivers in the borehole recoded down-going (black arrow) and up-going (blue arrow) wavefield, respectively. R_a the receiver selected to be a virtual source. D_{ab} the downhole seismic trace for the selected VS-receiver pair. S_{ka} and S_{kb} are the traces recoded Form *k*th source at the surface by receivers R_a and R_b respectively.

2.2.2 Borehole seismic interferometry applications

Borehole seismic interferometry may provide additional information for imaging complex subsurface structures using seismic multiples. Jiang (2006) used the Fermat's interferometry principle and the summation of diffracted energy and interbedded multiples to recover a salt boundary. This technique is also part of a well-known interferometric imaging procedure. Yu and Schuster (2006) used ghost reflections in reversed vertical seismic profiling to recover subsurface images. The interferometry migrated imaging of ghost reflections can be performed without knowing the sources' positions and their wavelets.

Schuster (2005) used reflection traveltime differences from two deep interfaces to invert for a velocity model. Schuster used a synthetic experiment to redatum the surface sources to a reference interface using a single deviated well. This method is called 'interferometric target-oriented tomography'. Another synthetic experiment in interferometric tomography was conducted by Zhou and Schuster (2000). The authors embedded the interferometry concept within standard traveltime tomography inversion and referred to the method as the 'phase-closure principle'. The phase-closure principle can provide additional improvements in conventional tomographic inversion if source static is present.

Torii et al. (2006) used the virtual source approach of Bakulin and Calvert (2006) to retrieve the direct arrival. They conducted a small-scale laboratory experiment involving two boreholes using the homogeneous, closed system of a vinyl chloride board (100 cm long x 170 cm wide).

This series of published work suggested that crosscorrelation interferometry could offer new insights in recovering the velocity between two or more vertical wells. In this study, I examined the principle of crosscorrelation seismic interferometry in crosswell tomography for synthetic and field data.

2.3 Principle of tomography inversion

In the last few decades tomographic reconstruction has been widely used in a variety of scientific fields to reveal images of hidden objects from tomographic data. In 1917 Australian mathematician Johann Radon demonstrated the possibility of reconstructing continuous 2D functions from a set of 1D line integrals. Radon's technique was implemented in medical imaging where X-ray attenuation was used to obtain density images of the human body as described in the early work of Hounsfield (1972) and Iyer (1993).

In geophysical applications the measured traveltime or the amplitude of transmitted waves is used to extract the spatial distribution of physical parameters, such as velocities and attenuation. In practical geophysics, the area under

investigation can only be covered by a limited number of lines (or rays), which can result in an instability problem for inversion methods.

In this section I will discuss two of the most prominent tomographic inversion methods. I briefly review the advantage of using the simultaneous iterative reconstruction technique (SIRT) using straight and curved ray theory. Such techniques will be applied later in the thesis.

2.3.1 Straight-ray simultaneous iterative reconstruction technique

The total traveltime of the seismic wave is a function of propagation velocity $v(x, y)$ and ray geometry. In the $x - y$ plane, the total traveltime is obtained from the line integral as follows (Krajewski et al., 1989)

$$t_k = \int_r \frac{dr}{v(x,y)}, \qquad k = 1, 2, \dots N,$$

2-5

where t_k is the observed traveltime for ray k and r is the raylength. The integral above can be expressed as a sum of linear equations:

$$t_k = \sum_{i=1}^{I} r_{ik}\, S_i\,,$$

2-6

where r_{ik} is length of the ray k that intersects pixel i, I is the total number of pixels intersected by the ray k and S_i is the slowness of pixel i (inverse velocity). To solve an inversion problem, the initial slowness value of S_i^0 is modified through a number of iterations n and a calculated traveltime t_k^n is obtained along each raypath using the following equation:

$$t_k^n = \sum_{i=1}^{I} r_{ik}\, S_i^n,$$

2-7

where S_i^n is the slowness of pixel i after the nth iteration. The difference between observed (t_k) and calculated (t_k^n) traveltimes gives the residual Δt_k^n, which is minimised to achieve the best results:

$$\Delta\, t_k^n = t_k^n - t_k. \qquad \textbf{2-8}$$

The correction to the previous slowness values ΔS_i^n can be given as

$$\Delta S_i^n = \sum_{ik} \frac{r_{ik}\, \Delta t_k^n}{\sum_{ik}(r_{ik}^2)}\ , \qquad \textbf{2-9}$$

where r_{ik} is updated after each iteration using ray tracing.This correction is added to the previous slowness values to improve the initial slowness values, as follows:

$$S_i^{n+1} = S_i^n + \Delta S_i^n \qquad \textbf{2-10}$$

The inversion requires a smoothing operator in the initial slowness values to achieve satisfactory convergence. Usually this smoothing is computed with a weighting operator that replaces the slowness value with $\overline{S_{i,m}^n}$ (Krajewski et al., 1989):

$$\overline{S_{i,m}^n} = \frac{W_1 S_{i,m} + W_2(S_{i+1,m} + S_{i-1,m} + S_{i,m-1} + S_{i,m+1})}{(W_1 + 4W_2)}, \qquad \textbf{2-11}$$

where W_i is the weighting operator for the cell's slowness while I and m are the cells in which the smoothing of the slowness field will be applied (Figure 2-8). These steps are repeated for all specified iterations until a certain cut-off criterion is satisfied (Krajewski et al., 1989).

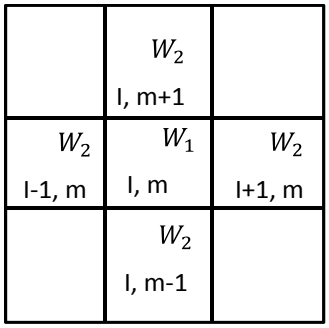

Figure 2-8. Cells associated with the smoothing operator for the slowness field in cell(I, m) **(**Krajewski et al., 1989**).**

2.3.2 Curved-ray simultaneous iterative reconstruction technique

A large velocity contrast can generate refraction effects. As a result the assumption of straight raypaths becomes an inappropriate solution for tomography inversion. Curved-ray algorithms are instead used to take into account a bending-ray situation. Such a technique is essential for seismic refraction tomography (Cha and Vest, 1981). For each cell the raypath is expressed as a circular arc that has a radius dependent on the gradient of the velocity field and distance. The velocity gradient in each cell is obtained by

$$grad_x v = \frac{v(I+1,m) - v(I-1,m)}{2\Delta x}, \quad \textbf{2-12}$$

And

$$grad_y v = \frac{v(I,m+1) - v(I,m-1)}{2\Delta y}, \quad \textbf{2-13}$$

where Δx and Δy are the cell dimensions. The value of the velocity gradient |grad v|, the direction angle $\emptyset_{\text{grad v}}$ and radius of ray curvature c(I, m) passing through a pixel at a direction angle of $\emptyset_0$ are given by Krajewski et al. (1989) as

$$|grad\ v| = \sqrt{(grad_x^2 v + grad_y^2 v)}\ , \tag{2-14}$$

$$\emptyset_{grad\ v} = \frac{\arccos(grad_x v)}{|grad\ v|}\ , \tag{2-15}$$

$$c(I,m) = \frac{1}{v(I,m)^{-1}\ |\ grad\ v|\ \sin(\emptyset_0\ - \emptyset_{grad\ v})}\ . \tag{2-16}$$

2.4 Principle of simultaneous vertical seismic profiling

Simultaneous vertical seismic profiling is a measurement procedure in which seismic wavefields generated on the surface are recorded by receiver strings fitted into two or more boreholes. Figure 2-9 shows the simultaneous VSP configuration using two boreholes. Here both up-going (blue) and down-going (red) waves are recorded in two boreholes simultaneously. This geometry provides not only insights into seismic wave propagation but it also improves the analysis and interpretation of VSP data. For example, in the case of zero-offset VSP one borehole string can provide complete vertical receiver coverage by moving the string up or down every time the source is generated. In the meantime another string can be stationary, monitoring the traveltime and possible amplitude changes associated with near-surface conditions. The important aspect here is that a wide range of seismic data may be collected in a fraction of the time with no extra cost, such as walkaway vertical seismic profiling (WVSP) and seismic interferometry (Almalki et al., 2012). To utilise these advantages I produced an effective simultaneous VSP acquisition method that can be readily implemented in seismic interferometry.

Coming up next is an overview of the simultaneous VSP methodology and highlight of some challenges related to VSP acquisition in slow formations.

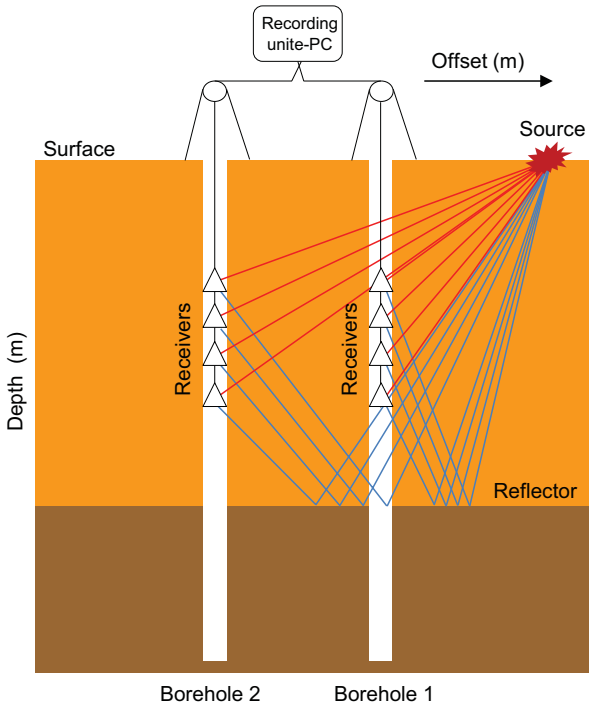

Figure 2-9. The basic field requirements for simultaneous vertical seismic profiling consists of two boreholes, two receiver strings (hydrophones or geophones) connected to a recording system and a seismic source offset from both boreholes.

2.4.1 Previous work with simultaneous VSP

The first attempt to combine two seismic surveys was pioneered by Alam and Manzur (1990), who acquired 3D marine surface seismic data simultaneously with vertical seismic profiling using a single receiver deployed several times to achieve a particular depth coverage. Simultaneous acquisition of 3D surface seismic and 3-component 3D VSP data was carried out by Chopra et al. (2002). Their experiments were performed with the goal of (i) providing an accurate velocity model for 3D seismic data, (ii) correlating the seismic and borehole data and (iii) providing a high-frequency image of the subsurface.

A number of seismic attributes can be extracted from VSP data and used for the processing of surface seismic data. Such attributes include a velocity model, deconvolution, amplitude correction and anisotropy parameters (Constance et al., 2000). Barakat et al. (2009) provided a comprehensive example of acquisition of high resolution simultaneous VSP and land seismic data. Combining VSP and land seismic surveys was used to provide excellent reservoir characterisation and refine the input parameters for seismic data processing.

It is important to note that in previous studies the simultaneous VSP and surface seismic data were obtained using a single borehole. Simultaneous multi-level or dense zero-VSP and walk-away VSP was acquired in an unconsolidated and uncompacted near-surface sedimentary deposit using hydrophone arrays (Almalki et al., 2011). The authors showed how simultaneous VSP data can provide insights into VSP signal analysis and the detailed velocity distribution between two wells. Simultaneous VSP was acquired in the North Sea using new borehole equipment called 'intelligent distributed acoustic sensing' (iDAS) (Madsen et al., 2013). This equipment was designed recently using fibre optic borehole arrays. Simultaneous VSP data were acquired from three production wells to reveal the flow parameters.

2.4.2 VSP limitations and challenges

2.4.2.1 Resolution

The resolution of the subsurface image obtained by surface seismic surveys is relatively low compared to the VSP surveys. This is because the surface seismic data is inherently affected by near-surface conditions, noise and multiples (Milligan et al., 1997). In contrast, VSP data provide greater resolution for subsurface structures because of three main factors including its (i) wider frequency bandwidth, (ii) improved signal to noise ratio and (iii) a small attenuation value associated with shorter travel path.

The vertical resolution of the seismic data to discriminate geologic features is based on the velocity and the frequency of the seismic wavelet, as given by (Widess, 1973)

$$T_{min} = \frac{v}{4f} = \frac{\lambda}{4},$$

2-17

where T_{min} is the bed thickness, v is the velocity, f is the frequency and λ is the wavelength (also λ/4 is Rayleigh's criterion which describe the interface or bed resolution (Kallweit and Wood, 1982)) . However, there are other factors that affect the vertical resolution, which include the pre-analysis degree of the known seismic wavelet and the acquisition tools and geometry (Widess, 1973).

The disadvantage of VSP data is that the subsurface lateral coverage is small compared to the surface seismic survey (Payne et al., 1994). VSP surveying has trade-offs between subsurface coverage and the resolution (Van der Pal et al., 1996). If the receivers are deployed closer to the target, then high resolution images can be achieved but with small coverage (e.g., "Fersnel zone"). Van der Pal et al. (1996) expressed this relationship for a homogenous layer model as

$$\Delta x = \frac{x}{2 + \frac{z}{b}},$$

2-18

where z is the receiver depth, b is the target depth, x is the source offset and Δx is the subsurface coverage.

2.4.2.2 Soil compaction

Within a few metres in unconsolidated soil the quality factor Q and P-wave velocity v_p decrease significantly to as low as 0.3 and 30 m/s, respectively (Rice et al., 1991). This results in a short distance L in which the quality factor Q decreases (inverse attenuation) especially for high-frequency f signals. This length is given by (Rice et al., 1991)

$$L = \frac{Qv}{\pi f},$$

2-19

Soil compaction in a soft sediment environment becomes depth dependent at the source location. The source wavelet is altered after changing the source location

during VSP surveys, which requires further signal analysis. In general, the effect of near-surface soil compaction is not uncommon in seismic data.

2.4.2.3 Tube waves

Another common problem with acquiring VSP data using a hydrophone string concerns the tube wave's arrival. Tube waves are confined in the borehole with little geometrical spreading, which promotes their large amplitude, this can obscure reflection energy in the seismic record (Bois et al., 1972). It is widely known that tube wave velocities are strictly less than the acoustic velocity of the borehole fluid. The tube waves will likely affect data recorded by hydrophones more than data recorded by clamped geophones. Hardage (1985) reported that if the geophones are rigidly coupled to the borehole wall, the particle motions of tube waves will be attenuated because the sensitivity of the geophone will change according to the particle motion associated with the rock properties. Milligan et al. (1997) concluded that additional design is required to attenuate these modes during acquisition. They proposed a method using closed-cell-foam baffles between the hydrophones to attenuate the high energy of tube waves.

An example of tube waves in data collected during this research is illustrated in Figure 2-10. The data is acquired using a string of twenty-four hydrophones spanning the depth from 170 to 400 m at the Mirrabooka ASR site. When the seismic source hits the ground, the up- and down-going tube waves are generated as results of surface waves that pass the well and transfer some energy into the borehole fluid (Hardage, 1981). The point to be noticed here is that at shallow depths, the amplitude of the tube waves is larger in the shallow part of the well compare to the deep section of the well (Bois et al., 1972).

In Figure 2-10, the tube wave velocity is 1200 m/s while the formation P-wave's velocity is as low as 1700 m/s specially at the shallow part of the formation (i.e., from 170 to 200 m). Thus, the separation of wavefield (i.e., reflected P-waves and tube waves) in the shallow part of the formation would be problematic if conventional VSP processing were to be used.

In this chapter I have considered basic principles of the set of borehole seismic techniques relevant to research presented in subsequent chapters 3, 4 and 5.

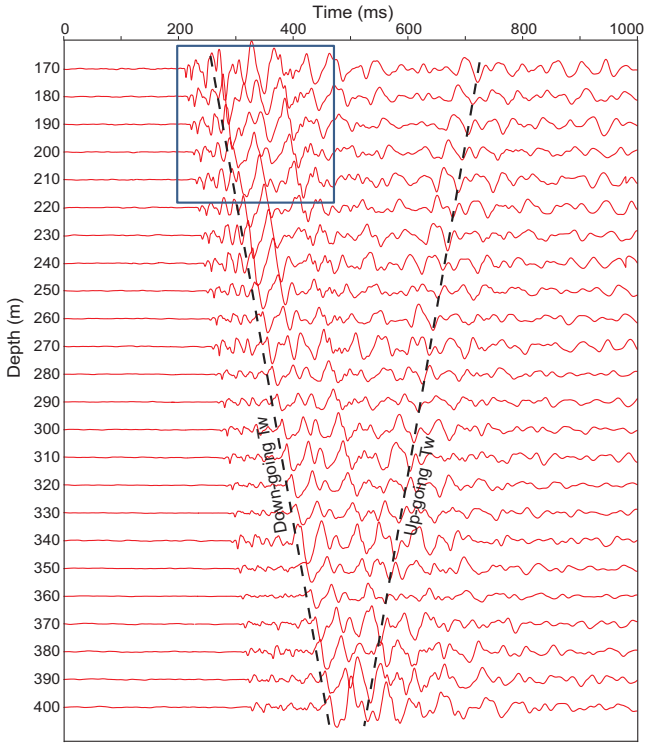

Figure 2-10. **An example of tube waves acquired using a twenty-four hydrophone string spanning the depth from 170 to 400 m in monitoring well borehole M345-109 at the ASR site. The tube waves obscure the reflection events and have a large amplitude at the shallow borehole depth level, as highlighted in the box.**

2.5 References

Alam, M. A., and A. Manzur, 1990, Simultaneous vertical-seismic profiling and surface seismic acquisition method: Google Patents.

Almalki, M., B. Harris, and J. C. Dupuis, 2011, Simultaneous Vertical Seismic Profiling in Two Wells and the Virtual Source Method; Perth Basin Western Australia: 73rd EAGE conference and exhibition, F045.

Almalki, M., B. Harris, and J. C. Dupuis, 2012, Numerical and field experiments for virtual source tomography, Perth Basin, Western Australia: 22nd International Geophysical Conference and Exhibition, ASEG Extended Abstracts, 1–4.

Bakulin, A., and R. Calvert, 2006, The virtual source method: Theory and case study: Geophysics, **71**, SI139–SI150.

Bakulin, A., B. Gurevich, R. Ciz, and S. Ziatdinov, 2005, Tube-wave reflection from a porous permeable layer with an idealized perforation:75th Annual International Meeting, SEG Expanded Abstracts, 332–335.

Bakulin, A., F. Karpfinger, and B. Gurevich, 2008, Understanding the acoustic response of deepwater completions: The Leading Edge, **27**, 1646–1653.

Barakat, S., M. Denis, S. Seeni, P. Amortila, and S. Robinson, 2009, High resolution, simultaneous VSP and land seismic acquisition: International Petroleum Technology Conference, IPTC Extended Abstract,13617.

Biot, M. A., 1956a, Theory of propagation of elastic waves in a fluid-saturated porous solid. I. Low-frequency range: The Journal of the Acoustical Society of America, **28**, 168.

Biot, M. A., 1956b, Theory of propagation of elastic waves in a fluid-saturated porous solid. II. Higher frequency range: The Journal of the Acoustical Society of America, **28**, 179.

Bois, P., M. La Porte, M. Lavergne, and G. Thomas, 1972, Well-to-well seismic measurements: Geophysics, **37**, 471-480.

Campillo, M., and A. Paul, 2003, Long-range correlations in the diffuse seismic coda: Science, 299, 547–549.

Cha, S., and C. M. Vest, 1981, Tomographic reconstruction of strongly refracting fields and its application to interferometric measurement of boundary layers: Applied Optics, **20**, 2787–2794.

Cheng, C., Z. Jinzhong, and D. R. Burns, 1987, Effects of in situ permeability on the propagation of Stoneley (tube) waves in a borehole: Geophysics, **52**, 1279–1289.

Cheng, C. H., and M. N. Toksöz, 1981, Elastic wave propagation in a fluid-filled borehole and synthetic acoustic logs: Geophysics, **46**, 1042–1053.

Cheng, N., C. Cheng, and M. Toksoz, 1991, Borehole Stoneley wave inversion for formation parameters: 61st Annual International Meeting, SEG Expanded Abstracts, 1633–1636.

Chopra, S., E. Blias, A. Manerikar, A. Kryzan, L. Chavina, V. Alexeev, and G. Larsen, 1999, Simultaneous acquisition of 3D surface seismic and 3D VSP data—processing and integration: 69th Annual International Meeting, SEG Expanded Abstracts, 2337–2340.

Claerbout, J. F., 1968, Synthesis of a layered medium from its acoustic transmission response: Geophysics, **33**, 264–269.

Constance, P., M. Holland, S. Roche, P. Bicquart, B. Bryans, S. Gelinsky, J. Ralph, and R. Bloor, 2000, Simultaneous acquisition of 3D surface seismic data and 3C, 3D VSP data: Houston geological society bulletin, **42**, 15–24.

Fink, M., 1992, Time reversal of ultrasonic fields. I. Basic principles: Ultrasonics, Ferroelectrics and Frequency Control, IEEE Transactions on 39, 555–566.

Gilbert, P., 1972, Iterative methods for the three-dimensional reconstruction of an object from projections: Journal of Theoretical Biology, **36**, 105–117.

Hardage, B. A., 1985, Handbook of geophysical exploration; Vertical seismic profiling; Principles: Pergamon Press, ISBN 094663128X.

Hardage, B. A., 1981, An examination of tube wave noise in vertical seismic profiling data: Geophysics, **46**, 892-903.

Hounsfield, G. N., 1972, Method and apparatus for measuring x-or y-radiation absorption or transmission at plural angles and analyzing the data: US Patent 3, 778614.

Iyer, H., 1993, Seismic tomography: Theory and practice: Springer, ISBN 0412371901.

Jiang, Z., 2006, Migration of interbed multiple reflections: 76th Annual International Meeting, SEG Expanded Abstracts, 3501–3505.

Kallweit, R.S., and L.C. Wood, 1982, The limits of resolution of zero-phase wavelets, Geophysics, **47**, 1035.

Krajewski, C., L. Dresen, C. Gelbke, and H. Rüter, 1989, Iterative tomographic methods to locate seismic low-velocity anomalies: a model study: Geophysical prospecting, **37**, 717–751.

Madsen, K., S. Dümmong, A. Kritski, Ĺ. Pedersen, D. Finfer, A. Gillies, and P. Travis, 2013, Simultaneous multiwell VSP in the North Sea using distributed acoustic sensing: 75th EAGE conference and exhibition, F431.

Milligan, P. A., J. W. Rector, and R. W. Bainer, 1997, Hydrophone VSP imaging at a shallow site: Geophysics, **62**, 842–852.

Norris, A. N., 1989, Stoneley-wave attenuation and dispersion in permeable formations: Geophysics, **54**, 330–341.

Oliver, J., and M. Major, 1960, Leaking modes and the PL phase: Bulletin of the Seismological Society of America, **50**, 165–180.

Paillet, F. L., and C. Cheng, 1986, A numerical investigation of head waves and leaky modes in fluid-filled boreholes: Geophysics, **51**, 1438–1449.

Payne, M. A., E. A. Eriksen, and T. D. Rape, 1994, Considerations for high-resolution VSP imaging: The Leading Edge, **13**, 173-180.

Rice, J., C. E. Krohn, and L. Houston, 1991, Shallow near-surface effects on seismic waves: 61st Annual International Meeting, SEG Expanded Abstracts, 747–749.

Rosenbaum, J., 1974, Synthetic microseismograms: logging in porous formations: Geophysics, **39**, 14–32.

Sabra, K. G., P. Roux, and W. Kuperman, 2005, Arrival-time structure of the time-averaged ambient noise cross-correlation function in an oceanic waveguide: The Journal of the Acoustical Society of America, **117**, 164–174.

Schuster, G. T., 2005, Fermat's interferometric principle for target-oriented travel time tomography: Geophysics, **70**, U47–U50.

Staal, J. J., and J. D. Robinson, 1977, Permeability profiles from acoustic logging: 52nd Annual Fall Technical Conference, SPE, 6821.

Tang, X. M., and C. Cheng, 1993, Borehole stoneley wave propagation across permeable structures: Geophysical prospecting, **41**, 165–187.

Torii, K., K. Shiraishi, K. Onishi, T. Kimura, S. Ito, T. Aizawa, K. Tsukada, and T. Matsuoka, 2006, Cross-hole tomography using seismic interferometry: 68th EAGE conference and exhibition, A044.

Van der Pal, R., M. Bacon, and D. Pronk, 1996, 3D walkaway VSP, enhancing seismic resolution for development optimization of the Brent field: First Break, **14**, 463–469.

Vasconcelos, I., and R. Snieder, 2008, Interferometry by deconvolution: Part 1—Theory for acoustic waves and numerical examples: Geophysics, 73, S115–S128.

Wapenaar, K., 2004, Retrieving the elastodynamic Green's function of an arbitrary inhomogeneous medium by cross correlation: Physical Review Letters, **93**, 254301.

Wapenaar, K., D. Draganov, and J. Robertsson, 2006, Introduction to the supplement on seismic interferometry: Geophysics, **71**, SI1–SI4.

Wapenaar, K., D. Draganov, R. Snieder, X. Campman, and A. Verdel, 2010, Tutorial on seismic interferometry: Part 1—Basic principles and applications: Geophysics, **75**, 195–209.

Weaver, R. L., and O.I. Lobkis, 2001, Ultrasonics without a source; Thermal fluctuation correlations at MHz frequencies: Physical Review Letters, **87**, 134301.

Widess, M., 1973. How thin is a thin bed?: Geophysics, **38**, 1176–1180.

Williams, D., J. Zemanek, F. Angona, C. Dennis, and R. Caldwell, 1984, The long space acoustic logging tool: 25th Annual Logging Symposium Transactions, Society of Professional Well Log Analysts, T1–T16.

Winkler, K. W., H. L. Liu, and D. L. Johnson, 1989, Permeability and borehole Stoneley waves: Comparison between experiment and theory: Geophysics, **54**, 66–75.

Yu, J., and G. T. Schuster, 2006, Crosscorrelogram migration of inverse vertical seismic profile data: Geophysics, **71**, S1–S11.

Zhou, M., and G. T. Schuster, 2000, Interferometric traveltime tomography: 70th Annual International Meeting, SEG, Expanded Abstract, 2138–2141.

CHAPTER 3 : Multifrequency Full Waveform Sonic Logging in the Screened Interval of a Large-diameter Production Well[1]

In this chapter, I developed methods for imaging and analysing phase velocity-frequency dispersion images from the entire wavetrain of field data. This represents the first published case of full waveform dispersion images acquired in a sand-screened production well and open hole. This research is published in the journal *Geophysics*.

1. Almalki, M., B. Harris, and C.J. Dupuis, 2013, Multifrequency full-waveform sonic logging in the screened interval of a large-diameter production well: Geophysics, **78** (5), B243-B257.

3.1 Summary

A set of field experiments using multiple transmitter centre frequencies was completed to test the application potential of low-frequency full waveform sonic logging in large-diameter production wells. Wireline logs were acquired in a simple open drillhole and a high-yield large diameter production well completed with wire-wound sand screens at an aquifer storage and recovery site in Perth, Western Australia. Phase-shift transform methods were applied to obtain phase-velocity dispersion images for frequencies of up to 4 kHz. A 3D representation of phase-velocity dispersion was developed to assist in the analysis of possible connections between low-frequency wave propagation modes and the distribution of hydraulic properties. For sandstone intervals in the test well, the highest hydraulic conductivity intervals were typically correlated with the lowest phase velocities. The main characteristics of dispersion images obtained from the sand-screened well were highly comparable with those obtained at the same depth level in a nearby simple drillhole open to the formation. The sand-screened well and the open-hole displayed an expected and substantial difference between dispersion in sand- and clay-dominated intervals. It appears that for clay-dominated formations, the rate of change of phase velocity can be associated with clay content. We demonstrated that with appropriate acquisition and processing, multifrequency full waveform sonic logging applied in existing large diameter sand-screened wells can produce valuable results. There are few wireline logging technologies that can be applied in this setting. The techniques that we used would be highly suitable for time-lapse applications in high-volume production wells or for reassessing formation properties behind existing historical production wells.

3.2 Introduction

Most large sedimentary basins contain thousands of wells of all types. Production wells must have their production interval open to the formation. A technology that could recover hydraulic or mechanical properties from behind the production interval would be of considerable value, in particular for time-lapse investigations into well efficiency. We believe full waveform sonic (FWS) logging at low frequencies offers the potential for obtaining near-well properties even in large-diameter screened

production wells. That is, the most valuable information may be hidden in the wavetrain, which is recorded at each receiver; however, extracting this information remains a challenge.

High-yield water supply wells can have a long and sometime complex life commencing with drilling and installation of the casing. For shallow high-permeability formations, weakly consolidated or even flowing sands, collapsing formations and extremes in hydraulic conductivity are a present threat during drilling and before the casing is set in place. In the longer term many forms of well clogging may occur. Dramatic changes in near-well hydraulic conductivity can occur throughout the life of a well.

3.2.1 Waveform sonic modes in slow-formation

Elastic waves propagating within a fluid-filled cylinder, such as a well, have different dispersive and nondispersive modes. In this research paper, the word "dispersion" is taken to mean any change in phase velocity with frequency. Apart from the compressional and shear-head waves, the dispersive modes generated by monopole FWS excitation in a well include pseudo-Rayleigh or normal mode (Paillet, 1980), leaky mode (White, 1962; Paillet and Cheng, 1986), or compressional modes (Wu et al., 1995) and Stoneley mode (Biot, 1952). In slow formations, the main components in FWS data are the compressional head waves and dispersive leaky and Stoneley modes (Ellefsen et al., 1989; Rao and Vandiver, 1999; Mavko et al., 2009).

The leaky mode in slow formations is a result of multiple reflected and constructively interfering head waves, which attenuate energy into the formation with distance (Tichelaar and Luik, 1995). This mode follows the fast compressional head wave in a FWS record and travels at velocities ranging between the formation P-wave velocity and fluid-wave velocity in the borehole. The leaky mode energy is slightly dispersive; that is, the low frequencies travel faster than the high frequencies (Franco et al., 2006) and are partially trapped in the borehole fluid (Burns, 1986). The leaky mode in FWS records is usually strong in slow formations and large diameter wells (Crain, 2004).

On the other hand, Stoneley waves have a relatively slow velocity, large amplitude (Tang and Cheng, 1993; Tezuka et al., 1997) and include waves traveling along the formation-well interface (Mavko et al., 2009). Thus, the Stoneley-wave phase velocities are often less than the velocity of sound in fluid (Cheng and Toksoz, 1982). In permeable formations the borehole fluid can also escape into pores. This reduces the velocity of the Stoneley wave causing dispersion and attenuation. Stoneley waves contain information concerning permeability, elastic moduli and density (Rosenbaum, 1974; Staal and Robinson, 1977; Williams et al., 1984; Cheng et al., 1987; Tang and Cheng, 1993).

3.2.2 Previous work in production wells

There are few case studies examining the propagation of poroelastic waves in sand-screened wells. Recently, Bakulin et al. (2005) investigated the properties of tube waves using an "idealised perforation" model of poroelastic and elastic layers. The authors observed that the Stoneley wave remains sensitive to the fluid flow passing through the open portion of perforations. Karpfinger (2009) demonstrated the influence of the formation permeability on dispersion curves. That is, the dispersion curves were shifted to lower velocities as the permeability increased.

Bakulin et al. (2008a, 2008b, 2009) proposed real-time completion monitoring techniques. These techniques use changes in the characteristics of tube waves to examine permeability variations in sand-screened deepwater completions. In sand-screened completions, there are two types of tube waves (slow and fast) that relate to an inner fluid column and the gravel in the annulus (Bakulin et al., 2009). These previous efforts propose excellent numerical and physical experiments for wells completed using casing and perforation combinations. Our case study presents the field challenge, which differs from other previous works (Bakulin et al., 2008a, 2008b, 2009; Karpfinger, 2009) in two main ways. First, the production well was completed with specially designed stainless steel sand-screen casing with the annulus filled by formation material (i.e., the well was naturally developed) and second, the permeability of the sand intervals is extremely high. To fully numerically describe wave propagation spanning several modes for the specific aquifer storage and recovery (ASR) well used in this case study, we would likely require either a new

formulation or significant adaptation of existing algorithms. What we present here is a case study for a new application of low-frequency FWS logging.

The sensitivity of the Stoneley wave or the low-frequency leaky mode to the hydraulic conductivity of the formation at the production interval is of particular importance. The development of new representations of the phase-velocity dispersion may be of considerable benefit to the hydrocarbon (conventional and unconventional), water, geothermal and mining industries. Our field experiment has a rare combination of key inputs that include the following:

1) Hydraulic conductivity distribution is defined by repeat flow logging in a formation consisting of a wide range of hydraulic conductivity, from negligible to greater than 40 m/day.
2) FWS logging is completed at a wide range of transmitter centre frequencies with the maximum energy in the key frequency range from 1 to 4 kHz.
3) The experiments include FWS logging in an open hole and a large diameter sand-screened production well.

The ultimate goal of such investigations is to develop FWS logging techniques to aid in understanding the distribution of hydraulic and elastic properties of the near-well environment. In addition, the application of repeat FWS logging for time-lapse monitoring of changes in near-well permeability may become possible if a robust link between the FWS derived parameters and permeability can be established.

In the following sections, we first review methods for processing FWS dispersion. We then describe the field experiment followed by development of methods for analysing and interpreting FWS dispersion. We also compare the dispersion analysis between open hole and large-diameter sand-screened wells, highlighting their similarities and their differences. We conclude by investigating possible links between the dispersion and formation hydraulic conductivity.

3.2.3 Theoretical background

The analysis of dispersion from FWS wireline logging opens new possibilities for interpreting formation properties. That is, a variety of phase-velocity–frequency-transform methods were developed to improve computation of dispersion phenomena for FWS logging in boreholes. For a borehole surrounded by a porous solid, the

complex phase velocity of Stoneley wave v_T at a low frequency is derived by White (1983) and modified by Chang et al. (1988) as

$$\frac{1}{v_T^2} = \rho_{bf}\left(\frac{1}{K_{bf}} + \frac{1}{N} - \frac{2}{i\omega r_b Z}\right), \tag{3-1}$$

where ρ_{bf} and K_{bf} are the density and bulk modulus of the borehole fluid, N is the shear modulus, r_b is the borehole radius, ω is the angular frequency and Z is the borehole wall impedance caused by fluid flow into the permeable formation that is given by

$$\frac{1}{Z} = \frac{\kappa}{\eta r_b}\frac{(1-i)\sqrt{\frac{\omega m}{2}}\, r_b K_1[(1-i)\sqrt{\frac{\omega m}{2}}\, r_b]}{K_0\,[(1-i)\sqrt{\frac{\omega m}{2}}\, r_b]}, \tag{3-2}$$

where

$$m = \frac{\varphi\,\eta}{\kappa\,K_f}\,. \tag{3-3}$$

K_0 and K_1 are modified Bessel functions of orders 0 and 1, η is the pore fluid viscosity, κ is the permeability, K_f is the bulk modulus of the pore fluid and φ is the porosity. In the presence of stainless steel casing material the velocity of the low-frequency tube wave (or Stoneley wave) can be affected by other factors such as the tool and casing material. Norris (1990) formulates the velocity of the low-frequency tube wave and includes other factors such as

$$v_T = (K^*/\rho_{bf})^{1/2}, \tag{3-4}$$

where K^* is the effective bulk modulus given as

$$\frac{1}{K^*} = \frac{1}{K_{bf}} + \frac{1}{1-f}\left(\frac{1}{M_F} + \frac{f}{M_T}\right), \tag{3-5}$$

where f is the volume fraction the tools occupy in the borehole and M_F and M_T are moduli that depend upon the formation and tool, respectively defined as

$$M_T = \mu_T\{(1-f_T)/[f_T + \tfrac{1-\nu_T}{1+\nu_T}]\}, \tag{3-6}$$

$$M_F = \mu_F\left(\frac{1-\nu_C + \left(f_C/2\right)\left(\mu_C/\mu_F - 1\right)(1-\beta\nu_C^2)}{1-\nu_C + \left(f_C/2\right)\left(\mu_f/\mu_c - 1\right)(1-2\nu_C+\beta\nu_C^2)}\right), \tag{3-7}$$

where μ_T and μ_C are the shear modulus of the tool and casing, respectively; ν_T and ν_C are the Poisson's ratio for the tool and casing; $f_T$and f_C are the volume fractions of the inner part of the tool (for a solid tool $f_T = 0$) and the casing, respectively; and β is a parameter that is associated to the contact between the casing and formation (β = 0 for a rigid contact and β =1 for a more lubricated contact). According to equation 3-4 the Stoneley wave speed will increase for the stiff casing material (i.e., stainless steel material) and slightly decrease if the area between the casing and formation is "lubricated" (Norris, 1990). Although the above equations give a general relationship between Stoneley-wave velocity and permeability for simple open and cased wells, it should be noted that it is not easily adapted to recover the Stoneley wave velocity in

a complex sand-screened production well environment. Such numerical analysis is yet to be developed.

Park et al. (1998) reported that the phase-shift method can overcome the disadvantages of the other methods and provides higher resolution dispersion images with improved mode separation for a relatively small number of receivers as follows:

$$U(x,\omega) = e^{-i\Phi x}\, A(x,\omega), \qquad \textbf{3-8}$$

where $\Phi = \omega / c_{\omega}$, ω = frequency in radian and c_{ω} is phase velocity for frequency ω. From the equation 3-8 the integral transformation V (ω, ø) can be obtained as

$$V(\omega,\emptyset) = \int e^{i\emptyset x}\, [U\,(x,\omega)/|U(x,\omega)|\,]dx,$$

$$= \int e^{-i(\Phi-\emptyset)x}\, [A(x,\omega)/|A(x,\omega)|]dx. \qquad \textbf{3-9}$$

In equation 3-9 the integral represents the summing of the offset of wavefields at a frequency after applying an offset-dependent phase shift to the wavefield determined for an assumed phase velocity ($c_{\omega} = \omega / ø$).

Park's method is widely used for many applications; however, we found no other examples in which this method was used to analyse borehole FWS logs. For our experiment, we used the processing methods developed by Park et al. (1998) to characterise the entire wave packet propagation across the FWS array. From this point forward, we use the term "dispersion image" to describe an image of the maximum "normalised" amplitude obtained by the Park's method. The dispersion image can be used to extract phase velocity as a function of frequency.

3.3 Field test site and its characteristics

3.3.1 Mirrabooka aquifer storage and recovery site

The FWS logging field experiments were conducted at the Mirrabooka aquifer storage and recovery (ASR) trial in Perth, Western Australia (Figure 3-1). The ASR trial at Mirrabooka is the second major aquifer replenishment project undertaken by the Water Corporation in the Perth Metropolitan in recent years. The trial includes continuous monitoring of water temperature, electrical conductivity and concentrations of chemicals from five depth levels in the aquifer. The ASR trial site includes five monitoring wells (M345-208, M345-108, M345-109, M345-308 and M345-408) and one large diameter high-volume ASR production well (M345-207). Multifrequency FWS logging was completed over the sand-screened interval of the large-diameter M345-207 production well and in the freshly drilled M345-109 open hole prior to installation of the casing. The distance between M345-207 and M345-109 is small (i.e., 40 m) and wireline logging in the six wells at the site revealed near-horizontal sedimentary layers. Thus, we expected that main formation properties between the two wells would be comparable. The ASR production well had been in service for at least 12 months prior to our FWS logging experiments. Furthermore, FWS logging experiments were completed in monitoring well M345-109 immediately after drilling and before the installation of any casing (i.e., in an open hole).

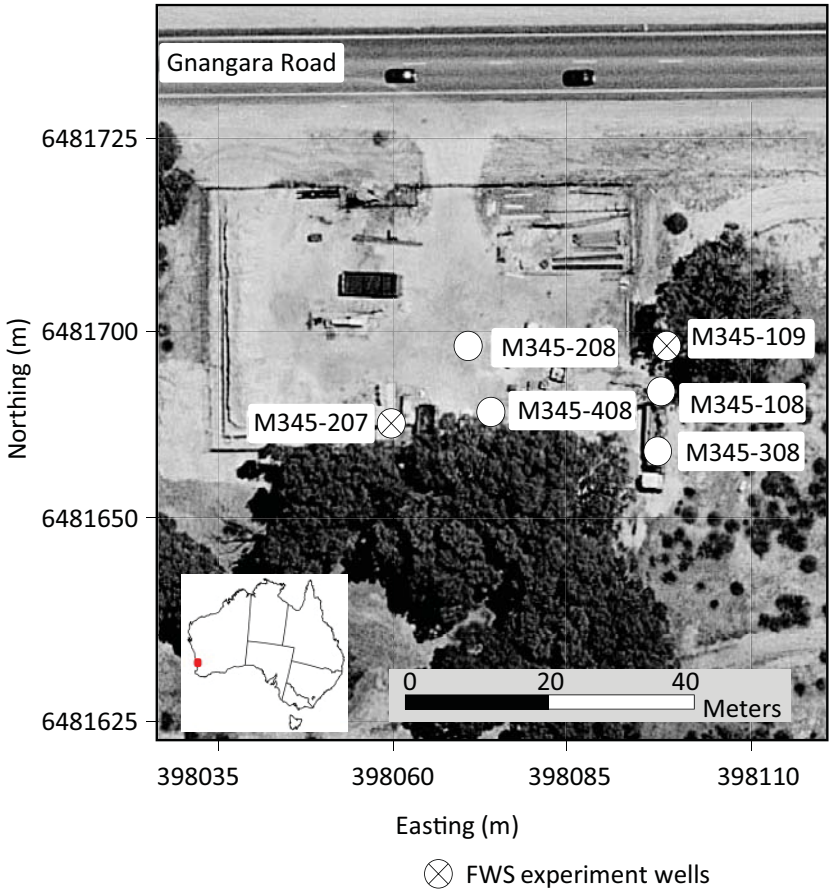

Figure 3-1. **Satellite image shows the Mirrabooka aquifer storage and recovery site located at north Perth, Western Australia. The interwell distance between the experiment wells (M345-207 production well and in the M345-109 monitoring well) is 40 m.**

The total diameter of the drillholes at the M345-207 production well and the M345-109 monitoring well are 381 and 216 mm, respectively. Two intervals in the production well were completed using wire-wound stainless steel sand screens with an inner and outer diameter of 256 and 278 mm, respectively. The production well has a larger diameter than the monitoring well, which may impact the particle motion of the borehole guided wave as previously described in equation 3-4. The sand-screened depth intervals are from 320.1 to 368.1 m and from 394.1 to 427.1 m. The two intervals are separated by plain steel casing. The wire-wound sand screens have 11% of their area open to the formation and an aperture size of 0.5 mm. The production well was developed naturally (without gravel pack) by jetting, followed

by airlifting (Rockwater, 2009). Figure 3-2a highlights the specific dimensions of the wire-wound stainless steel sand screens (i.e., the V-shaped slots, the support rod, the effective shape of the wire and the aperture size).

During the life of a production well, the sand screens and near-well setting may experience many changes in mechanical and hydraulic properties. These may be associated with physical, chemical, or biological changes in the near-well environment. Figure 3-2b and 3-2b provide examples of modern large diameter sand screens and recovered older slotted steel casing commonly used in production wells in the Perth area. Sand screens such as these can be found across the globe. FWS sonic logging at low frequencies may assist in decision making on methods for well development at the start of a well's life and on the appropriate time to decommission a well at the end of its life.

3.3.2 Hydraulic conductivity in the M345-207 production well

A key requirement for the FWS experiment at M345 is an exceedingly good knowledge of the hydraulic conductivity distribution over the injection interval of the ASR well. In this site gamma counts clearly separate the sand/sandstone-dominated layers from the siltstone/claystone-dominated layers. Six sandstone layers are identified in the M345-207 and M345-109 wells, as shown in Figure 3-3. Although the vertical heterogeneity of the sedimentary layers is extreme, the horizontal continuity of the layering between the production and monitoring wells is clear from Figure 3-3. In general, there is a good horizontal continuity of rock properties in the Leederville formation at the ASR site (Xu and Martin, 2008).

Five repeat flow logs were completed in the M345-207 production well after it was cleaned and fully developed (Water Corporation, 2010). To obtain the flow log, the logging tool is placed at the base of the production well, then a submersible pump is switched on and logging up the well is completed. Flow logging obtains a measure of cumulative flow up the well. An estimate of the hydraulic conductivity distribution can be obtained by taking the gradient of the cumulative flow curve and weighting the gradient by the aquifer transmissivity. Transmissivity was determined from a constant rate test. Note that the transmissivity in the production well is high (i.e., of the order 1000 m^2/day) and the well losses (hydraulic head losses at the well-

formation interface) are exceedingly small. This indicates that the well is highly efficient.

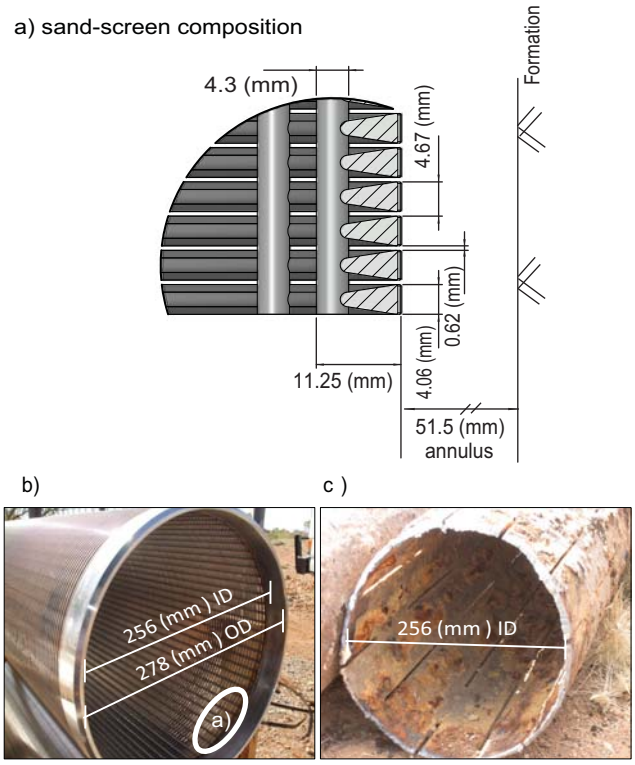

Figure 3-2. **Stainless steel sand-screen casing at the ASR site. (a) Sand-screen composition shows the dimension of V-shaped slots, supported rod, open area of the screen (11%), thickness and annulus. (b) The wire-wound stainless steel sand screens used at production well M345-207. (c) Slotted-type stainless steel sand screens used at different sites experiencing complex changes over many years.**

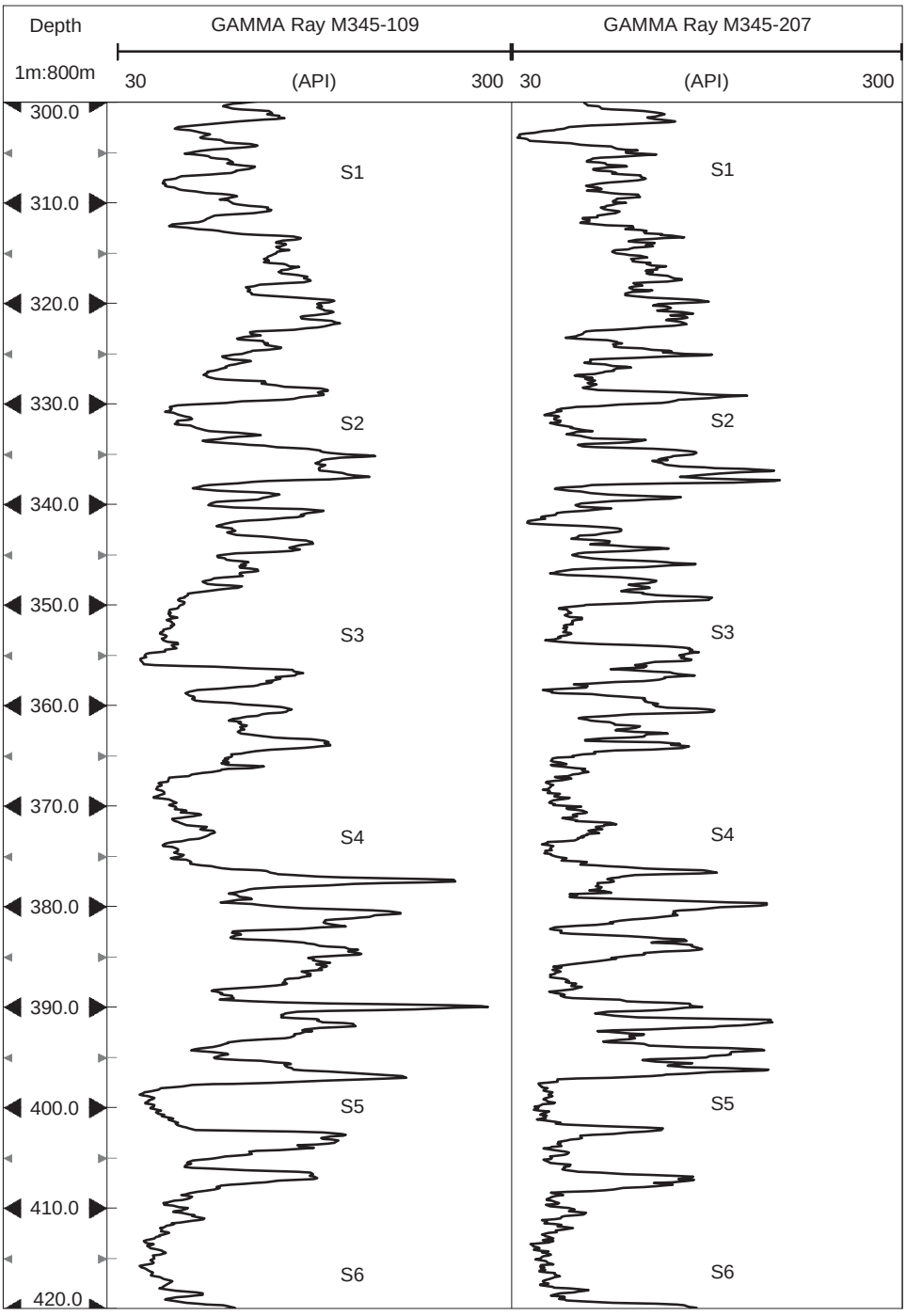

Figure 3-3. **Gamma counts wireline logging for the ASR site. There is a good correlation between the gamma logs in the monitoring well M345-109 (left) and the production well M345-207 (right), which indicates horizontal continuity of at least six sandstone layers (S1,S2,S3,S4,S5,S6) between the wells. The interwell distance is 40 m and the depth intervals between 320 and 420 m below ground level.**

The distribution of hydraulic conductivities estimated from the flow logging was calibrated by the following:

1) Laboratory permeability measurements were taken from selected plugs (Table 3-1) (Weatherford Laboratories, 2010). Several core permeability measurements were made enabling approximate calibration of measured hydraulic conductivity. The results are presented in Figure 3-4. The values of core measurements are also consistent with the average hydraulic conductivity estimated for screen sections (Rockwater, 2011).

2) Hydraulic and solute transport modelling were calibrated with more than 60 layers in the production interval. The calibration (i.e., history matching) was based on measurements taken from multiple depth levels in five close monitoring wells over approximately three years of the ASR trial (Descourvières et al., 2010). That is, the flow distribution in the numerical model closely matched the flow distribution expected from analysis of the flow logs (i.e., the injected water moved past the monitoring wells as predicted by the numerical hydraulic and solute transport model).

3) Distribution of high hydraulic conductivity preferential flow units were identified by time-lapse induction logging over the injection interval during the ASR trial (Malajczuk, 2010). That is, a low-solute concentration was injected into the formations via the screens of the ASR well. This low-solute concentration water was readily identified in fast flow pathways (i.e., high-permeability sands) as a distinct drop in electrical conductivity measured in the time-lapse induction logs (Malajczuk, 2010).

Based on the above results, considerable confidence was placed in the hydraulic conductivity recovered from the flow logs and, in particular, the location of high-permeability sand-dominated units. The obtained values are provided in Figure 3-4. As can be seen, the hydraulic conductivity ranges from negligible (siltstones and shales) to greater than 40 m/day for the coarse weakly consolidated sands. Note that the transition between low and high hydraulic conductivity is generally sharp, which confirms a high degree of vertical heterogeneity in the aquifer.

Table 3-1. Example of formation properties (Weatherford Laboratories, 2010).

Sample number	Depth (m)	Porosity (%)	Permeability (mD)	Grain density (g/cm^3)
SST 16	302.57	38.2	10672	2.63
SST 20	342.75	40.2	7496	2.65
SST 21	352.13	38.8	5648	2.62
SST 05	361.98	35.5	7230	2.64
SST 23	366.35	34.5	3952	2.65
SST 06	377.65	39.2	1752	2.63
SST 25	386.09	36.0	1080	2.61
SST 07	393.54	31.8	8420	2.65
SST 08	406.71	38.6	1198	2.67
SST 28	411.04	35.1	11210	2.62
SST 28	411.26	36.4	13940	2.62
SST 09	448.75	33.4	14766	2.65

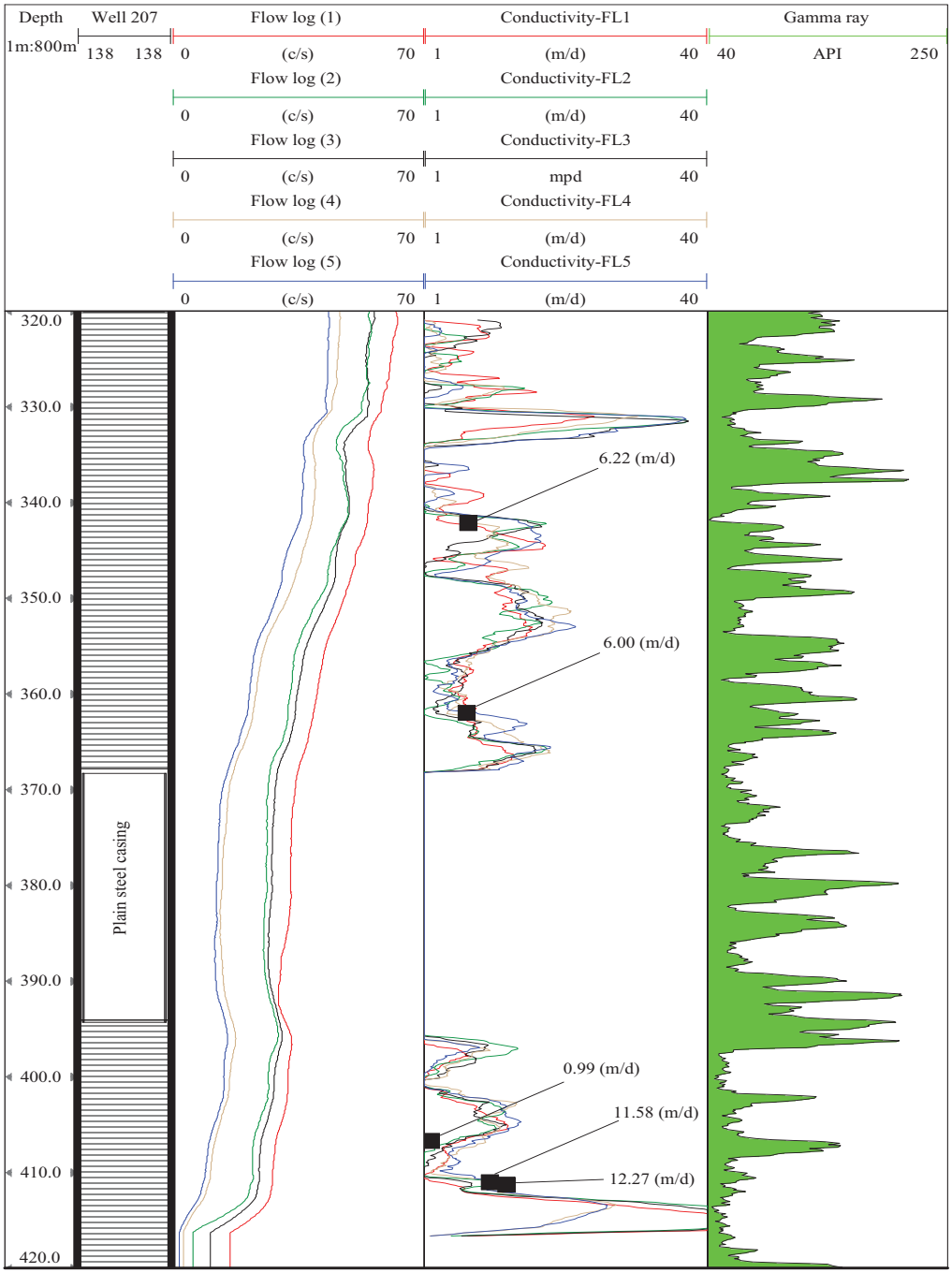

Figure 3-4. Hydraulic conductivity estimated from flow logs. From the left, the well construction, the five flow logs, the hydraulic conductivity and gamma ray for the production well. The interval between 368.1 and 394.1 m is the plain steel casing. Core permeability measurements (illustrated by black squares) show a good agreement with hydraulic conductivity.

3.4 Methods

3.4.1 Full waveform data acquisition

The FWS tool used in this research consisted of one transmitter (i.e., Tx) and four 1C receivers (i.e., Rx1, Rx2, Rx3 and Rx4) separated by 0.3048 m. The near offset from the source to the first receiver was set to 0.9 m.

Similar tool configuration and recording parameters were used for logging the production and monitoring wells (Table 3-2). The major difference in logging parameters between the two surveys was the recording length. The recording length was set longer for experiments in the large-diameter production well to compensate for larger propagation distances. A vertical-source spacing of 10 cm (i.e., sampling down the hole) was specified after considering the heterogeneity of the formation at the ASR site.

To ensure sufficient accuracy over a wide range of frequencies, the FWS data were recorded using a single transmitter that ran with several central frequencies in the production well and the open hole. For all of the acquired FWS data, the frequency bandwidth was approximately 0.9 to 25 kHz with the transmitter central frequencies set for each logging run to 1, 3 and 15 kHz. As expected, changing the transmitter centre frequency had the effect of focusing spectral energy closer to the centre frequency. For example, if the central frequency of the transmitted pulse was set to 5 kHz, then the frequency spectrum would contain all the frequencies between 0.9 and 25 kHz with maximum energy occurring around 5 kHz. Figure 3-5 shows the typical distribution of spectral energy recorded by the four receivers when the transmitter centre frequency was set to 1 kHz. The amplitude spectrum for the FWS data acquired with the transmitter central frequency set to 1 kHz has a strong peak near 1.7 kHz, which is where the Stoneley wave is expected to be the dominant propagation mode. Nevertheless, the spectrum has other peaks at approximately 3 and 5 kHz, which may contain valuable information in this low-frequency band. Although data collected with the 15 kHz transmitter centre frequency retain some energy in the lower frequency band from 1 to 4 kHz, the signal-to-noise ratio (S/N) for this low frequency tends to be relatively low. For this reason we focus on data collected at 1 and 3 kHz transmitter centre frequencies.

Figure 3-6 and 3-7 presents an example of the FWS data acquired in the open-hole and production wells, respectively. These example data sets were acquired at approximately the same depth level in both wells (i.e., 340.5 m). In Figure 3-7, three individual FWS records from the production well collected at different transmitter central frequencies (i.e., 1, 3 and 15 kHz) are presented. The wavetrains recorded consist of (1) compressional head waves followed by (2) a "ringing" tail that is probably related to the monopole leaky mode, which appears from approximately 0.8 to 2 ms on all receivers (i.e., highlighted by boxes in Figure 3-7) and (3) the low-frequency Stoneley wave. The two latter dispersive modes are of principle interest in this study.

Table 3-2. Full waveform acquisition parameters.

Logging parameter	Production well M345-207	Monitoring well M345-109
Date logged	May, 2010	January, 2009
Logging speed	2 m/min	2 m/min
Conditions of well	381-mm-diameter drilled hole complete with 278-mm OD wire-wound sand-screen casing	Open hole
Shot spacing	10 cm	10 cm
Data sampling rate	1 kHz sampled every 8 μs; 15 kHz sampled every 4 μs	8 μs
Probe diameter	39 mm	39 mm
Tool mode	Monopole	Monopole
Near to far-offsets	0.91 to 1.82 m	0.91 to 1.82 m
Receiver spacing	0.304 m	0.304 m
Transmitter central frequency	1, 3 and 15 kHz	1, 3 and 15 kHz
Data recording length	6.24 ms	4.25 ms
Number of transmitters	1	1
Number of receivers	4	4
Interval logged	300–417 m	300–413 m

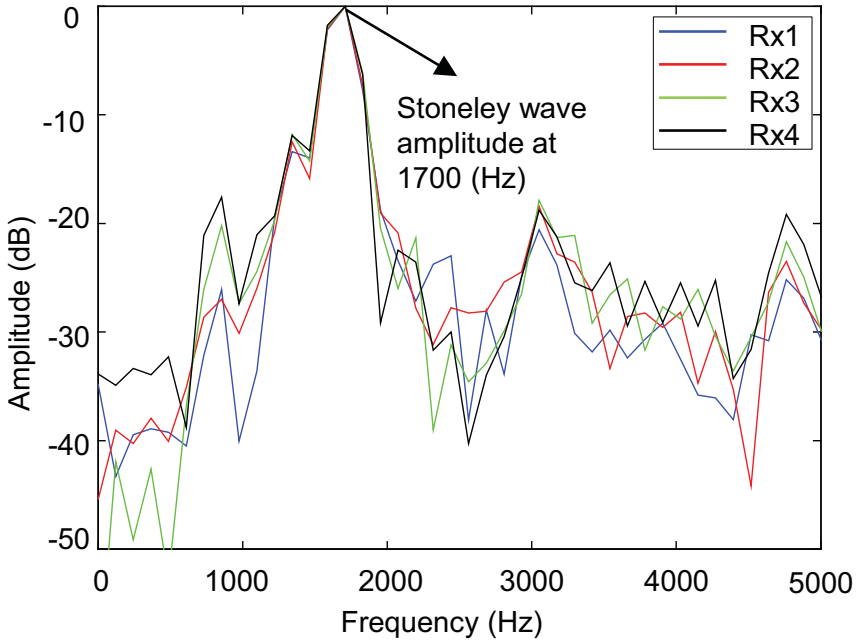

Figure 3-5. Frequency spectrum from four receivers at the M345-207 production well using a transmitter centre frequency of 1 kHz. The dominant frequency of the Stoneley wave peaks at 1700 Hz and the energy spectrum are closely matched for all of the receivers.

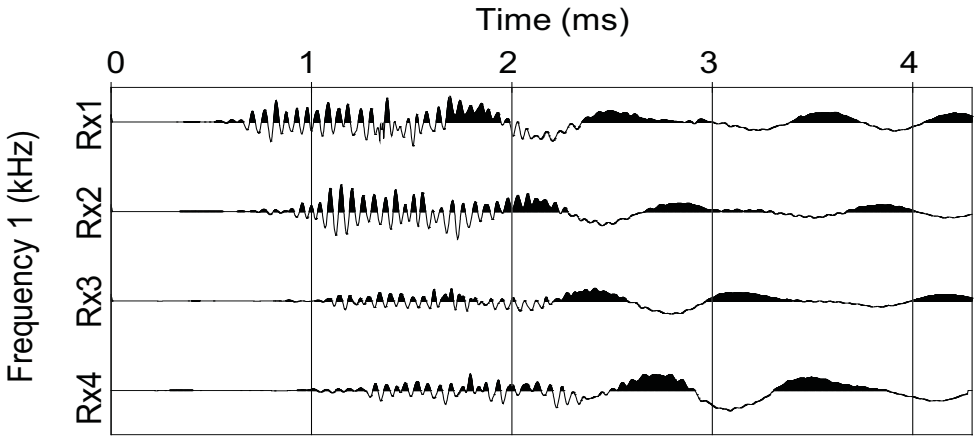

Figure 3-6. An example of data acquired at the open hole M345-109. The transmitter central frequency was set to 1 kHz. The data were acquired at a depth of 340.5 m with the single transmitter and four receivers (i.e., Rx1, Rx2, Rx3 and Rx4).

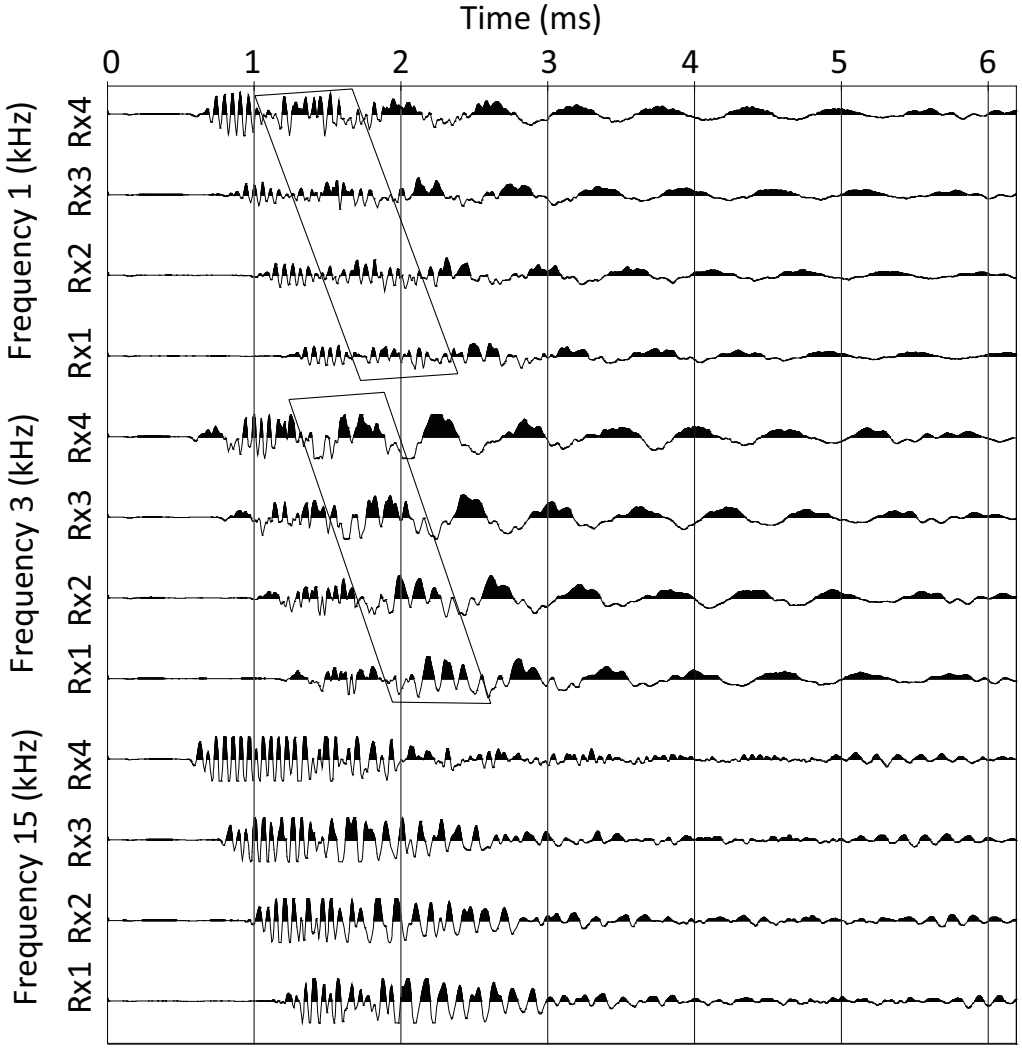

Figure 3-7. Multifrequency FWS data acquired with the four receivers (i.e., Rx1, Rx2, Rx3 and Rx4) in the M345-207 production well at a similar depth to that as shown in Figure 3-6. From the top, transmitter central frequencies are of 1, 3 and 15 kHz. Leaky modes (black boxes) are observed at all receivers in low frequency data sets (1 kHz and 3 kHz).

3.4.2 3D representation of dispersion image

We provide a new method that uses a 3D volume to interrogate phase velocity, frequency and coherency with depth. The 3D volume consists of 2D dispersion images generated at each measurement depth by the previously described phase-shift technique.

FWS measurements were collected at 10-cm intervals over a 116.4-m production zone, resulting in 1164 (2D) dispersion images (e.g., velocity versus frequency), which combine to form a 3D volume that spans the injection interval. The 3D volume is displayed as inline (frequency), crossline (phase velocity) and z-direction (depth). The 3D dispersion volumes are helpful when analysing rapid and/or small changes in dispersion with depth. This feature is particularly important for establishing whether a formation is sufficiently uniform for poroelastic theories to be useful.

3.5 Results

3.5.1 Full waveform dispersion image in the open-hole M345-109

It was important to compare the FWS data sets in the open hole and the completed production well. Dispersion images were derived from the 1 kHz FWS logging data acquired in the open hole M345-109 in frequencies up to 5 kHz. We present typical dispersion images in Figure 3-8 for (a) claystone, (b) siltstone and (c, d) sandstones. The gamma counts image is included in Figure 3-8 because it can be used to differentiate the sandstone (yellow), siltstone (green) and claystone (brown) intervals.

One feature common to FWS data propagation in the open-hole and the sand-screened production well is the presence of different modes. The low-frequency mode is dominant in the frequency range of approximately 0.7 to 2 kHz. (i.e., Stoneley wave energy). A second high-frequency mode typically dominates the spectral range from approximately 2 to 5 kHz. Our observation of a distinct high-frequency mode is consistent with that of Mavko et al. (2009), who suggested that the high-frequency mode in slow formations was predominately the leaky mode. As described earlier, the formations at the ASR site can reasonably be described as slow formations and given this, we would not expect pseudo-Rayleigh waves. It seems that the low-frequency modes in claystone and siltstone in Figure 3-8a and 3-8b, respectively, have phase velocities greater than the borehole fluid velocity in the open hole. This may be because there is an additional leaky mode that overlaps the

Stoneley wave mode at higher frequencies (see the white highlighted boxes in Figure 3-8a and 3-8b). This is one of the special characteristics of low-frequency modes in open-hole and slow-formation layers (claystone and siltstone). It is clear that several propagation modes exist and will overlap in frequency. Each mode will dominate (i.e., show stronger "amplitude" in the dispersion images) within a specific range of frequencies and as discussed, this range will depend on many factors. It requires sophisticated analytical techniques to separate the different propagated modes, in particular, where they overlap.

In Figure 3-8, focused energy is observed in low velocities (i.e., less than 500 m/s) in all data sets. This focused energy is marked as noise and is likely to be associated with the aliasing of FWS frequencies much higher than 20 kHz (Avila-Carrera et al., 2011). The phase velocities from 100 to 500 m/s physically do not represent any expected propagation mode. They are likely to be coherent noise or possibly aliasing. This focused energy also appeared throughout our 3D images and was not connected to geology or layering.

The low-frequency mode of the Stoneley wave in sandstone layers is shown in Figure 3-8c and 3-8d. As can be seen, the phase velocity of the low-frequency modes increases slightly with frequency (i.e., up to 2 kHz). In sandstone layers the phase velocity of the low-frequency mode will not exceed the velocity of sound in water as described early by Cheng and Toksöz (1982). The high-frequency mode in the sandstone layers has phase velocities that are greater than the borehole fluid velocity (i.e., the leaky mode). This high-frequency mode is typically expressed as a complex pattern in the dispersion images with the shape generally consistent with dispersion curves generated by Ellefsen et al. (1989).

In Figure 3-8 we observe a significant difference between the shape of the dispersion images for siltstone and claystone on one hand and sandstone on the other hand. The phase-velocity dispersion for the low- and high-frequency modes increases continuously with frequency in siltstone and clay layers. The shapes of the low-frequency mode for siltstone and claystone are in good agreement with the cases of a closed-pore wall whereby no fluid flow can penetrate into the siltstone or claystone. That is, we anticipate and observe no evidence for a "permeability effect" on the dispersion image.

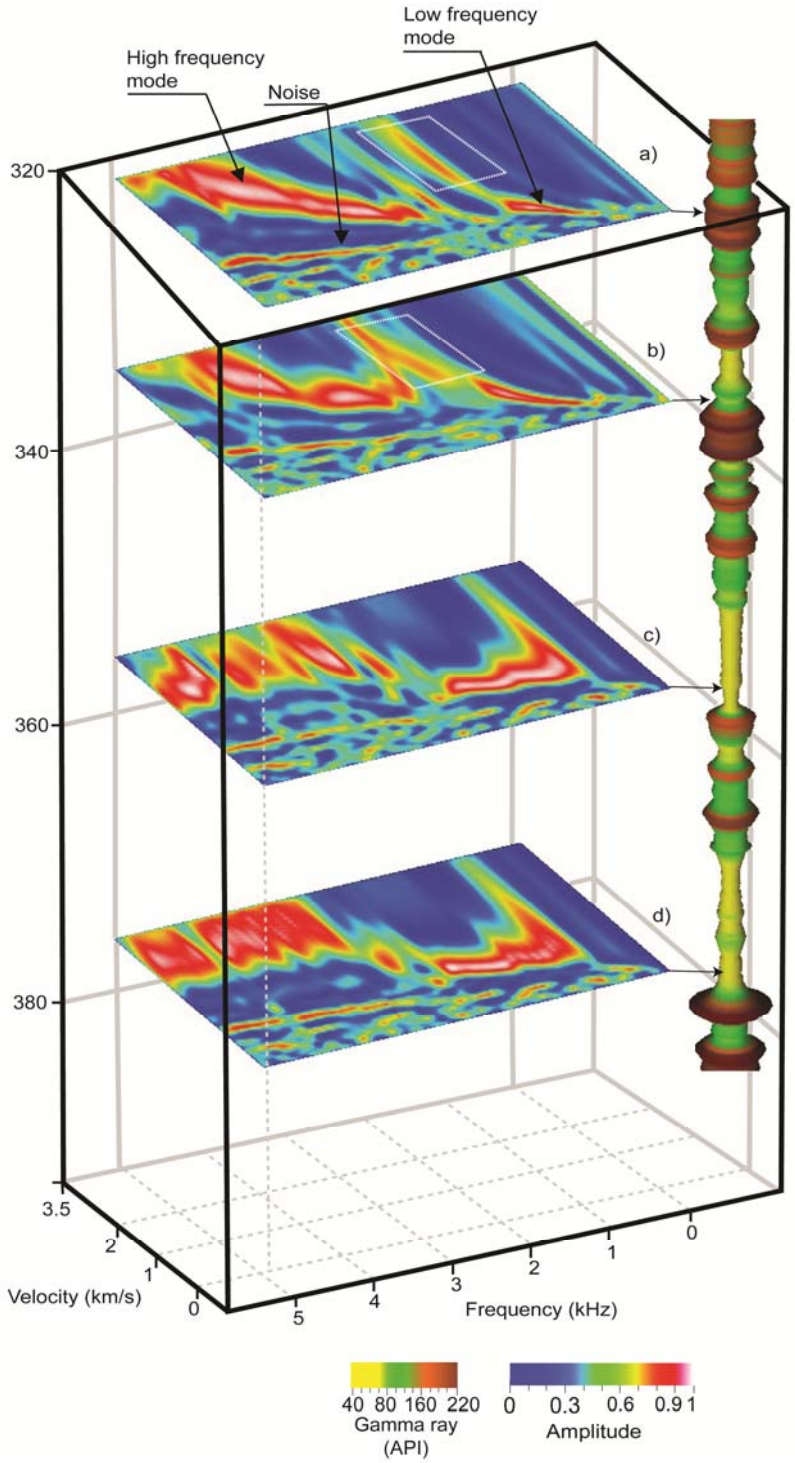

Figure 3-8. **Dispersion images for (a) claystone, (b) siltstone and (c, d) sandstone intervals in open-hole monitoring well M345-109. The Gamma counts on the right represent the claystone, siltstone and sandstone in brown, green and yellow, respectively.**

3.5.2 Dispersion in the large diameter sand-screened M345-207 production well

In the large-diameter sand-screened production well the approximate 51.5-mm annulus was left open so that the well could be naturally developed by collapsed formation materials during the jetting and airlifting processes (Rockwater, 2009). This well design must influence how the acoustic energy is distributed between the different wave-propagation modes.

The borehole annulus represents a high permeability zone between the sand screens and natural formation. The annulus is likely to be filled with sand; however, for some thicker shale intervals, it is possible that the annulus remains as a void space that contains only water. Figure 3-9a indicates the possibility of an additional fast dispersion mode that occurs adjacent to the high-frequency mode. As described previously, there are two types of tube waves (slow and fast) generated in the inner fluid column and the annulus. The fast mode is expected to disappear if the annulus becomes tightly packed with material that has similar acoustic properties to the formation material. This process is likely to be the case in the high-permeability sand-dominated intervals of M345-207 because the process of high-velocity jetting combined with airlifting will force the less consolidated coarse granular formation material into the annulus. Figure 3-9b provides an example of a phase-velocity dispersion image in sandstone where there is no indication of this additional high-frequency mode.

Figure 3-10 shows the dispersion image for claystone layers in the M345-207 production well using the 1 kHz transmitter central frequency data set. For the claystone layers, the velocity steadily increases with frequency as described for the open hole; however, we do observe crossover through the maxima in the phase velocity dispersion image; therefore, there are frequencies in which certain velocities for the claystone and sandstone could be identical.

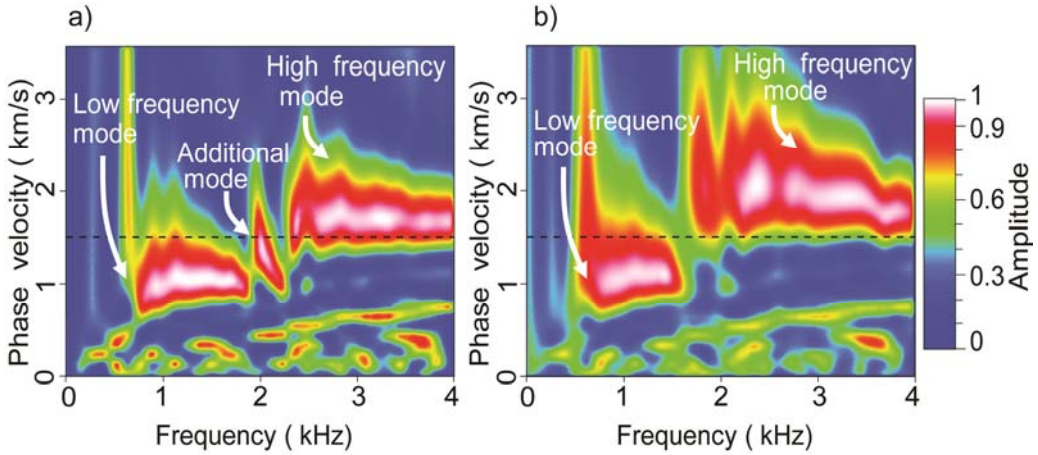

Figure 3-9. **The dispersion image at sandstone layers in the production well M345-207. (a) The additional acoustic mode is dominate over a narrow bandwidth and may be connected to the nature of the well annulus at a depth of 397 m. (b) The dispersion image in sandstone where there is no indication for the additional mode at a depth of 423.8 m. Both images are derived from the 1 kHz transmitter centre frequency FWS data set. The dotted line shows the maximum possible acoustic wave speed in water (i.e., approximately 1480 m/s).**

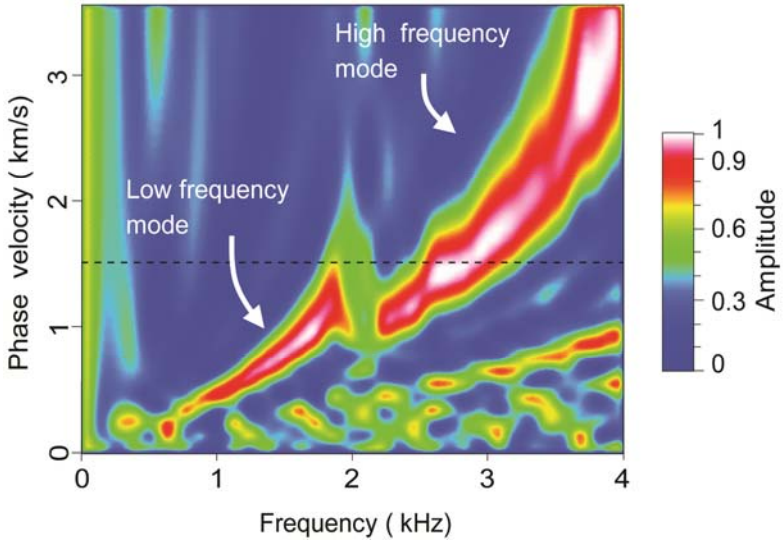

Figure 3-10. **The dispersion image for a claystone layer at a depth of 422.9 in the M345-207 production well using the 1 kHz data set.**

3.5.3 Comparison between the phase velocity dispersion images in the M345-109 open-hole and large diameter sand-screened M345-207 production well

A comparison of the gamma logs and geology in both wells indicates that the sediments are horizontally layered between the 40 m separated wells. In the following analysis we compare dispersion images from the same depth level and generally assume similar formation properties.

Figure 3-11 shows a comparison between (a) the phase-velocity dispersion image for sandstone derived from the 1 kHz FWS logs in the open hole and (b) the corresponding image for the production well. We observe that the shape of the dispersion images from similar depth levels in the large-diameter M345-207 production well and the M345-109 open hole are comparable. The main difference between the dispersion images in the open-hole and the production wells was the maxima of the phase velocities.

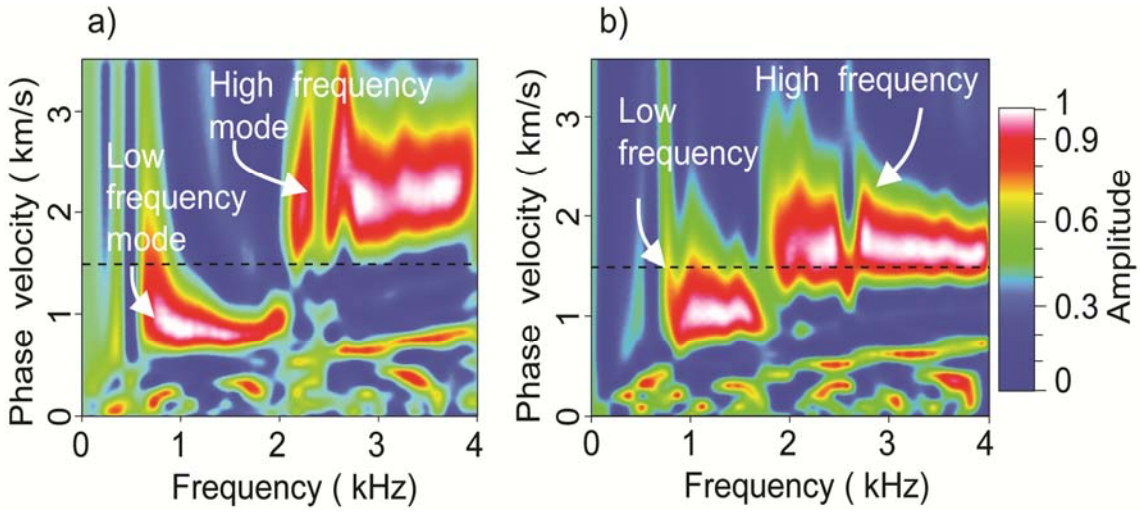

Figure 3-11. **A comparison between the dispersion images for sandstone in the (a) open hole M345-109 and (b) the production well M345-207 at a depth of 395 m using data sets acquired with a 1 kHz transmitter centre frequency. The high-frequency mode in the open hole has faster phase velocities compare to the production well. As expected the low-frequency mode is faster in the larger diameter production well.**

The mixture of sand and water in the annulus of the production well will likely create a lower velocity zone compared to the formation. The influence of the annulus on the distribution of energy is greater at high frequencies because the penetration of the wavefield into the formation becomes lower. In other words, as the frequency increases the particle motion will be increasingly dominated by the acoustic properties of the well annulus. As a result the high-frequency mode in the M345-207 production well is slower than that from the open hole M345-109. The waveguide energy at low frequency (i.e., Stoneley waves) in the production well must be influenced by materials and the geometry of the four cylindrical zones including the water, stainless-steel sand screens, sand-filled annulus and the natural formation. In Figure 3-11b, due to the presence of a stiffer casing material than the formation material (i.e., stainless steel), the velocity of the low-frequency propagated modes will increase accordingly, as previously presented in equation 3-7 (Norris, 1990).

3.5.4 Dispersion images and hydraulic conductivity over the production interval of the ASR site

The hydraulic conductivity derived from flow logs, phase-velocity dispersion derived from FWS data and gamma ray logs is integrated in a 3D representation and shown as Figure 3-12. Figure 3-12a and 3-12b shows phase-velocity dispersion images derived from independent FWS logging runs with transmitter centre frequencies set to 1 and 3 kHz, respectively. Both images display a single frequency slice taken through the 3D phase-velocity dispersion volume at 3 kHz. As described by Park et al. (1998), the resolving power of a dispersion image is a measure of stacked normalised amplitude at each frequency. The resolving power of the dispersion image in Figure 3-12b was higher for the data set acquired with the 3 kHz transmitter centre frequency compared with those runs with the transmitter centre frequency set to 1 kHz as shown in Figure 3-12a, especially in the upper part of the production well from 320 to 340 m. The higher resolution is likely to be because the spectral energy was greater over the key frequency band between 2 and 3 kHz, compared with the other data sets. It should be noted that the resolution or resolving power is in general lower for the high hydraulic conductivity zones (see, for example, the layer depth from 331 to 334 m). These zones tend to have a low-energy

level for the summed normalised amplitude displayed in the dispersion images. At this stage, we do not draw a conclusion about a direct relationship between high hydraulic conductivity and high attenuations because we also know that the highest hydraulic conductivity of coarse sandstone intervals can be very weakly consolidated. A further important point is that the images in Figure 3-12a and 3-12b are derived from independent wireline logs completed with different survey parameters (i.e., 1 and 3 kHz transmitter centre frequencies), yet they are well matched. In summary, velocity-dispersion images are shown to be repeatable even where logs are completed with different centre transmitter frequencies, provided sufficient S/N spans the frequency range at which targeted wave modes exist.

To explain the phase velocity variations a comparison between the dispersion phase velocity and the hydraulic conductivity can be made. We determined the phase velocity at different frequencies and plotted the values next to hydraulic conductivity. The results are illustrated in Figure 3-13. In Figure 3-13a we have sliced the 3 kHz 3D dispersion volume at frequencies of 2.5, 2.75, 3 and 3.25 kHz to recover the phase velocity at the maximum normalised amplitude from depths of 403 to 419 m. In Figure 3-13b, we have plotted an enlarged view that includes gamma, resistivity, hydraulic conductivity and phase velocity at the same selected frequencies. The interval is between depths of 408.5 to 415 m. At this latter interval the FWS logging tool passed over a thick sandstone interval where the hydraulic conductivity logs reach a high value of more than 28 m/day. We observe a wide range of hydraulic conductivities within the sandstone in which the distinct intervals are also characterised in the gamma and resistivity logs. In the highest hydraulic conductivity sandstone interval, high resistivity and high hydraulic conductivity are associated with low gamma counts, which are consistent with the clean coarse quartz-dominated sands. We also note that of the entire log (i.e., the screened intervals), the slowest phase velocities match with the highest hydraulic conductivity at a depth of 414 m below ground level.

The objective of our work was to present a case study for FWS logging in large-diameter production wells and to consider possible relationships between phase velocity and hydraulic conductivity distribution. The relationships we observe do not imply any particular rock physics model or even a direct connection between velocity dispersion and hydraulic conductivity. Such relationships provide a starting point from which empirical relationships can be established. In Figure 3-14, there is

a connection between the phase velocity and the higher hydraulic conductivity over a key sandstone interval between 400 and 417 m within the sand-screen production well M345-207. The relationship we show is between phase velocity at 3 kHz and hydraulic conductivity. We have also classified the cross-plotted points by colour based on the gamma logs. As can be seen, gamma counts cannot characterise hydraulic conductivity; however, it does broadly present the sand intervals where there is high hydraulic conductivity. We observe that at the highest hydraulic conductivities the phase velocities drop to 1450 m/s for this interval at this particular frequency (i.e., 3 kHz). Although Figure 3-14 shows some kind of a qualitative correlation at high hydraulic conductivity we would remind the reader that phase velocity is likely to be a function of frequency, together with many formation and well-construction parameters that combine to yield the dispersion image (see equations 3-1 and 3-7). That is, low phase-velocity does not necessarily indicate high hydraulic conductivity. New tools with broadband high-energy sources may assist future research in recovering high-resolution phase-velocity images over a greater frequency range. Certainly, we hope our work will motivate such developments.

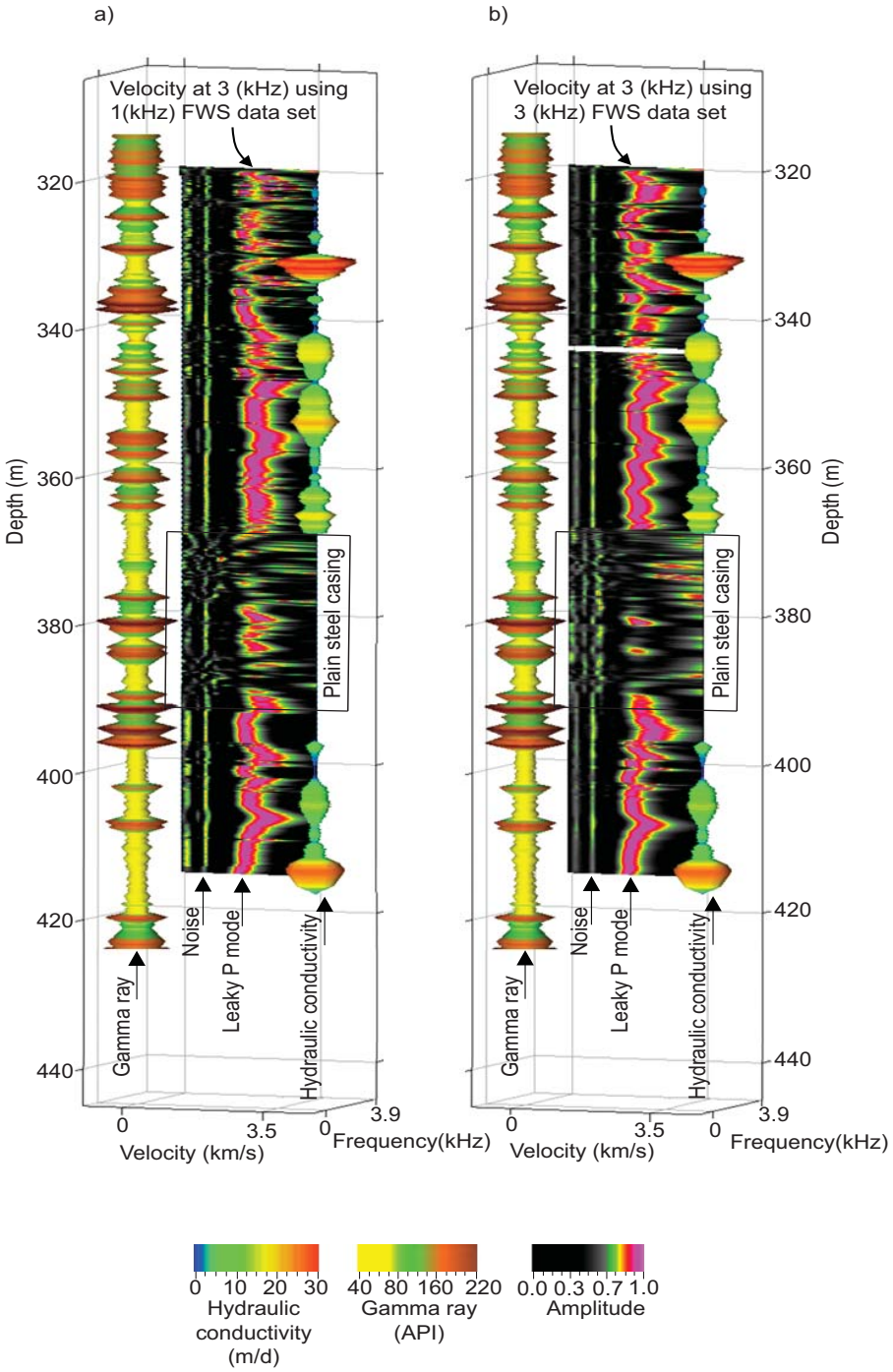

Figure 3-12. The 3D dispersion cube shows (a) the phase velocity of 1 kHz and (b) 3 kHz FWS data at a frequency slice of 3 kHz. The left and right tracks in (a, b) are gamma counts and hydraulic conductivity, respectively. The low amplitude between 369 and 394 m is due to the plain steel casing. The dispersion resolution is much higher in the 3 kHz data set, especially at shallow depth. The energy highlighted as noise is associated to the aliasing phenomena.

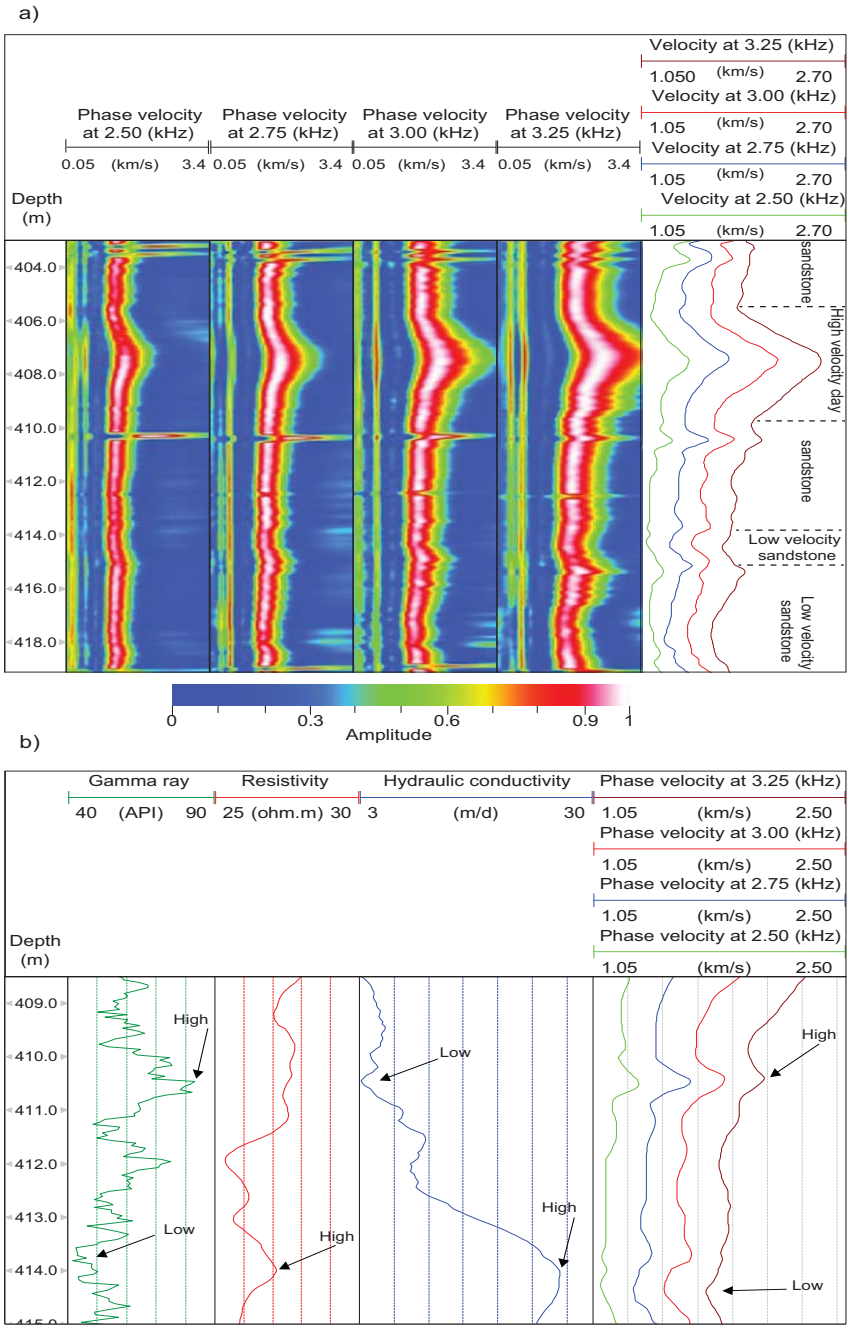

Figure 3-13. An image showing the correlation between phase velocity and formation properties. (a) The results of dispersion slices taken from the 3 kHz 3D dispersion cube at the following frequencies: 2.50, 2.75, 3.00 and 3.25 kHz. The maximum amplitude of the dispersion images is picked to obtain the phase velocity (right tracks). (b) The enlarged view of gamma counts, resistivity, hydraulic conductivity and phase velocities. In the high hydraulic conductivity zone, the phase velocity decreased at all selected frequencies.

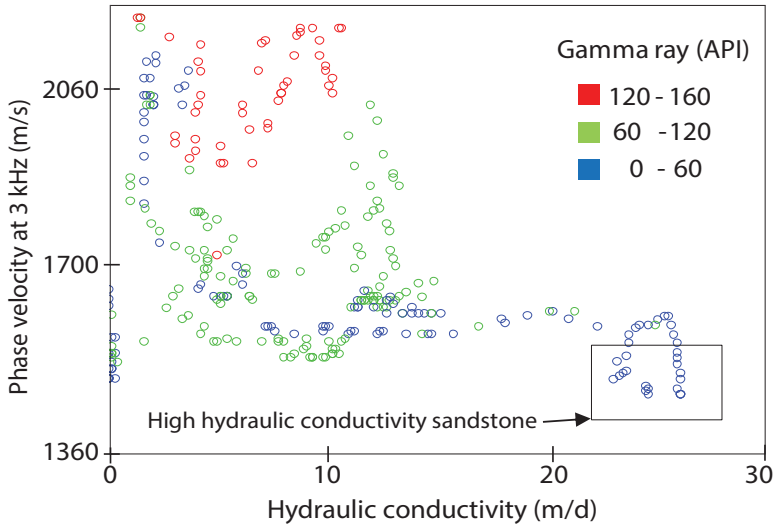

Figure 3-14. **The crossplot between hydraulic conductivity and phase velocity at a frequency of 3 kHz using a 3 kHz FWS data set between depths of 400 to 417 m. The formation lithology is classified by three categories based on the gamma log. The phase velocity drops to 1450 m/s at the highest hydraulic conductivity.**

3.6 Discussion

In water-well drilling the integrity of the mud rotary-drilled holes in soft sediments can begin to deteriorate soon after the driller pulls the bit out of the hole. As a result there is typically a short time window over which open-hole logging can be completed. The FWS experiments in the M345-109 open hole were completed during the night over an 8 h period after which the final monitoring installation was completed. The combination of time constrains, hole diameter and the fragility of the weakly consolidated sediments required that logging was completed rapidly with a lightweight slim-line acoustic logging tool with accurately fitted centralisers. Using heavy, long or large-diameter sonic logging tools in such circumstances would have been either impossible or could have placed the integrity of the hole at risk (i.e., increased the risk of hole collapse).

The production interval at the ASR site has extreme high and low hydraulic conductivity intervals repeating vertically throughout the screened production interval. The thickness of layers with similar petrophysical properties is an important characteristic when analysing any signal-coherence-based method (i.e., phase-velocity dispersion images). For example, the dispersion image in highly inhomogeneous layers may cause a broken coherency, especially at a high-frequency mode (Park et al., 1999). Here, the key parameter is the total separation between the set of receivers. For our FWS experiments the total distance between the first and last receiver was 0.91 m. Clearly, the sediments need to be relatively homogeneous over this interval for any intrinsic or general rock physics model to be applicable. Given the extreme and rapid vertical changes in sediment type at the ASR site, it would have been of little value to increase the length of the receiver array. In other words, there are very few intervals with similar rock properties for intervals greater than 0.9 m. It is expected that the impact of very thin layers or horizontal boundaries within the receiver set used for analysis could only be fully understood with physical or numerical modelling.

We note that for several phase-velocity dispersion images in the M345-207 production well there are small high-energy zones in the transition between low- and high-frequency modes (see Figure 3-9). These transitions do not occur in the dispersion images for the open hole M345-109 (see Figure 3-11a). Two possible explanations are as follows:

(1) The well annulus may not be completely filled with sediment during the jetting and well development phase. Therefore, any interval with an open annulus may have supported additional modes of wave propagation. Bakulin et al. (2009) describe the concept of Stoneley wave "splitting" in which two modes can be generated across the borehole completion.

(2) Another possibility is poor coupling between the formation and the wire-wound sand screens. This poor coupling may create an additional ringing mode (see Tubman et al., 1984). If the well annulus is incompletely filled or the casing is poorly coupled to the formation, then a sophisticated signal analysis is required. We would suggest that this will require new systematic field scale studies to reveal the complex relationship between the well completion and the FWS wireline logs.

The same sonic logging tool parameters and processing were used to facilitate our comparison of phase-velocity dispersion images in the open hole M345-109 and the production well M345-207. Although the velocities were different, the general character and shape of the dispersion images obtained in similar sediments were comparable. Figure 3-11 shows that a slightly higher phase velocity was observed in the low-frequency mode within the sandstone intervals of the production well. This result is broadly expected because of several parameters including the casing materials and diameter (see Tubman et al., 1984; Norris, 1990).

We observe a good correlation between the high gamma counts, claystone-dominated formations and the high-phase-velocity interpreted from the dispersion images at the high-frequency mode (see Figure 3-13a). One explanation often given for the higher phase velocity in claystone intervals is improved coupling. That is, if the claystones tend to swell then the formation and casing are well coupled (Henriet et al., 1983). However, this explanation is unlikely to apply at the ASR site because similar dispersion images are observed in the open hole M345-109 and the production well M345-207. Here we strongly suspect that the dispersion images are related to the nature and intrinsic properties of the claystones themselves.

Figure 3-15a and 3-15b can be used to compare the dispersion curves obtained in production well M345-207 and those from Ellefsen et al. (1989), respectively. Our dispersion curves in the sandstone layers reveal similar trends compared with the previous study of Ellefsen et al. (1989); however, for this current field experiment two aspects were unique. First, the wells intersect slow formations in which the P-wave velocities range from 1700 to 2900 m/s and second, the sandstone layers have exceedingly high permeability (i.e., ≥20 D). Note that the frequency range that we analyse is lower (i.e., up to 4 kHz) compared with the range analysed by Ellefsen et al. (1989) (i.e., up to 12 kHz). This difference in frequency may also depend on other parameters including the well diameter (see equation 3-7). Despite these differences the general characteristics of the sandstone dispersion curves are in good agreement.

It is noted that at the ASR site we have a range of hydraulic conductivities from negligible to greater than 40 m/day. There remains considerable debate concerning a possible connection between FWS propagation and hydraulic conductivity in coarse, weakly consolidated sandstone. In this regard, we would emphasise that our results

are based on a controlled field experiment from which we have recovered robust measurements of dispersion and hydraulic conductivity.

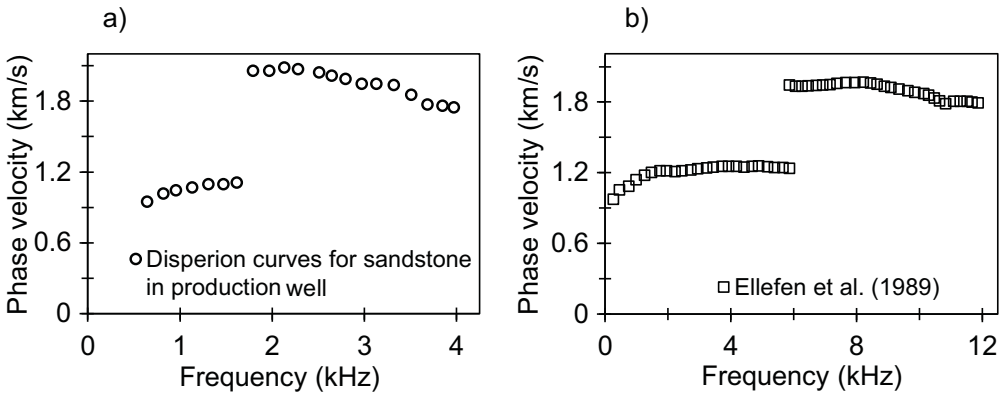

Figure 3-15. Comparison between (a) the dispersion curve for sandstone obtained in the M345-207 production well at a depth of 423.8 m and (b) the sandstone dispersion curve presented in Ellefsen et al. (1989). The general characters of the dispersion curves are similar. Note that the dispersion curve from the M345-207 production well was obtained at a lower frequency bandwidth.

3.7 Conclusions

Existing production wells must have at least one interval open to the subsurface so that fluid can move in or out of the well. We have shown that low-frequency FWS logging can be effective over such intervals in existing wells by comparing sets of multifrequency FWS wireline logging experiments in a large-diameter production well with an identical set of experiments completed in a nearby open hole. To analyse the FWS data, we obtained phase-velocity dispersion images and expressed the information as a 3D volume. We observed that at low frequency, the general characters of the phase-velocity dispersion images derived from the production well and the open hole are comparable. The main difference between the dispersion images in these wells is in the phase velocities' maxima. We consistently observe

that the shape of the high-frequency leaky mode in sandstone is different than those in claystone formations.

Our 3D phase-velocity volumes helped us with the analysis of FWS logs where formation layers exhibited rapid changes in the elastic and hydraulic properties over the production interval at the ASR site. We found that the low phase velocity at a frequency of 3 kHz within the sandstone-dominated formations could be correlated to high hydraulic conductivity in the production well.

The character of the phase-velocity dispersion curves in sandstone layers for the production well showed good agreement with the character of the dispersion curves obtained by previously published works.

A key conclusion is that the phase-velocity dispersion images extracted from low-frequency FWS wireline logging and completed over the sand-screened interval hold considerable information that could potentially be used for time-lapse monitoring of sanding, mechanical failure, well clogging, or any other change in near-well conditions. In short, FWS sonic logging in a production well is highly repeatable and can be applied at any point in the life of a well without impacting the well or near-well environment in any way.

3.8 References

Avila-Carrera, A., J. H. Spurlin, and C. Valle-Molina, 2011, Simulating elastic wave propagation in borehole: Fundamentals of seismic response and quantitative interpretation of well log data: Geophysical international, **50**, 57–76.

Burns, D. R., 1986, Formation property estimation from guided waves in a borehole: Massachusetts Institute of Technology.

Bakulin, A., D. Alexandrov, A. Sidorov, and B. Kashtan, 2009, Acoustic waves in sand-screened deepwater completions: Comparison of experiments and modelling: Geophysics, **74**, 45–56.

Bakulin, A., M. Jaaskelainen, A. Sidorov, and B. Kashtan, 2008a, Downhole acoustic surveillance of deepwater wells: The Leading Edge, **27**, 518–531.

Bakulin, A., A. Sidorov, B. Kashtan, and M. Jaaskelainen, 2008b, Real time completion monitoring with acoustic waves: Geophysics, **73**, 15–33.

Bakulin, A., B. Gurevich, R. Ciz, and S. Ziatdinov, 2005, Tube-wave reflection from a porous permeable layer with an idealized perforation: 75th Annual International Meeting, SEG Expanded Abstracts, 332–336.

Biot, M. A., 1952, Propagation of elastic waves in a cylindrical bore containing a fluid: Journal of Applied Physics, **23**, 997–1005.

Chang, S., H. Liu, and D. Johnson, 1988, Low-frequency tube waves in permeable rocks: Geophysics, **53**, 519-527.

Cheng, C. H., and M. N. Toksoz, 1982, Generation, propagation and analysis of tube waves in a borehole: Presented at the 23th SPWLA Annual Logging Symposium.

Cheng, C. H., J. Z. Zhang, and D. R. Burns, 1987, Effects of in-situ permeability on the propagation of Stoneley (tube) waves in a borehole: Geophysics, **52**, 1297–1289.

Crain, E. R., 2004, How many acoustic waves can dance on the head of a sonic log?: CWLS Newsletter, http://www.cwls.org/docs/insite/insite_april_2004.pdf, accessed 14July 2012.

Descourvières, C., N. Hartog, B. M. Patterson, C. Oldham, and H. Prommer, 2010. Geochemical controls on sediment reactivity and buffering processes in a heterogeneous aquifer, Applied Geochemistry, **25**(2): 261–275.

Franco, J. L., M. A. Ortiz, G. S. De, L. Renlie, and S. Williams, 2006, Sonic investigation in and around the borehole, Oilfield, Spring, **18**, 14–33.

Ellefsen, K. L., C. H. Cheng, and K. M. Tubman, 1989, Estimating phase velocity and attenuation of guided waves in acoustic logging data: Geophysics, **54**, 1054–1059. http://dx.doi.org/10.1190/1.1442733.

Mavko, G., T. Mukerji, and J. Dvokin, 2009, The rock physics handbook: Tools for seismic analysis of porous media: Cambridge University press.

Henriet, J. P., J. Schittekat, and P. H. Heldens, 1983, Borehole seismic profiling and tube wave application in a dam site investigation: Geophysical Prospecting, **31**, 72–86.

Karpfinger, F., 2009, Modelling borehole wave signatures in elastic and poroelastic media with spectral method: PhD thesis, Curtin University.

Malajczuk, S., 2010, Time-lapse thermal and induction logging in the near-well environment, Perth Basin WA: BSc thesis, Curtin University.

Norris, A. N., 1990, The speed of a tube wave: Acoustic Society of America, **87**, 414–417.

Paillet, F. L., 1980, Acoustic propagation in the vicinity of fractures which intersect a fluid-filled borehole: Presented at the 21st SPWLA Annual Logging Symposium, paper DD.

Paillet, F., and C. H. Cheng, 1986, A numerical investigation of head waves and leaky modes in fluid-filled boreholes: Geophysics, **51**, 1438–1449.

Park, C., R. Miller, and J. Xia, 1998, Imaging dispersion curves of surface waves on multichannel records: 68th Annual International Meeting, SEG, Expanded Abstract, 1377–1380.

Park, C. B., R. D. Miller, J. H. Xia, J. A. Hunter, and J. B. Harris, 1999, Higher mode observation by the MASW method: 69th Annual International Meeting, SEG, Expanded Abstract, 524–527.

Rao, V. N., and J. K. Vandiver, 1999, Acoustics of fluid-filled boreholes with pipe: Guided propagation and radiation: Acoustic Society of America, **105**, 3057–3066.

Rockwater Pty Ltd, 2009, Mirrabooka aquifer storage and recovery trial: Bore completion and hydrogeological evaluation: Report no 236.20.4/09/01, Water Corporation.

Rockwater Pty Ltd, 2011, Mirrabooka aquifer storage and recovery trial—results and technical review for cycle 2: report no 236.20.4/11/1: Water Corporation.

Rosenbaum, J. H., 1974, Synthetic microseismograms: Logging in porous formations: Geophysics, **39**, 14–32.

Staal, J. J., and J. D. Robinson, 1977, Permeability profiles from acoustic logging: the 52nd Annual Fall Technical Conference, SPE, 6821.

Tang, X. M., and C. H. Cheng, 1993, Borehole Stoneley waves propagation across permeable structures: Geophysical Prospecting, **41**, 165–187.

Tezuka, K., C. H. Cheng, and X. M. Tang, 1997, Modelling of low-frequency Stoneley wave propagation in an irregular borehole: Geophysics, **62**, 1047–1058.

Tichelaar, B. W., and K. W. Luik, 1995, Sonic logging of compressional-wave velocities in a very slow formation: Geophysics, **60**, 1627–1633.

Tubman, K. M., C. H. Cheng, and M. N. Toksoz, 1984, Determination of formation properties in cased boreholes using fullwave acoustic logs: 25th Society of Professional Well Log Analysts, CC1–CC19.

Water Corporation, 2010, Engineering review. Aquifer Storage and Recovery (ASR), Mirrabooka M345- design, installation and commissioning. Asset management division, Mechanical and electrical service branch, Document No: 2536-ER-01, April 2010.

Weatherford, 2010, Routine core analysis final report of Mirrabooka-345: Weatherford Laboratories.

White, J. E., 1962, Elastic waves along a cylindrical bore: Geophysics, **27**, 327–333.

White, J. E., 1983, Underground sound: Application of seismic waves, Elsevier Scientific, New York.

Williams, D. M., J. Zemanek, F. A. Angona, C. L. Dennis, and R. L. Caldwell, 1984, The long space acoustic logging tool: Presented at the 25th Annual Logging Symposium Transaction: Society of Professional Well Log Analysts, paper T.

Wu Peter T., H. Darling, and D. Scabbier, 1995, Low frequency P-wave logging for improved compressional velocity in slow gas zones: 69th Annual International Meeting, SEG, Extended Abstract, 9–12.

Xu, C., and M. Martin, 2008, Assessing impacts of confined abstraction on the Ganagara Mound using transient response functions: Water Down Under.

CHAPTER 4 : Changes in P-Wave Velocity with Different Full Waveform Sonic Transmitter Centre Frequency[2]

In this chapter, I have considered the possibility of apparent P-wave dispersion and its meaning in shallow, moderately consolidated to unconsolidated sandstone formations. Recovery of the complete P-wave dispersion was not considered possible; however, semi-quantitative methods for analysing changes in velocity with frequency (i.e., between 1 and 15 kHz) were developed. Although quantitative results of apparent P-wave dispersion were difficult to obtain from the field data, it is reasonably clear that small-scale structures in these shallow sandstones are significant factors in determining variations in apparent P-wave velocity dispersion. The content of this chapter has been submitted to the journal *Exploration Geophysics*. The material is currently undergoing second round review.

2. Almalki, M., Harris, B. and Dupuis, C.J. 2013. Changes in P-wave velocity with different full waveform sonic transmitter centre frequency: Exploration Geophysics, Manuscript EG 13037.

4.1 Summary

Full waveform sonic logging, with the transmitter set at different centre frequencies, often provides different compressional wave velocities over the same interval. There may be several reasons why these velocity differences are recovered where the source has different frequency content. Examples include: intrinsic dispersion, scattering dispersion, geometric dispersion, processing artefacts and acquisition artefacts. We acquired and analysed multifrequency monopole full waveform sonic logging data from the cored drill hole intersecting a high-permeability sandy aquifer in the Northern Gnangara Mound, Perth Basin Western Australia. A key interval of the shallow, sand-dominated Yarragadee Formation was selected and logged four times with transmitter centre frequencies set to 1, 3, 5 and 15 kHz. We consider possible reasons for variations in velocity and in particular, consider possible relationships between apparent dispersion of P-wave velocity, hydraulic permeability and broad divisions between sedimentary structures.

Field examples of direct or indirect relationships between signals recorded by seismic methods and in-situ permeability in very high permeability sandstones are exceedingly rare. These relationships are investigated using high-precision in-hole sonic measurements. We computed apparent velocity dispersion as the percentage velocity differences in the P-wave velocity recovered from full waveform sonic logs completed at different dominant transmitter centre frequencies. We found that high permeability sediments could be placed into broad groups: cross-bedded and non-cross-bedded sandstones.

We find a distinctly different relationship between apparent P-wave velocity dispersion and permeability for cross-bedded and non-cross-bedded sandstones. The grain size of these two sediment categories ranges from fine to gravel. Cross plots for both sediment types show a general trend of increasing apparent dispersion with increasing permeability. Grouping the sandstone layers based on sediment type, as observed from core samples, illustrates different but positive correlation between the apparent P-wave velocity dispersion and permeability in these shallow, weakly-consolidated sandstones. The cross-bedded sandstone, for its part, has a wider range of permeability than the non-cross-bedded sandstone but a smaller range of apparent P-wave velocity dispersion. Given these results our hypothesis is that while

permeability plays a role, other factors such as geometric dispersion or scattering dispersion likely contribute the net value of P-wave dispersion recovered between any two receivers. Finally the results from these experiments have shown that there exists at least a weak empirical relationship between P-wave velocity dispersion and hydraulic permeability at the field site.

4.2 Introduction

Full waveform sonic (FWS) logging provides measurements that are often used in hydrocarbon, groundwater, coal and geothermal exploration to investigate near-well lithological, hydraulic and mechanical properties. The FWS acoustic tools emit broadband seismic source energy that typically focus somewhere in the frequency range from 1 to 30 kHz. The new generation of slim-line multifrequency sonic acquisition equipment provides the potential for a better understanding of poroelastic mechanisms through the analysis of multiple sonic logs acquired at different centre frequencies (Mount Sopris Instruments Inc, 2002). Although FWS data have been used for a wide range of objectives, analysis of the differences in the P-wave velocities measured at different transmitter frequencies is an ongoing research problem for applications such as the characterisation of permeability and the classification of small scale sedimentary structures. Although P-wave velocity dispersion has been the subject of numerous numerical and theoretical studies (Ba et al., 2008a & b; Batzle et al., 2006; Gurevich et al., 1997; Pride, 2005; Vogelaar, 2009; David and Zimmerman, 2013; Sam et al., 1997), there remains a remarkable lack of published field trials (e.g., Pun et al., 2010), particularly for shallow sandy environments.

The acquisition of FWS sonic data in high-permeability, moderately consolidated to unconsolidated sandstones presents many challenges. The first challenge is that the drill hole can only remain open for a limited time following the completion of drilling. Logging must be undertaken immediately after the drilling activity is completed and prior to the addition of any well completion. There have been laboratory studies that have investigated sediments from shallow formations at very low confining pressures (i.e., from less than 100 to 2000 kPa) (Zimmer, 2004); however, few multifrequency FWS wireline data sets have been collected in shallow

weakly-consolidated sandstones. In particular, no data sets have been acquired in the study site, the Perth Basin of Western Australia, using multiple transmitter frequencies, which is probably because of the cost and the potential risk of hole collapse while logging an open hole. In fact, the relationship between P-wave dispersion and rock heterogeneity has not been rigorously defined from well-log data because the measurement of heterogeneity from sub-centimetre to several meters is problematic.

In this study, we acquired and analysed multifrequency FWS data for aquifers that are known to contain 'friable' sands along with moderately-consolidated sandstones. We consider both laboratory measurements on core samples (i.e., permeability and sediment structures) and multifrequency FWS well logs. Our objective is to recover information that may be hidden in the frequency content of the first arrival wavelet (i.e., the P-wave). For this research, the term 'apparent dispersion' is used to describe any velocity change related to traveltime that is obtained from logs acquired at different transmitter centre frequencies.

4.2.1 Site conditions

The study site is located in the Northern Gnangara Mound, Perth Basin, Western Australia (Figure 4-1). The Gnangara Mound is considered to be the most important groundwater aquifer recharge area for Perth (Western Australia Planning Commission, 2001). The FWS experiments were performed at the open-cored drill hole NG3 immediately after drilling. This drill hole intersected the hydrogeologically important Yarragadee aquifer that has moderately consolidated to unconsolidated sandstones. Borehole NG3 was drilled to a depth of 200 m below ground surface.

Figure 4-2 shows the unconsolidated nature of the sandstones recovered at the study site. Core recovery and condition varied with depth. For example, the shallow part of the borehole to depths up to 90 m consisted of poorly consolidated to loose sands. Core recovery improved after this particular depth. Visual analysis of the intact core samples was used to categorise sedimentary types (Wilson and Garcia, 2009). The sedimentary structure of the study site could be categorised as cross-bedded or non-cross-bedded sandstone. Each category exhibited a wide variety of grain size and permeability. The sandstone for both groups consisted of planar

laminations, very coarse gravel lenses or laminae and centimetre-scale variations in grain size (Wilson and Garcia, 2009). The total fraction of cross-bedded sedimentary structures increased with depth, especially below 140 m. In general, the Yarragadee Formation has a consistent dip of 7 degrees to the East. Figure 4-3 shows the dipping layers of Jurassic Yarragadee formation, below the Neocomian unconformity, on a high resolution 2D seismic section that is approximately 2.1 km to the south of the NG3 cored drill hole.

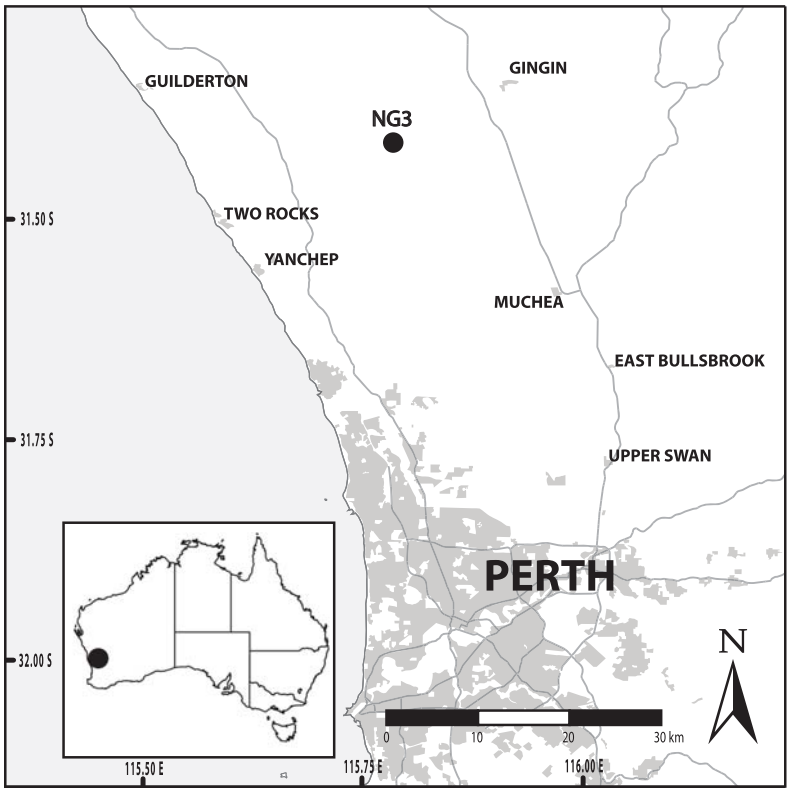

Figure 4-1. The study map shows borehole NG3, which was used to acquire the FWS data.

Figure 4-2. An example of core recovery and condition from drill hole NG3 from a depth of 50 to 70 m. These shallow sandstones are poorly-consolidated and core loss was common.

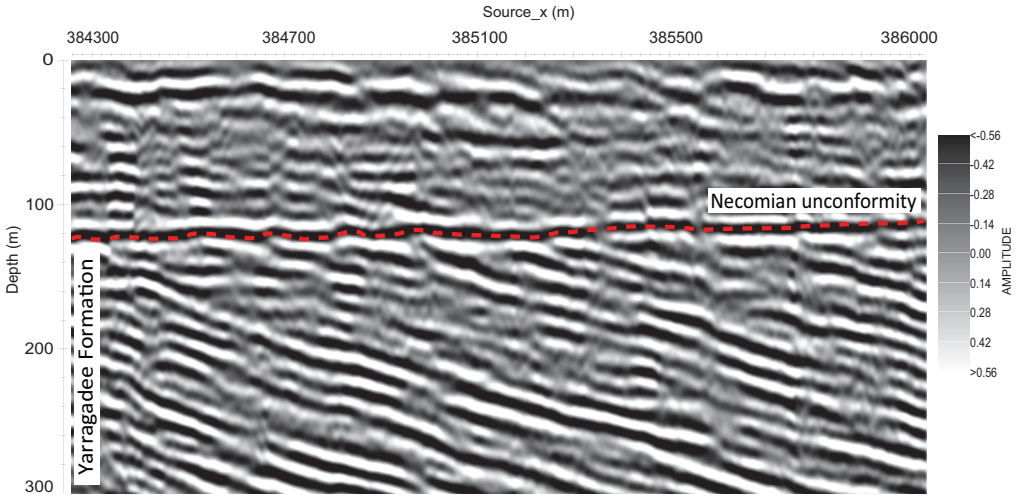

Figure 4-3. Seismic section shows the main characteristic of Yarragadee formation at the study site.

4.2.2 A theoretical background on P-wave dispersion

At well-log frequencies from 1 to 30 kHz, the prediction of P-wave dispersion has several limitations, mainly associated with the difficulties in distinguishing between geometric factors related to the borehole environment and the formation's physical parameters. These physical parameters controlling the types of dispersion mechanisms observed in sedimentary formation are not entirely understood. For example, the observed dispersion obtained from FWS data in sedimentary rock will

often be a combination of intrinsic, scattering and geometric dispersion. The contribution of each type of dispersion may vary considerably depending on the formation, its hydraulic parameters and the drill-hole conditions (e.g., filter pack and mud invasion etc.). Table 4-1 defines several types of dispersion that can occur at FWS frequencies.

The nature of seismic wave propagation is affected by the heterogeneity of the rock, the pore fluid (Sato et al., 2012) and its mobility within the rock (i.e., mobility m is the relationship between permeability κ and viscosity η, $m = \frac{\kappa}{\eta}$). Wave-induced fluid flow (WIFF) is a dispersion and attenuation mechanism that is affected/controlled by the hydraulic properties of the rock (e.g., Müller et al., 2005, 2010). When a compression wave passes through heterogeneous rocks, the variations in rock properties are likely to generate pressure gradients and fluid flow. The induced fluid flow is classified based on the scale length of the pressure gradient. The spatial scale of the induced fluid flow is divided into three categories: macroscopic (Biot's global flow), mesoscopic (local flow) and microscopic (squirt flow) (e.g., Pride et al., 2004). Mesoscopic fluid flow occurs at a scale much larger than the pore size but smaller than the seismic wavelength (Müller et al., 2010). That is, the scale length of heterogeneities is governed by the relationship given by

$$a_{pore} \ll a_{meso} \ll \lambda, \qquad \textbf{4-1}$$

where a_{pore} indicates the pore size, λ is the wavelength of dominant frequency of the seismic wavelet and a_{meso} is the estimated length of heterogeneities through which fluid flow can occur (Rubino et al., 2012; Caspari et al., 2013). The WIFF mechanism is important in sedimentary basins where heterogeneity and a wide variation in permeability is commonly observed. The WIFF mechanism for mesoscopic heterogeneities is a fluid pressure diffusion process. For the equations below, the diffusion length L_d is the size of heterogeneities (Rubino et al., in press; Biot, 1956; Caspari et al., 2013):

$$L_d \equiv \sqrt{D/\omega_c} \simeq a_{meso}\ , \qquad \textbf{4-2}$$

where ω_c and D are the characteristic frequency and the pressure diffusivity, respectively. The mesoscopic flow will cause a significant dispersion if mesoscale heterogeneities with substantial different elastic compliances exist. The pressure diffusivity in terms of poroelastic properties is expressed in early work of Dutta and Odé (1979). The pressure diffusivity can be given as

$$D = \frac{\kappa}{\eta}\left(\frac{LM - \alpha^2 M^2}{L}\right), \tag{4-3}$$

where κ and η represent the permeability and fluid viscosity (Batzle et al., 2006; Rubino et al. 2012; Rubino et al., in press). The parameters α, M, and L are given as

$$\alpha = 1 - \frac{K_m}{K_s}, \tag{4-4}$$

$$M = \left(\frac{\alpha - \varphi}{K_s} + \frac{\varphi}{K_f}\right)^{-1}, \tag{4-5}$$

$$L = \lambda_u + 2\mu, \tag{4-6}$$

where K_m, K_s and K_f represents the bulk moduli of the dry matrix, solid grains and fluid, respectively (e.g., Rubino et al., 2012; 2009). The parameters μ, φ and λ_u are the shear modulus of the bulk material, the porosity of the rock and the saturated Lame parameter.

Table 4-1. Summary of reasons why P-wave velocity may change with frequency in field sonic logging data.

Type of dispersion	description
1. Intrinsic: a) Biot's global flow b) Wave-induced fluid flow (local flow) c) Squirt flow	a) This is the dispersion expressed by Biot (1956a, 1956b, 1962). It is related to energy losses caused by relative movement of the grain material and fluid. Values from a few per cent per decade may be expected depending on several parameters including permeability. Biot's so called 'global flow' is relevant in laboratory measurements. b) A second mechanism that occurs in the presence of mesoscale heterogeneities is wave- induced (or local) fluid flow. References include: Norris (1993), Gurevich and Lopatnikov (1995), Gelinsky and Shapiro (1997) and Sam et al. (1997). In both cases a) and b) dispersion is positive (i.e., for the same rock, velocity at the high-frequency limit is higher than at the low-frequency limit). c) Squirt flow dispersion may occur when seismic waves compress a saturated porous rock with grains having micro-cracks; the crack portions will have a greater fluid pressure than the pore space. This will cause fluid flow from the crack to the pore (Mavko and Nur, 1975). The rate at which this can occur is frequency dependent. Squirt flow dispersion is less likely in high-permeability shallow porous rocks but should be considered. It has been found that the amount of attenuation caused by squirt flow is not enough to explain measured attenuation in the seismic frequency band (1-10^4 Hz) (Pride et al., 2004). The squirt mechanism focuses on the microscopic grain scales (grain contacts and microcracks in the grains) to describe viscous losses (Jones, 1986). Other reference include: Jones (1986), O'Connell and Budiansky (1977), Mavko and Nur (1975, 1979), Palmer and Traviolia (1980), Murphy et al. (1984), Johnston et al. (1979), Winkler et al. (1985), Sams et al. (1997) and Pride et al. (2004).
2. Scattering	Scattering dispersion (e.g.,Müller et al., 2008) can be connected to backscattering from the rock heterogeneity, where energy is transferred from the first arrival waves into waves propagating in all directions causing scattered attenuation and dispersion (Pride et al., 2004). Scattering can potentially result in a local phenomenon where the amplitude can be enhanced (e.g., as found in reflection seismology). The dispersion is caused by interference effects and scattering from heterogeneities, such as thin-bedded layers (Jones, 1986). This type of dispersion is typically positive.
3. Geometric	Geometric dispersion is simply a consequence of longer wavelengths propagating through larger volumes of rock. For example, the drilling process must influence the very-near-well setting so that high frequencies will tend to be more influenced by the effects of drilling (mud invasion, the filter pack built up by drilling, formation damage, etc.). In most cased the drilling process tends to disturb the very-near-well setting so there would be an expectation that geometric dispersion would be negative with the lower frequencies being less affected by the very-near-well setting (e.g., less than 10 cm around the well or drill hole) (Khan and Rees, 1967).
4. Overlapping wave modes	Overlapping wave modes are essentially a processing artefact. For example, at near offsets in slow formations the direct wave travelling in the water column may sit so closely behind the critically-refracted head wave travelling in the formation that the two are difficult to separate. The problem of waveform separation changes with frequency may result in the creation of an artificial dispersion.

Sato et al. (2012) state that if the fluid mobility in the sands is high, then the dispersion of P-waves can occur in both the seismic and sonic frequency bands. Sams et al. (1997) observed the dispersion of P-waves in the sonic frequency bandwidth from 8 to 24 kHz. Best and Sams (2003) found significant velocity dispersion at a sonic frequency of 10 kHz in sandstone. In our case study, the fluid is water and saturation is 100% so viscosity is uniform and known. Solute concentration is low in this shallow aquifer system (i.e., less than 500 mg/L). Also, low solute concentration, cellulosic, polymer-based drilling muds were used to 'hold back' delicate formations while providing minimal impact on the aquifer chemistry and hydraulics proximal to the hole.

The estimation of permeability from the multifrequency P-wave velocity derived from acoustic data remains an important unsolved problem in applied geophysics. Several researchers have considered the relationships between seismic velocity, seismic attenuation and hydraulic parameters (e.g., Bourbie et al., 1987; Pride et al., 2003). Prasad (2003) presented a relationship between the P-wave velocity and permeability by considering a 'flow zone indicator' (FZI). Han and Nur (1987) showed overwhelming experimental evidence that the dispersion of compressional velocity measured at ultrasonic frequencies ranges from 1 to 6% in fairly well-cemented sandstone and from 2 to 9% in less-cemented sandstone. They concluded that there was no correlation between dispersion and porosity in compacted and well-cemented sandstone.

4.3 Method

4.3.1 Full waveform sonic acquisition

The multifrequency FWS field experiment was completed with the slim-line Mount Sopris Full Waveform Sonic wireline logging system. Figure 4-4 shows a simplified illustration of the wireline logging tool (Mount Sopris Instruments Inc, 2002). Two centralisers are located at the upper and lower parts of the tool probe to ensure centralisation within the vertical drill hole. The FWS tool consists of four receivers separated by 0.3048 m and one transmitter with an offset to the nearest receiver of 0.9144 m.

Multifrequency FWS data were generated using a single sonic transmitter with centre frequencies of 1, 3, 5 and 15 kHz. These measurements were repeated over the same depth interval. Similar tool configuration and recording parameters were used for FWS logging as shown in Table 4-2. The main difference in logging parameters between the repeated surveys was the recording length, which was set shorter for the FWS experiment acquired with 15 kHz.

The transmitter spectral energy was focused closer to the selected transmitter frequency; however, the spectral energy of the signal remained relatively broadband for all logs. To explore the nature of the source's waveform and frequency, we conducted experiments in a large fresh water area (i.e., a swimming pool) where the effect of surrounding media is negligible. Figure 4-5 and 4-6 shows respectively the amplitude spectrum and the source waveform at three selected central frequencies of 1, 15 and 20 kHz. In Figure 4-5, the dominant energy of the P-wave appears to be excited at 15 kHz and as such it is present in all records irrespective of the frequency selected by the operator. That is, spectrum is not purely band limited based on the selected transmitted frequency but has a range of 1 to 30 kHz with the maximum frequency shifted toward the selected transmitter frequency. Further, the waveforms in Figure 4-6 show a slight difference in the frequency content of the P-wave. Put simply, in a large body of water we observe no change in velocity of acquired data. As expected there is no dispersion in water.

Figure 4-7 shows examples of FWS data recorded with four different central frequencies of 1, 3, 5 and 15 kHz, at a depth of 66.7 m below ground surface. Note that the receiver gain was applied to the recorded signal at larger receiver offsets to account for the lower amplitude of first arriving wavelet. The selected gains were 1, 4, 8 and 16 dB for Rx1, Rx2, Rx3, and Rx4, respectively. This is the reason why the first arrival amplitude (i.e., highlighted by solid lines) received on Rx1 was less than the arrival amplitude received on Rx4 in Figure 4-7. Our principle interest is in the first arriving wavelet recorded with transmitter frequencies of 1 and 15 kHz on receivers Rx1 and Rx2 as they appear to be free from the contaminating effects of other wave modes. Note that the wave mode separation is better in the data set acquired with a 1 kHz transmitter centre frequency. The relatively high amplitude of the leaky P modes, which contains considerable and broader spectral energy than the first arriving pulse, is clear in all sonic records especially for the data acquired with 1 kHz transmitter centre frequencyas highlighted by dash line in Figure 4-7. The 15

kHz data is clipped due to the effect of the gain, which was set optimally for the first arriving wavelet.

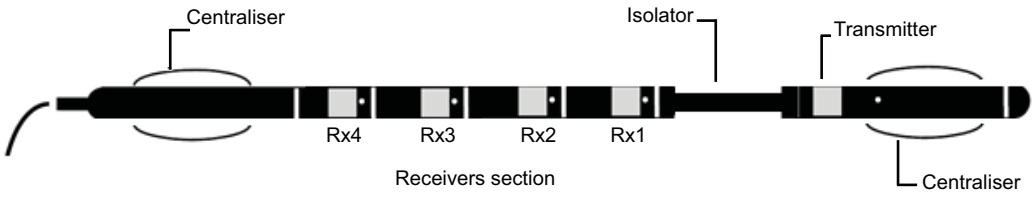

Figure 4-4. Schematic of the sonic tool elements used in this study. The first P-wave arrivals recorded at Rx1 and Rx2 were used to measure the interval velocity. The transmitter and the set of receivers were separated by 0.914 m of rubber material to attenuate the source-generated noise that travelled along the tool (Mount Sopris Instruments Inc, 2002).

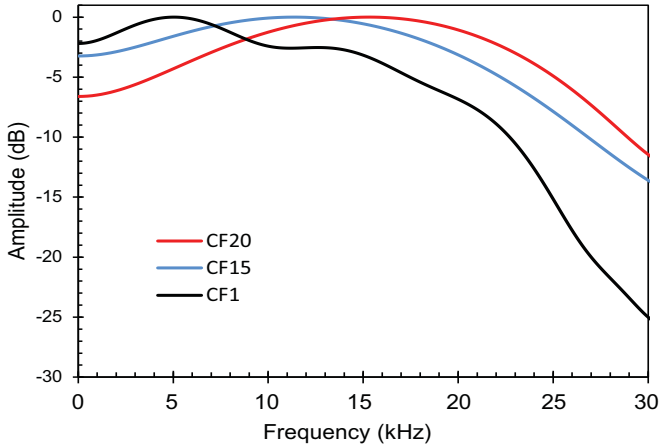

Figure 4-5. Amplitude spectrum for the full waveform sonic tool operating in a water (i.e., 5 m deep diving pool) at transmitter centre frequencies of 1, 15 and 20 kHz. Note that the maximum frequency is shifted toward the selected transmitter frequency.

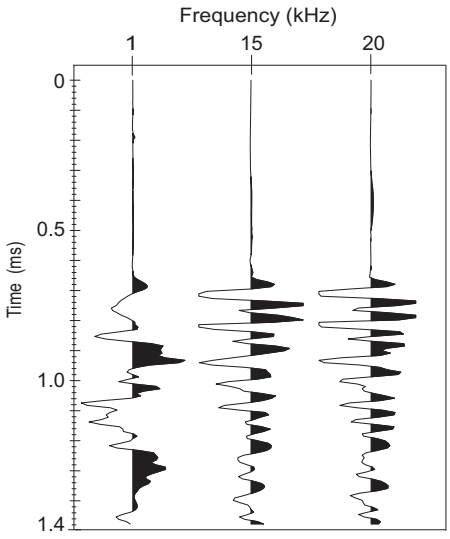

Figure 4-6. The source waveform for spectrums presented in Figure 4-5. The data are acquired at Rx1 with the source-receiver offset set to 0.9 m. Note that the shape of waveforms is highly dependent on the transmitter frequency. The P-wave arrives with a water velocity of 1534 m/s and no dispersion.

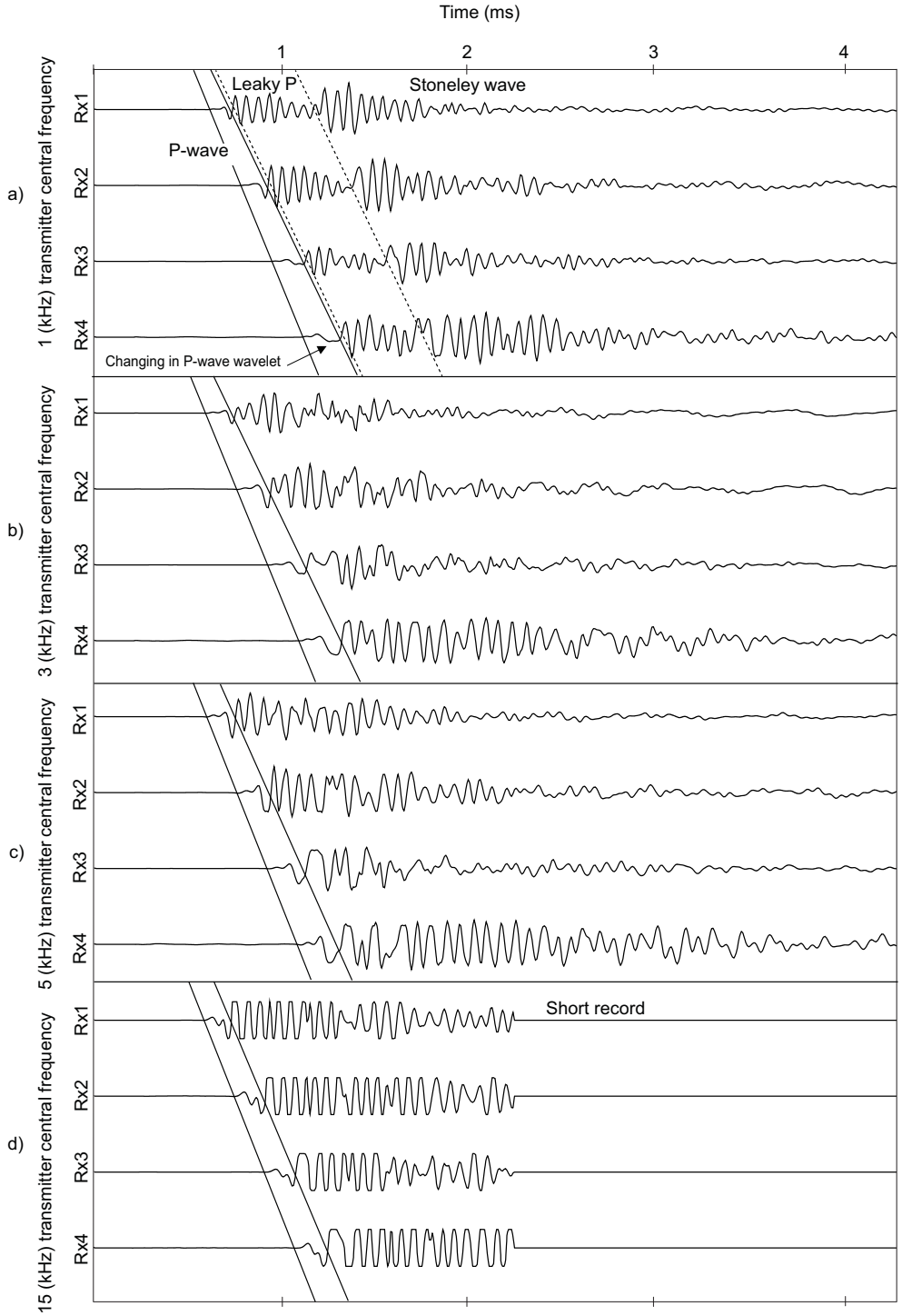

Figure 4-7. An example of FWS data sets acquired by four receivers with transmitter centre frequencies of (a) 1, (b) 3, (c) 5 and (d) 15 kHz. The solid lines indicate how the P-wave wavelet vary with distance from the source due the effect of other modes. The arrival of leaky mode seems to be overlapped with P-

wave energy at Rx3 and Rx4. The displayed FWS data was acquired at a depth of 66.7 m below ground surface.

Table 4-2. Full waveform acquisition parameters.

Logging parameter	Value
Date logged	September, 2008
Logging speed	2 m/min
Conditions of well	100 mm diameter drilled hole
Shot spacing	5 cm
Data sampling rate	4 μs
Probe diameter	39 mm
Tool mode	Monopole
Near- to far-offsets	0.9144 to 1.8288 m
Receiver spacing	0.3048 m
Transmitter central frequency	1, 3, 5 and 15 kHz
Data recording length	1, 3 and 5 kHz data sets recorded to 4.308 ms, and 15 kHz recorded to 2.24 ms
Number of transmitters	1
Number of receivers	4
Interval logged	1 kHz from 54.92 to 189.92 m 3 kHz from 55.08 to 86.98 m 5 kHz from 1.91to 86.81 m 15 kHz from 3.99 to 190.09 m

4.3.2 Apparent velocity dispersion

Apparent P-wave dispersion can be observed from the first arriving wavelet acquired with different transmitter central frequencies. The term 'apparent dispersion' has been used because, in reality, we are computing a per cent velocity difference between a signal that is dominantly high frequency (centred at 15 kHz) and one that is dominantly low frequency (centred at 1 kHz). At this stage we have not computed full dispersion curves for the complete wavetrain observed by the receivers as we are expressly concerned with the first arrival pulse. However, many examples of full dispersion images, which are dominated by leaky P and Stoneley waves, are provided in Almalki et al. (2013). The reason we don't apply such analysis here is because it is prone to contamination by a multitude of seismic wave

modes that follow closely behind the first arriving compressional wavelet, as presented in Figure 4-7.

Figure 4-8 shows the variation in the shape of the direct arrival P-wave acquired with transmitter centre frequencies of 5 and 15 kHz. These examples were collected at the same depth using receiver Rx1. The first arrival P-wave as shown in Figure 4-8(a) was acquired in non-cross-bedded sandstone with a permeability of 2.4 D at a depth of 54 m below surface level. Figure 4-8(b) shows the first arriving wavelet in cross-bedded sandstone with a permeability of 2.04 D at a depth of 86 m. The grain size in both samples varies from fine to gravel. These figures provide an example of the first arrival pulses in sandstones with similar permeability but different relative traveltimes for acquisition at 5 and 15 kHz. This difference in relative traveltime and pulse shape points towards differences in velocity dispersion for sandstone rocks with essentially the same permeability but different mesoscopic sedimentary structures. It seems likely that the variations in P-wave dispersion are associated with differences in small scale sedimentary structures.

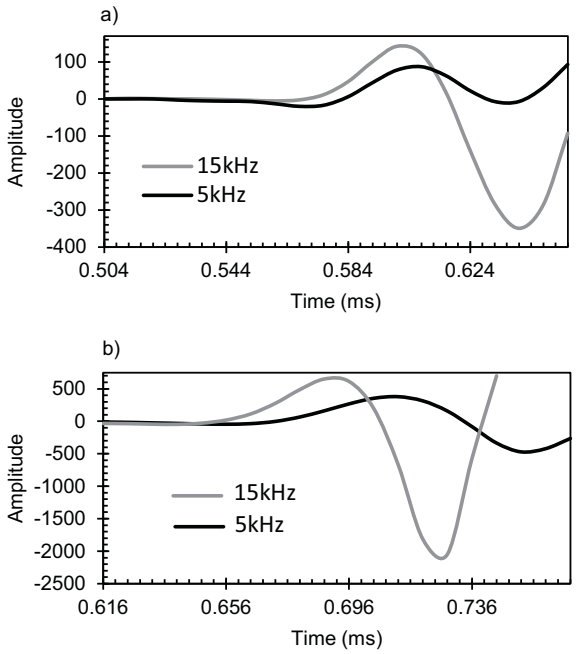

Figure 4-8. **The first arrival P-wave recorded at receiver Rx1 with the transmitter centre frequency set to 5 and 15 kHz at two sandstones sediments including (a) non-cross-bedded and (b) cross-bedded.**

4.3.3 Waveform crosscorrelation

Several processing techniques can be applied for FWS data to obtain high-quality velocity measurements (Almalki et al., 2012; Li and Mason, 2000; McCormack et al., 1993; Wu and Nyland, 1987). If the first arrival is picked by hand, the results would be qualitative. Crosscorrelation of the first arrival wavelet from receivers Rx1 and Rx2 has been conducted to provide an automatic and unbiased method of recovering the traveltime differences for data acquired with the different transmitter centre frequencies of 1 and 15 kHz. We picked top and bottom mutes to isolate the first arrival packet of seismic energy (Figure 4-9). The muting retained only the first arrival of P-waves as input for the crosscorrelation. Sheriff and Geldart (1983) explained the crosscorrelation function as a multiplication of two signals and summation of their products. If one signal is shifted with respect to the other then the crosscorrelation of the two signals will produce a maximum amplitude at a value of time τ corresponding to the delay time between the two input traces. The crosscorrelation of two signals can be given as

$$\phi_{xy}(\tau) = \sum_{k} x_k \, y_{k+\tau}, \qquad \textbf{4-7}$$

where the $\phi_{xy}(\tau)$ is the crosscorrelation of signals x_t and y_t in time domain (Sheriff and Geldart, 1983). In the frequency domain, the crosscorrelation can be considered to be the multiplication of amplitude spectra and then the subtraction of the phase spectra, as described by Sheriff and Geldart (1983), in equation 4-8 below:

$$\phi_{xy}(\nu) = |X(\nu)|\,|Y(\nu)| e^{-j[\gamma_x(\nu)-\gamma_y(\nu)]}, \qquad \textbf{4-8}$$

where $X(\nu)$ and $Y(\nu)$ are the amplited spectra, and $\gamma_x(\nu)$ and $\gamma_y(\nu)$ are phase spectra of two signals.

The maximum crosscorrelation amplitude is auto-picked to recover the traveltime differences between the two receivers, Rx1 and Rx2. Figure 4-10 shows the

crosscorrelation of the first arrival wavelets from receivers Rx1 and Rx2 using the 1 kHz data set. The red line represents lag or position of the maximum amplitude needed to recover the time differences for the velocity computations. The velocity values can be calculated by dividing the receiver pair distance (i.e., 0.3048 m) by delay time. This method was applied to determine the velocity for data sets with the dominant transmitter frequencies set to 1 and 15 kHz for the purpose of revealing small velocity differences. After recovering the velocities for both data sets, the apparent velocity dispersion (V_{disp}) is calculated by using the simple formula,

$$V_{disp} = \frac{V_{15kHz} - V_{1\,kHz}}{V_{15\,kHz}} \times 100, \qquad \textbf{4-9}$$

where V_{1kHz} and V_{15kHz} are the computed P-wave velocities from both the 1 kHz and 15 kHz transmitter centre frequency data sets, respectively.

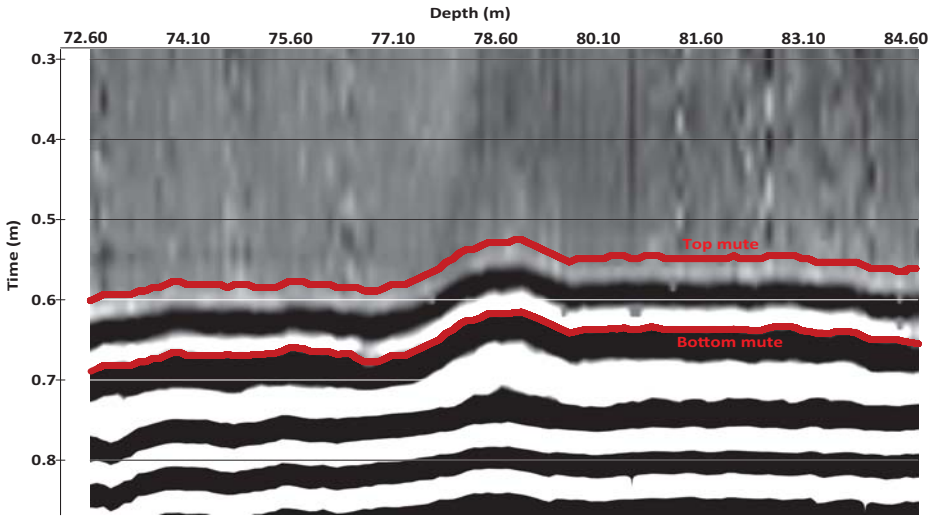

Figure 4-9. An example of picking top and bottom mute (red lines) on Rx1 to recover the P-wave direct arrivals for crosscorrelation.

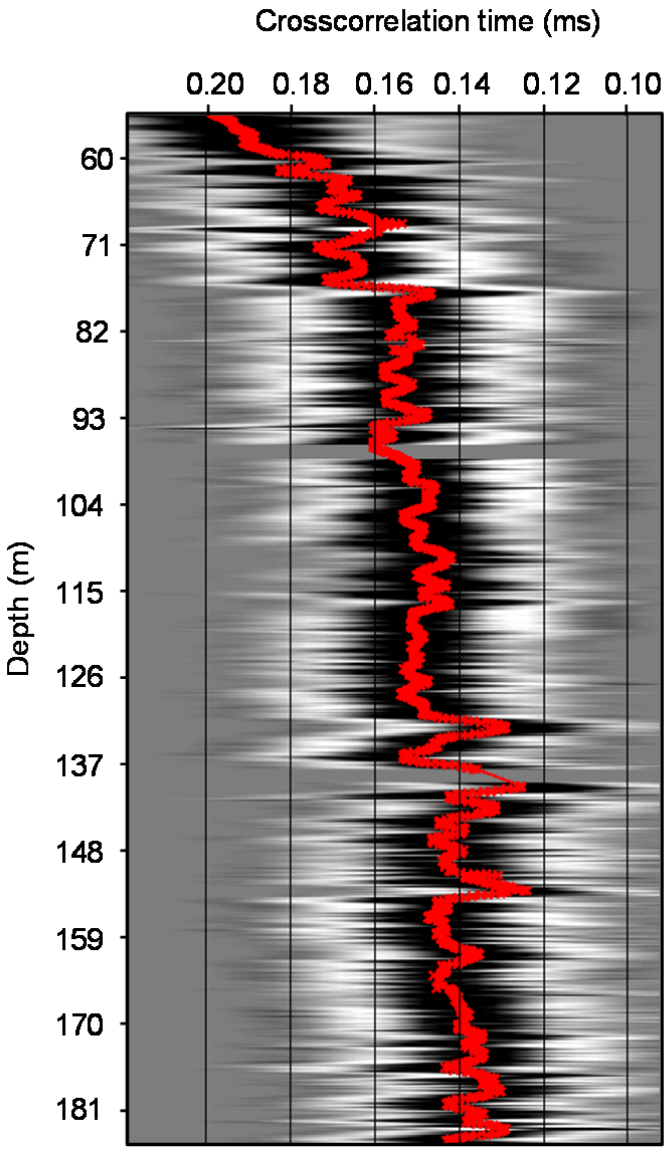

Figure 4-10. Crosscorrelation of first arrival P-waves from receivers Rx1 and Rx2 using a 1 kHz transmitter central frequency between depths of 55.32 and 187 m. The red dotted line illustrates the auto-picked traveltime differences (τ). The black zone indicates the maximum crosscorrelation amplitude.

4.3.4 Core permeability measurements

Thirty-five core samples were collected from borehole NG3 to classify the sedimentary structures. Standard 38 mm diameter plugs were recovered from these core samples to determine permeability. The experimental procedures used for

recovering permeability and a description of sedimentary structures were found in Wilson and Garcia (2009).

4.4 Results

4.4.1 Apparent P-wave velocity dispersion and formation properties

The convention employed in this work is that P-wave velocities derived from the aforementioned crosscorrelation approach are plotted at the midpoint between the receiver pairs used. The interval velocities and apparent velocity dispersions can then be associated with lithology and sedimentary structure in the interval between the receiver pairs.

Figure 4-11 shows the P-wave velocity acquired with the transmitter centre frequency set to 1 kHz (solid red track) and 15 kHz (dotted black track) in the depth range 55 to 130 m. The P-wave in the 15 kHz data set is faster over some sandstone intervals and exhibits positive dispersion. These beds, indicated by the white-blue arrows, exhibited relatively low gamma counts. While gamma is generally low in these sand-dominated beds, it shows considerable variability and tends not to be correlated in any simple or predictive way with permeability. The borehole is dominated by sandstones for which grain size and permeability can change rapidly. That is, borehole NG3 is dominated by a complex assortment of sandstones with many changes in grain size, sorting and small scale sedimentary structures (e.g., cross-bedding).

There is a 'reverse-phenomenon' where the low frequency 1 kHz data set appears faster than those for the 15 kHz data set. Note that negative dispersion implies the opposite to amplitude attenuation, which for a first arrival, is not reasonable from a rock physics perspective. So it should be stressed that negative dispersion cannot be connected with models for intrinsic dispersion as in Table 4-1. This apparent negative dispersion may however, relate to geometric dispersion. We observe that this reverse-dispersion phenomenon or apparent negative dispersion, commonly occurs across thin, high-velocity beds shown as spikes in both the 1 and 15 kHz velocity logs (examples are highlighted with black arrows in Figure 4-11). Also, this

reverse-dispersion phenomenon occurs in thin, high-velocity beds that have a carbonaceous, silt and clay matrix (see Table 4-3 and boxes in Figure 11) (Wilson and Garcia, 2009). The gamma counts for these beds (the green track in Figure 4-11) have relatively high values and the resistivity is relatively low (blue track); however, the reverse phenomenon is by no means universal for all coincident velocity and gamma "spikes". Figure 4-12 shows selected thin-section photomicrographs taken from (a) medium-fine carbonaceous interlaminated sandstone with porosity less than 10% and (b) silty micaceous fine-medium sandstone with a porosity of less than 5% (Wilson and Garcia, 2009). Generally, these samples have relatively low permeability due to the presence of clay. There are no clear explanations for the reverse -dispersion; however, we suggest that the geometry of the thin bed, given that it is a fraction of the source-receiver offset of the system, plays a role in this phenomenon. Figure 4-7 indicates the possibility of an additional low-frequency mode (leaky P) that occurs adjacent to the P-wave arrival. The low-frequency mode tends to contaminate the P-wave arrival with increasing offset. We should note that our analysis is focused on relatively thicker sandstone intervals where the sediment type could readily be characterised between receiver pairs.

The percentage velocity differences (i.e., a simple measurement of apparent velocity dispersion) between the high and low transmitter centre frequency data sets and permeability measurements in depth interval from 92 to 114.5 m are shown in Figure 4-13. In this figure we only considered the positive or normal dispersion from the thicker interval of sandstone, where velocities from the 15 kHz data set are higher than the velocities obtained from the 1 kHz data set. In this sandstone interval, the apparent dispersion is generally higher in the high permeability beds. At this stage, we do not draw a conclusion about the direct relationship between dispersion and permeability because we also know that there are many factors that could contribute to the observed velocity dispersion. However, higher permeability is weakly correlated with higher apparent dispersion.

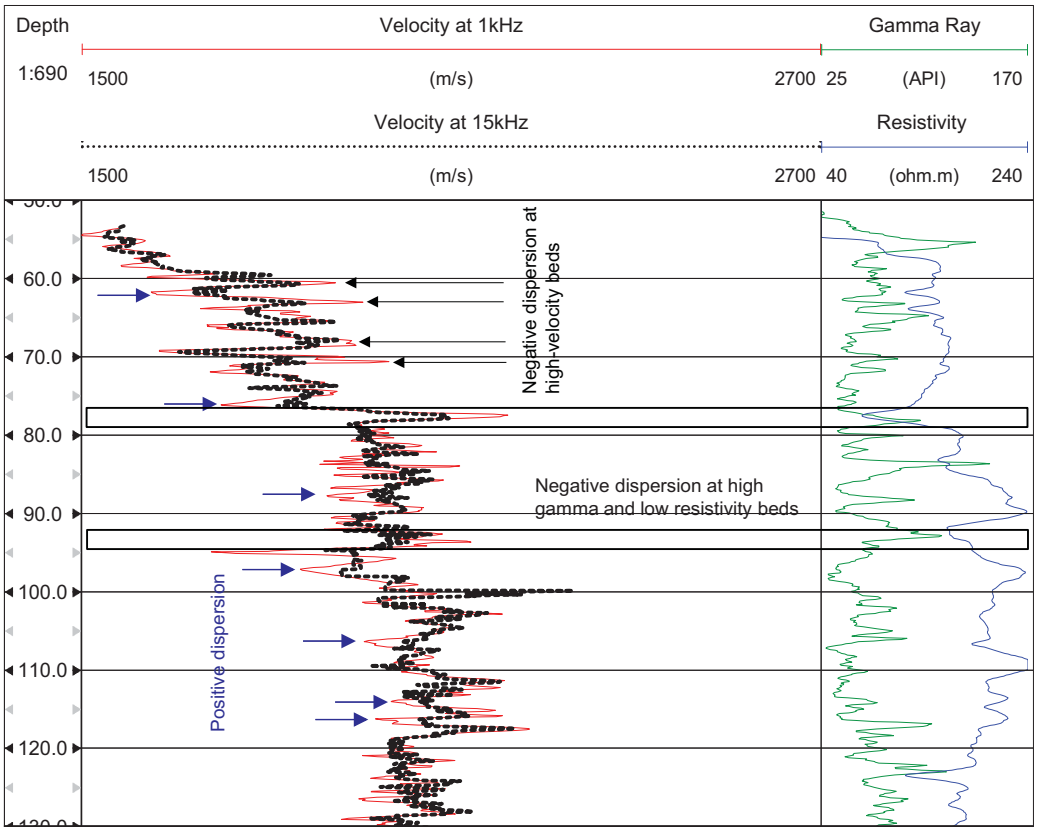

Figure 4-11. The P-wave velocity logs acquired with transmitter centre frequencies of 15 kHz (dotted black track) and 1 kHz (red track). The reverse-dispersion phenomenon occurs at (i) the high-velocity beds (black arrows) and/or (ii) the beds having high-velocity values with relatively high gamma counts and low resistivity (boxes). Examples of positive dispersion beds are indicated in blue arrows. Gamma (green track) and resistivity (blue track) logs illustrate the rapid change in aquifer properties.

a) b)

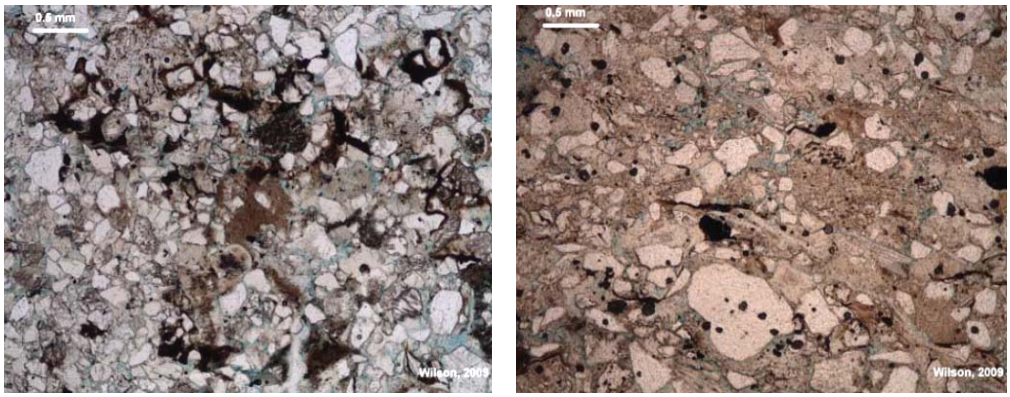

Figure 4-12. Thin section photomicrographs for (a) medium-fine carbonaceous interlaminated sandstone and (b) silty micaceous fine-medium sandstone with siltstone clasts (Wilson and Garcia, 2009). These sections are commonly identified by high gamma counts, low resistivity and high FWS velocity with reverse-dispersion phenomenon.

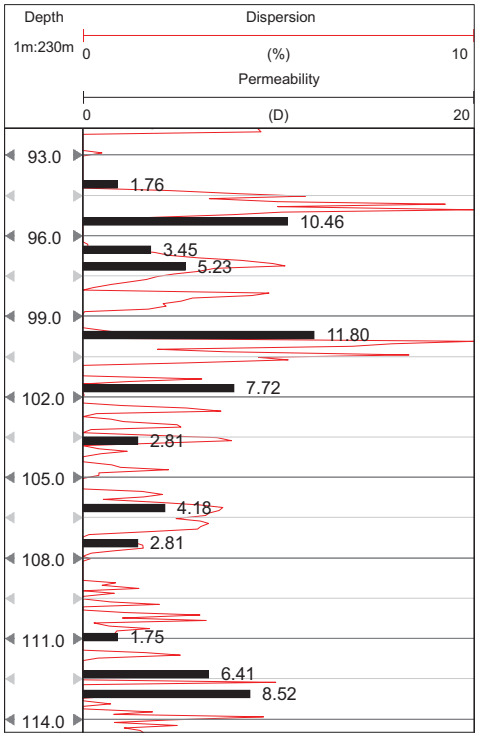

Figure 4-13. The correlation between the apparent P-wave velocity dispersion (red track) and permeability (bars). Only positive dispersion is considered. Apparent P-wave velocity dispersion roughly agrees with the measured core

permeability. Note that there is no intact core sample for a permeability measurement at a depth of 95 and 100 m where the highest velocity dispersion regions exist; however, the nearby sample is indicating an increase in permeability.

Table 4-3. An example of sediment and mineralogy of sandstone layers that have a reverse velocity dispersion (sediment structure and their component data are from Wilson and Garcia, 2009).

Sample depth	Sediment structure	Components	Gamma ray (API)	Resistivity (ohm.m)
94.10	Silty, micaceous, fine-medium (includes pebble clasts)	Quartz, feldspar, lithics clasts, siltstone, clays and mica	107.3	162
117.62	Medium-fine carbonaceous and medium-coarse interlaminated	Quartz, feldspar, mica and clay sand/silt.	102.6	191
141	Fine to very coarse to gravelly	Quartz, feldspar, lithics, and silt.	149	197
154.66	Fine to very coarse cross- bedded	Quartz, feldspar, muscov, and silt	119	125

The lithological classifications of thirty-five samples collected from borehole NG3 together with the permeability and apparent P-wave velocity dispersion measurements are listed in Table 4-4. This data set was used to investigate the characteristics of P-wave propagation in shallow sandstones having a variety of sedimentary structures. The Udden-Wentworth geometric grain size scale was used to provide grain size distribution (Wentworth, 1922). As seen in Table 4-4, the apparent dispersion of the P-wave is higher in the sandstone group where there is no observation of cross-bedded structure (i.e., non-cross-bedded) compared with the

clearly cross-bedded sandstone. These two sandstone groups show a great variety of grain size from fine to gravelly sandstones. These grain size distributions and sediment structures have combined to define the heterogeneities that may be an important factor if WIFF is to be considered as a cause of dispersion (see Table 4-1).

Table 4-4. Lithological classification of thirty-five samples from borehole NG3 (Wilson and Garcia, 2009). Two main sediment structures are observed: non-cross-bedded and cross-bedded sandstone.

Depth (m)	Permeability (D)	Apparent P-wave dispersion (%)	Sedimentary structure	Grain size
54.43	2.4	3.79	Non-cross-bedded sandstones	Medium-fine
62.16	4.04	5.38		Gravelly to medium
65.66	3.76	4.60		fine-medium with gravelly lenses (1-2cm)
66.45	5.92	3.67		Fine with gravelly lenses
82.81	2.39	3.48		Medium-fine and coarse
83.43	5.75	5.58		Medium-fine and coarse
91.79	1.92	5.15		Fine to medium
97.15	5.23	5.16		Medium to coarse
103.63	2.81	3.79		Fine to very coarse
106.14	4.18	3.57		fine to medium and coarse
129.68	2.32	2.95		Medium to coarse
165.1	6.47	4.78		Medium to coarse carbonaceous
179.91	3.32	2.55		Fine to medium
186.81	2.06	4.56		Fine
57.5	9.93	0.60	Cross-bedded sandstone	Medium-coarse
80.85	1.28	1.28		Fine
86.35	2.04	0.42		Fine to very-coarse
90.63	9.6	3.47		Coarse to very coarse

96.54	3.45	1.18		Medium-coarse
101.68	7.72	3.21		Coarse-very coarse
107.46	2.81	1.32		Fine to medium
121.19	4.63	1.90		Medium-coarse
122.62	4.64	0.36		Medium-coarse and gravelly
126.73	6.19	2.96		medium to coarse
130.29	1.95	1.26		Medium-coarse
137.97	5.11	3.54		Fine to medium
157.12	13.11	3.19		Medium to very coarse with gravelly laminae
159.64	6.23	1.51		Fine to coarse with carbonaceous
161.17	4.74	2.87		Coarse to very coarse
163.44	7.16	0.61		Medium-coarse with very coarse laminae
164.13	5.78	0.73		Medium-coarse with very coarse laminae
165.96	4.89	1.26		Medium coarse carbonaceous with very coarse laminae
169.43	9.28	2.06		Coarse to very coarse
174.52	11.22	1.36		Coarse to very
185.25	6.87	2.16		Medium coarse

4.4.2 Velocity-permeability measurements within different sediment types

We have considered possible correlations between the apparent P-wave velocity dispersion and permeability for different sedimentary structures and showed the results in Figure 4-14. Figure 4-14 shows the P-wave dispersion and permeability measurements associated with cross-bedded (grey) and non-cross-bedded (black) sandstones. The cross plots for each sediment types show increasing apparent P-

wave dispersion with increasing measured permeability as shown in Figure 4-15 and 4-16**.** Certainly the relationship within each group is somewhat complex and any correlation between apparent dispersion and permeability is relatively weak. The subset of data that represents cross-bedded sandstone illustrates low apparent dispersion between 0.4 and 3.5% for permeability values that range from 1.2 to 13 D. In contrast, the apparent dispersion values in the non-cross-bedded sandstone intervals range from 2% to 6% while permeability in the range 1.9 to 6.4 D.

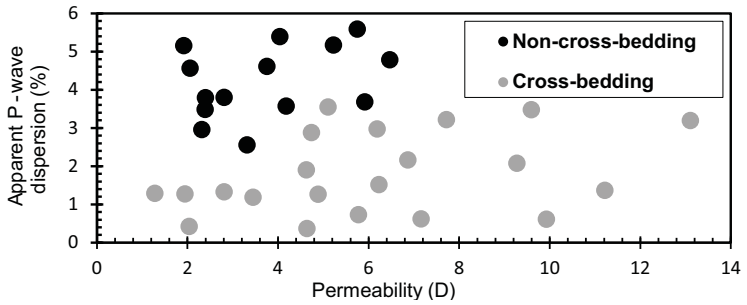

Figure 4-14. Apparent P-wave dispersion-permeability classification based on sedimentary type. The black points represent non-cross-bedded sandstone intervals, while the grey points represent cross-bedded sandstone. The cross-bedding features have higher permeability than the gravelly sandstone but with overall smaller dispersion.

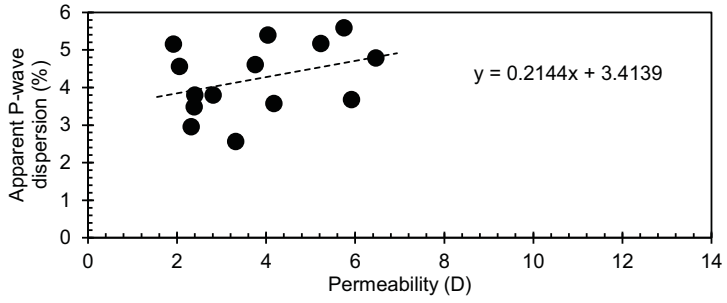

Figure 4-15. The correlation between apparent P-wave dispersion and permeability in non-cross-bedded sandstone.

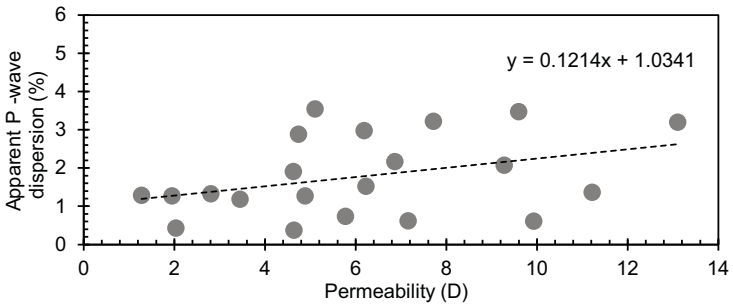

Figure 4-16. The correlation between apparent P-wave dispersion and permeability in cross-bedded sandstone.

An example of grain size distribution in the non-cross-bedded sandstone category is given in Figure 4-17. Figure 4-17 shows thin section photomicrography from different depth levels. Figure 4-17(a) shows fine to very fine sandstone with a porosity of 15% at a depth 52.15 m; 4-17(b) illustrates medium to coarse sandstone with a porosity of 25% at a depth 51.1 m; and 4-17(c) shows gravelly medium-coarse sandstone with a porosity 15% at a depth 157.12 m. Overall, the grain size varies considerably from fine to very coarse to gravelly. Wilson and Garcia (2009) suggest that although most samples contain clay in the range from 5 to 8%, the permeability values remain high. Given these observations we would suspect that the main factor controlling permeability variation is the grain size, as is often the case for shallow, weakly-consolidated sediments.

Small scale variations in sediment structure can be observed in the core samples. Figure 4-18 provides images of our two categories of sedimentary structures including (a) cross-bedded and (b) non-cross-bedded sandstone. These figures highlight the variation of small scale structures over a 30 cm interval that is approximately equivalent to the "inter-receiver" spacing over which apparent dispersion is calculated from the FWS logs. Based on the dominant transmitted frequency used (i.e., 15 kHz), we expect that the velocity information will be affected by small scale structures, as described in the work of Takeuchi and Saito (1972).

We recognise that the apparent velocity dispersion may be related to a combination of several factors as shown in Table 4-1. Having said that, we also strongly suspect that intrinsic and scattering dispersions are likely playing a dominant role. Certainly, values of phase velocity dispersion of 1 – 5% per decade

are not outside what may be expected from rock physics models, although values from 5 to 10% would be considered high.

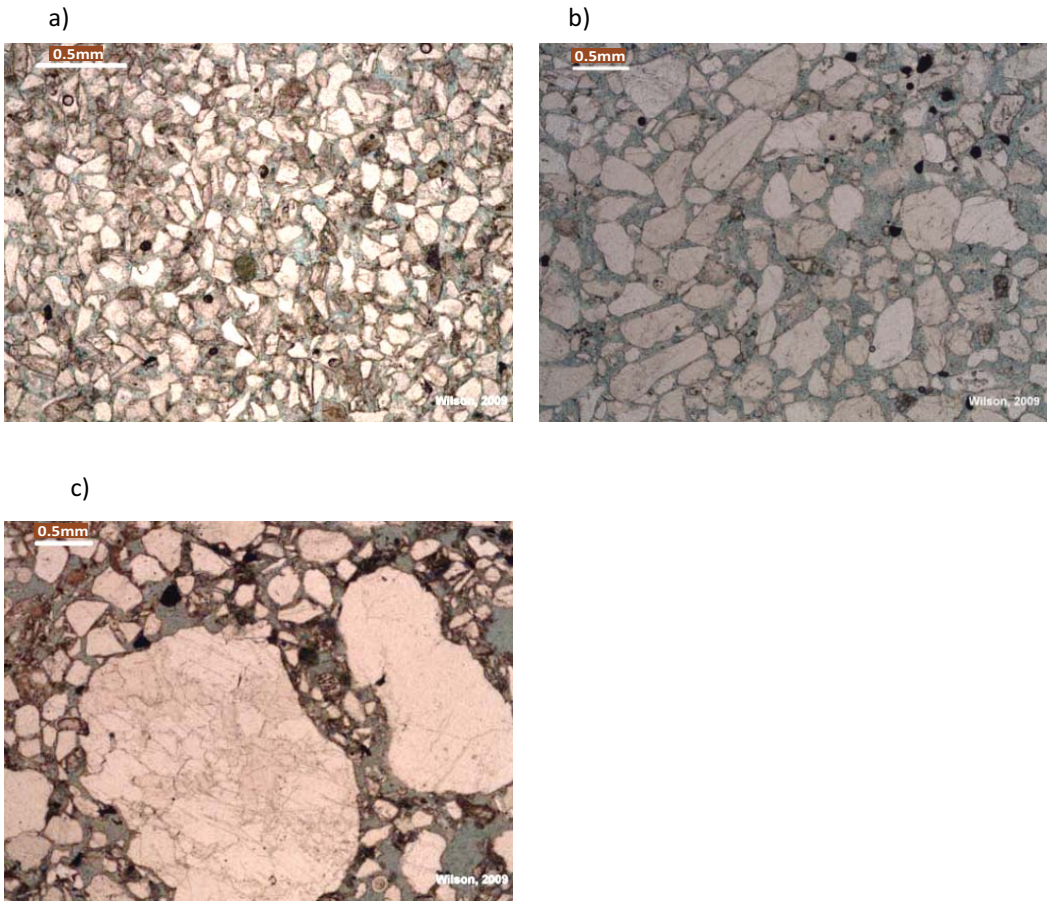

Figure 4-17. An example of thin section photomicrography shows the difference in grain size for non-cross-bedded sandstone (Wilson and Garcia, 2009). (a) Fine to very fine sandstone with a porosity of 15% at a depth of 52.15 m; (b) medium to coarse sandstone with a porosity of 25% at a depth 51.1 m; and (c) medium-coarse to gravelly sandstone with a porosity of 15% at a depth 157.12 m.

While these semi-quantitative relationships between velocity dispersion and permeability are encouraging, considerable improvement is still required in the acquisition and interpretation of multifrequency full waveform sonic data before quantitative relationships can be established. This work reinforces the fact that new

numerical and physical experimentation is required as an experimental basis for new algorithms that are needed for describing wave propagation in shallow, high-permeability sandstones, similar to those encountered in the core drill hole NG3.

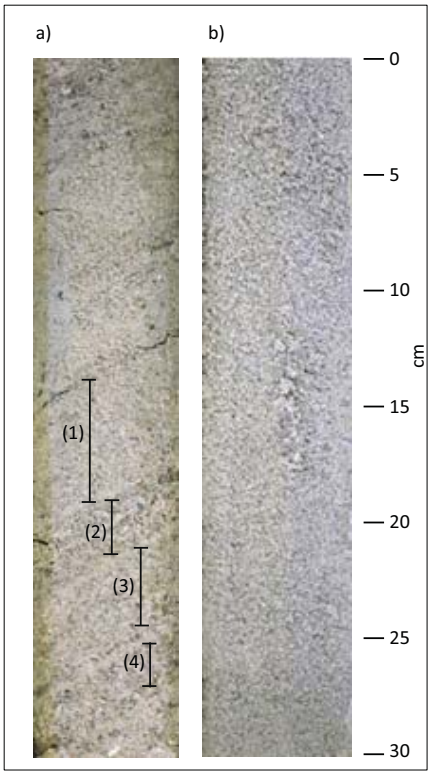

Figure 4-18. Core sample photographs taken from the NG3 cored hole for different sedimentary structures (modified from Wilson and Garcia, 2009). (a) Cross-bedded sandstone with medium to very coarse and gravelly grain size at a depth of 145.7 m (with -0.4% dispersion). The thickness of cross-bedded sandstones is varying (illustrated from 1 to 4). (b) non-cross-bedded sandstone with coarse to very coarse grain size at a depth of 171.33 m (with dispersion +0.96%).

4.5 Conclusions

Rapidly changing sediment types in shallow, weakly-consolidated sandstone formations present a highly challenging environment for FWS logging. Small

variations in the P-wave velocity with frequency have been identified from multifrequency FWS data that were acquired in a shallow, uncased cored drill hole in the Perth Basin. A positive correlation between an apparent P-wave velocity dispersion and permeability was recovered by dividing intersected sandstone dominated formation into appropriate lithological subsets. A simple processing method was developed for the multifrequency FWS data set to determine travel time measurements via crosscorrelation of first arrival wavelets. The intent of the processing method was to minimise the number of steps necessary to provide an unbiased indicator of any velocity dispersion between FWS data acquired with transmitter set to high (e.g., 15 kHz) and low (e.g., 1 kHz) centre frequencies. Sediment classification appears to be critical in understanding the relationship between dispersion and permeability. This case study indicates that velocity dispersion has potential to be a helpful tool for understanding the distribution of high-permeability intervals in weakly-consolidated sandstones. The main conclusion is that apparent P-wave velocity dispersion can vary in sedimentary rocks with similar permeabilities but different small-scale sedimentary structures. In these circumstances, classification based on sediment type is required before any empirical relationship between P-wave dispersion and permeability can be entertained. Further, considerable care must be taken to recover unbiased traveltime information for the first arriving packet of seismic energy from FWS data recorded with different transmitter centre frequencies. We must also recognize the potential contribution of geometric and scattering type P-wave velocity dispersion wherever difference in travel times (i.e. velocities) are recovered from measurements made with different transmitter centre frequencies.

4.6 References

Almalki, M., B. Harris, and J. C. Dupuis, 2012, Stoneley wave dispersion in high permeability sandstone: Perth Basin, Western Australia: ASEG Extended Abstracts, 1-4.

Ba, J., J. X. Nie, H. Cao, and H. Z. Yang, 2008a, Mesoscopic fluid flow simulation in double-porosity rocks: Geophysical Research Letters, **35,** L04303, doi:10.1029/2007GL032429.

Ba, J., H. Cao, F. C. Yao, J. X. Nie, and H. Z. Yang, 2008b, Double-porosity rock model and squirt flow in laboratory frequency band: Applied Geophysics, **5**, 261–276.

Batzle, M. L., D. H. Han, and R. Hofmann, 2006, Fluid mobility and frequency-dependent seismic velocity-Direct measurements: Geophysics, **71**, N1–N9.

Biot, M. A., 1956a, Theory of propagation of elastic waves in fluid-saturated porous solid. I. Low-frequency range: Journal of the Acoustical Society of America, **28**, 168–178.

Biot, M. A., 1956b, Theory of propagation of elastic waves in a fluid-saturated porous solid. II. Higher frequency range: Journal of the Acoustical Society of America, **28**, 179–191.

Biot, M. A., 1962, Mechanics of deformation and acoustic propagation in porous media: Journal of Applied Physics, **33**, 1482–1498.

Best, A. I., and M. S. Sams, 2003, Compressional wave velocity and attenuation at ultrasonic and sonic frequencies in near-surface sedimentary rocks: Geophysical Prospecting, **45**, 327–344.

Bourbie, T., O. Coussy, and B. Zinszner, 1987, Acoustics of porous media: Gulf Publishing Company, Technip, Paris.

Caspari, E., B. Gurevich, and T. M. Müller, 2013, Frequency-dependent effective hydraulic conductivity of strongly heterogeneous media: Physical Review E 88, 042119.

Crostella, A., 1995, An evaluation of the hydrocarbon potential of the onshore northern Perth Basin, Western Australia: Geological Survey of Western Australia, ISBN 0730944719.

David, E., and R. Zimmerman, 2013, Model for frequency-dependence of elastic Wave Velocities in porous rocks: Poromechanics, 2431-2440. doi: 0.1061/9780784412992.284.

Dutta, N., and H. Odé, 1979, Attenuation and dispersion of compressional waves in fluid-filled porous rocks with partial gas saturation (White model)-Part I: Biot theory: Geophysics, **44**, 1777-1788.

Gelinsky, S., and S. A. Shapiro, 1997, Dynamic-equivalent medium approach for thinly layered saturated sediments: Geophysical journal international, **128**, F1–F4.

Gurevich, B., and S. L. Lopatnikov, 1995, Velocity and attenuation of elastic waves in finely layered porous rocks: Geophysical journal international, **121**, 933– 947.

Gurevich, B., V. B. Zyrianov, and S. L. Lopatnikov, 1997, Seismic attenuation in finely layered porous rocks: Effects of fluid flow and scattering: Geophysics, **62**, 319-324.

Han, D. H., and A. Nur, 1987, Velocity dispersions in sandstones: 57th Annual International Meeting, SEG, Expanded Abstracts, **57**, 5–8.

Harris, B., A. Kepic, and J. C. Dupuis, 2010, Acquisition and processing report: Seismic reflection and ground penetration radar transects across the northern Gnangara Mound; Perth Basin; Western Australia: Curtin University, Department of Exploration Geophysics.

Johnston, D. H., M. Toksöz, and A. Timur, 1979, Attenuation of seismic waves in dry and saturated rocks: II. Mechanisms: Geophysics, **44**, 691–711.

Jones, T. D., 1986, Pore fluids and frequency-dependent wave propagation in rock: Geophysics, **51**, 1939-1953.

Khan, M. A., and A. I. Rees, 1967, Dispersion of seismic waves: S.K. Runcorn (Editor), International Dictionary of Geophysics, Pergamon, Oxford, **2**: 804.

Li, M., and I. Mason, 2000, Interactive seismic event recognition and its applications: Exploration Geophysics, **31**, 469-472.

Mavko, G., and D. Jizba, 1994, The relation between seismic P- And S-wave velocity dispersion in saturated rocks: Geophysics, 59, 87–92.

Mavko, G. M., and A. Nur, 1975, Melt squirt in the asthenosphere: Journal of Geophysical Research, 80, 1444-1448.

Mavko, G. M., and A. Nur, 1979, Wave attenuation in partially saturated rocks: Geophysics, 44, 161-178.

Meissner, R., 1983, Attenuation of seismic waves in sediments: Proc. 11th World Petroleum Congress, 363-379.

Mount Sopris Instrument Co., Inc., 2002, 2SAA-1000/F Sonic Probe: Colorado, USA.

Mavko, G. M., and A. Nur, 1975, Melt squirt in the asthenosphere: Journal of Geophysical Research, **80**, 1444-1448.

Mavko, G. M., and A. Nur, 1979, Wave attenuation in partially saturated rocks: Geophysics, **44**, 161-178.

McCormack, M. D., D. E. Zaucha, and D. W. Dushek, 1993, First-break refraction event picking and seismic data trace editing using neural networks: Geophysics, **58**, 67-78.

Müller, T. M., and B. Gurevich, 2005, Wave-induced fluid flow in random porous media: Attenuation and dispersion of elastic waves: Journal of the Acoustical Society of America, **117**, 2732-2741.

Müller, T. M., B. Gurevich, and S. A. Shapiro, 2008a, Attenuation of seismic waves due to wave-induced flow and scattering in random porous media, in H. Sato and M. Fehler, eds., Earth heterogeneity and scattering effects on seismic waves: Elsevier, 123-166.

Müller, T. M., B. Gurevich, and M. Lebedev, 2010, Seismic wave attenuation and dispersion resulting from wave-induced flow in porous rocks – A review: Geophysics, 75 (5), 75A147–75A164.

Murphy, W. M., K. W. Winkler, and R. L. Kleinberg, 1984, Frame modulus reduction in sedimentary rocks: The effect of adsorption on grain contacts: Geophysical Research Letters, **II**, 805-808.

Norris, A. N., 1993, Low-frequency dispersion and attenuation in partially saturated rocks: Journal of the Acoustical Society of America, **94**, 359– 370.

O'Connell, R. J., and B. Budiansky, 1977, Viscoelastic properties of fluid-saturated cracked solids: Journal of Geophysical Research, **82**, 5719-5736.

Palmer, I. D., and J. L. Traviolia, 1980, Attenuation by squirt flow in under-saturated gas sands: Geophysics, **45**, 1780-1792.

Pride, S. R., J. G. Berryman, and J. M. Harris, 2004, Seismic attenuation due to wave induced flow: Journal of Geophysical Research, **109**, no. B1, B01201.

Pride, S. R., 2005, Relations between seismic and hydrological properties, in Y. Rubin, and S. S. Hubbard, eds., Hydrogephysics: Springer, 253–290.

Pride, S. R., J. M. Harris, D. L. Johnson, A. Mateeva, K. T. Nihei, R. L. Nowackack, J. W. Rector, H. Spetzler, R. Wu, T. Yamamoto, J. G. Berryman, and M. Fehler, 2003, Permeability dependence of seismic amplitudes: The Leading Edge, **22**, 518–525.

Prasad, M., 2003, Velocity-permeability relations within hydraulic units: Geophysics, **68**, 108–117.

Rabnawaz, U., 2009, Acoustic logging for hydrogeology, Perth Basin, Western Australia: MSc(Geophysics), Report GPM 3/09, Curtin University, November 2009.

Rubino, J. G., L. B. Monachesi, T. M. Müller, L. Guarracino, and K. Holliger, n.d., Compressional seismic wave attenuation and dispersion due to wave-induced flow in porous rocks with strong permeability fluctuations: In press in Journal of the Acoustical Society of America.

Rubino, J., C. Ravazzoli, and J. Santos, 2009, Equivalent viscoelastic solids for heterogeneous fluid-saturated porous rocks: Geophysics, **74**, N1-N13.

Rubino, J., D. Velis, and K. Holliger, 2012, Permeability effects on the seismic response of gas reservoirs: Geophysical journal international, **189**, 448-468.

Pun, W., B. Milkereit, and B. Harris, 2010, Extracting frequency-dependent velocities from full waveform sonic data: SEG Technical Program Expanded Abstracts: 4024-4028, doi: 10.1190/1.3513698.

Sams, M., J. Neep, M. Worthington, and M. King, 1997, The measurement of velocity dispersion and frequency-dependent intrinsic attenuation in sedimentary rocks: Geophysics, **62**, 1456–1464.

Sato, H., M. C. Fehler, and T. Maeda, 2012, Seismic wave propagation and scattering in the heterogeneous earth: Springer, ISBN 3642230288.

Sheriff, R. E., and P. L. Geldart, 1983, Exploration seismology Vol 2: Cambridge University Press.

Takeuchi, H., and M. Saito, 1972, Seismic surface waves. In: Seismology: Surface wave and earth oscillations, Methods in computational physics: 11, B. A. Bolt, Ed. Academic Press, New York.

Vogelaar, B., 2009, Fluid effect on wave propagation in heterogeneous porous media: PhD. thesis, Delft University of Technology.

Wentworth, C. K., 1922, A scale of grade and class terms for clastic sediments: Journal of Geology, **30**, 377–392.

Western Australia Planning Commission, 2001, Gandangara land use and water management strategy: Western Australia Planning Commission, Final Report, Perth, Western Australia.

Winkler, K., 1985, Dispersion analysis of velocity and attenuation in Berea sandstone: Journal of Geophysical Research, **90**, 6793–6800.

Wilson, M. E., and M. O. Garcia, 2009, Sedimentology and aquifer quality of the Yarragadee Formation in the Perth Basin: Report for Department of Water, 120 P.

White, J. E., 1975, Computed seismic speeds and attenuation in rocks with partial gas saturation: Geophysics, **40**, 224– 232.

White, J. E., N. G. Mikhaylova, and F. M. Lyakhovitsky, 1975, Low-frequency seismic waves in fluid-saturated layered rocks: Izvestija Academy of Sciences USSR, Phys. Solid Earth, 11, 654–659.

Wu, X., and E. Nyland, 1987, Automated stratigraphic interpretation of well log data: Geophysics, **52**, 1665-1676.

Zimmer, M. A., 2004, Seismic velocities in unconsolidated sands: Measurements of pressure, sorting, and compaction effects. Ph.D. thesis: Stanford University.

CHAPTER 5 : Field and Synthetic Experiments for Virtual Source Crosswell Tomography in Vertical Wells, Perth Basin, Western Australia[3]

This chapter presents the potential of virtual source crosswell tomography in two vertical wells. The research has been published in the *Journal of Applied Geophysics*.

3. Almalki, M., Harris, B. and Dupuis, C.J. 2013. Field and synthetic experiments for virtual source crosswell tomogrphy: Journal of Applied Geophysics, **98**, 144-159.

5.1 Summary

It is common for at least one monitoring well to be located proximally to a production well. This presents the possibility of applying crosswell technologies to resolve a range of earth properties between the wells. We present both field and synthetic examples of dual well walkaway vertical seismic profiling in vertical wells and show how the direct arrivals from a virtual source may be used to create velocity images between the wells. The synthetic experiments highlight the potential of virtual source crosswell tomography where large numbers of closely spaced receivers can be deployed in multiple wells. The field experiment is completed in two monitoring wells at an aquifer storage and recovery site near Perth, Western Australia. For this site, the crosswell velocity distribution recovered from inversion of travel times between in-hole virtual sources and receivers is highly consistent with what is expected from sonic logging and detailed zero-offset vertical seismic profiling. When compared to conventional walkaway vertical seismic profiling, the only additional effort required to complete dual well walkaway vertical seismic profiling is the deployment of seismic sensors in the second well. The significant advantage of virtual source crosswell tomography is realised where strong near surface heterogeneity results in large travel time statics.

5.2 Introduction

A cost-effective and low-impact method for recovering velocity information between verticals wells is likely to be of considerable interest for the groundwater, geothermal, geotechnical and conventional/unconventional hydrocarbon industries. For any site where large volumes of fluids are injected into or pumped from the subsurface, crosswell tomography may provide a useful constraint on the distribution of the mechanical and hydraulic properties. Here, the term “tomography” refers to a technique that uses direct travel times between in-hole sources to receivers to reconstruct the velocity distribution between two wells.

Developing a hydrostratigraphic model between wells is often based on interpolation between wire-line logs. However such interpolation can and should be enhanced by crosswell methods where they can be applied at reasonable cost. In

subsurface storage for fluids, such as what occurs during aquifer storage and recovery (ASR), it is often important to track the fate of the injectant. ASR operations are often intended to inject water when it is abundant and to retrieve water when it is in short supply or high demand. For arid to semi-arid climates such as that of Perth, Western Australia, aquifer management may mean banking (i.e., injection) in the winter and the retrieval of stored water in hot summer periods. The water chemistry and clogging potential in different sediment layers depends on geochemical interactions between the injected water and formation sediments (Descourvières et al., 2010) and on the discharge rate from the well (Lowry and Anderson, 2006). It is our intent to test the potential of a method of recovering crosswell velocity distribution that may assist in constraining the geometry of subsurface models required for hydraulic or reactive transport modelling.

A number of techniques can be used to recover a crosswell velocity distribution without using downhole sources. Blakeslee and Chen (1996) investigated a method that can be used to simulate crosswell tomography using seismic sources on the surface. The travel times are measured at receivers deployed in both wells and compared to the travel time calculated on the basis of an assumed inter-well velocity model. This method is akin to crosswell tomographic inversion based on vertical seismic profiling (VSP), which modifies an initial velocity model based on the travel time measurement between receivers in closely spaced wells. Zhou (2006) used the first arrivals from VSP, in which receivers are deployed in a single vertical borehole and a number of seismic sources are distributed on the surface to construct a three-dimensional (3D) velocity-depth model for a salt dome structure using a tomographic approach described as deformable-layer tomography (DLT). This method is suitable for areas where geological and geophysical information is known for model parameterisation. That is, the velocity information for some regions on the 3D model must be supplied for the inversion process to stabilise the solution. However, the limitation of these methods is the requirement of an accurate travel time and a priori knowledge of velocity structure. We address this particular problem by using a method based on seismic interferometry (Wapenaar et al., 2010).

The advantage of direct-wave seismic interferometry using a controlled/active source is an important application for this research. Seismic interferometry creates pseudo-seismic recorders by cross-correlating wavefields received at two different

positions without known model parameters (Wapenaar et al., 2006, 2010). As a historical side note, the idea of seismic interferometry was originally put forward by Claerbout (1968), who stated that the autocorrelation of a wavefield from a source buried in horizontally layered media is a response from an impulsive source on the surface. Using source-receiver reciprocity, Bakulin and Calvert (2006) developed an approach to redatum surface sources into deviated borehole by cross-correlating the wavefield recorded in two receiver positions. This technique is called the "virtual source method" (VSM). For imaging proposes, Bakulin and Calvert (2006) suggest that a preferable application of a virtual source experiment is in deviated or curved 3D trajectory wells. The algorithm of the VSM can be written as

$$D_{\alpha\beta}(t) = \sum_{k=1}^{N} S_{k\alpha}(-t) * S_{k\beta}(t), \qquad \textbf{5-1}$$

where

$D_{\alpha\beta}(t)$ is equivalent to the response at a selected downhole virtual source (α), measured by any downhole receiver (β),

$S_{k\beta}(t)$ is the response recorded by the receiver (β), from the kth source at the surface,

$S_{k\alpha}(-t)$ is the time-reversed portion of the response recorded by (α) from the kth source at the surface, and

N is the source element, and '$*$' denotes temporal convolution.

The application of time-reversed acoustics can be implemented for tomographic inversion to construct the velocity information between two receivers. Zhou and Schuster (2000) provided an alternative approach called the Phase-Closure principle, which integrates the concept of seismic interferometry directly into the tomographic inversion process. For their work both sources and receivers are inside the boreholes. Torii et al. (2006) conducted a small-scale laboratory based VSM experiment. While the authors retrieved the direct wave, they did not proceed in the analysis of the tomographic inversion. Also their experiment was not intended to represent or

analyse the complexities and heterogeneity that exist in the full scale field experiments we present.

Vasconcelos and Snieder (2008) presented a new approach for processing based on seismic interferometry of passive data using multidimensional deconvolution (MDD). In essence, the computation of this method required a receiver's array coverage in which all receivers simultaneously contributed to matrix inversion regularisation. The application of MDD was then modified by Minato et al. (2011), who could stabilise the MDD solution using a singular-value decomposition (SVD) approach. This method is intended to better retrieve down-going and up-going wavefield amplitudes compared to the crosscorrelation VSM (Bakulin and Calvert 2006).

Minato et al. (2013) used the SVD approach for borehole configurations to evaluate the quality of the wavefield retrieved by MDD interferometry. Their experiment examined the effect of data redundancy due to the surface source distribution. In localised surface source positions (i.e., sources are only in one side of the boreholes), the MDD method retrieved the first arrival amplitude, and the result further improved when including near-surface scatterers. While many published works discuss the possibility of virtual source tomography, none analyse the field application of the method or how well tomographic inversion can recover velocity distribution.

In this paper we explore methods for recovering the velocity distribution between two vertical wells that do not require actual in-hole seismic sources to be deployed. Our approach combines the recovery of accurate crosswell travel times with the VSM (Bakulin and Calvert, 2006) and tomographic inversion. We refer to our approach as "virtual source crosswell tomography" (VSCT). We require only a line of surface sources and the first arriving wavelet as recorded at in-hole receivers in two vertical wells. We do not require or create full virtual source records for our VSCT approach.

Synthetic modelling of seismic records is used to assess the field parameters and processing requirements for the application of VSCT. The method we develop is then applied to dual well walkaway vertical seismic profiling (WVSP) field data acquired in two monitoring wells at the Mirrabooka Aquifer Storage and Recovery (ASR) trial

site in Perth, Western Australia. In addition to testing VSCT for vertical wells, a site-specific objective is to better characterise aquifers above and within the ASR trial injection zone by investigating the P-wave velocity's structure between two wells.

5.3 Method

5.3.1 Generating the virtual source

The virtual source method can be used to simulate a set of sources below complex overburden to achieve improved subsurface images. For vertical wells, this method requires simultaneous acquisition using surface sources and receivers located in two wells, as shown in Figure 5-1. To generate a virtual source at R_α, we crosscorrelate the wavefield from each surface source recorded by the receiver R_α in the first borehole with the wavefield recorded by the receiver R_β. Next, the crosscorrelated traces are summed over the surface sources. This idea is the general principle of the VSM presented in equation 5-1 (Bakulin and Calvert, 2006). Note that, for our virtual source crosswell tomography we isolated the first arrival information from the dual well WVSP by applying time muting to remove other wavefields. Wavefield separation in crosscorrelation seismic interferometry is commonly used for improving the reflection response (van der Neut and Bakulin, 2008; Mehta et al., 2007)

The surface source distribution is an important factor in creating a virtual source (Minato et al., 2013). For a given receiver pair, one can get a kinematically correct wavefield if (i) surface sources are in the stationary phase region only, or (ii) surface sources of equal strength are distributed around the virtual source or receiver pair (Vasconcelos and Snieder, 2008; Wapenaar et al., 2010).

A key step in retrieving the direct arrival from the VSM is fulfilling the stationary phase condition (Wapenaar et. al., 2010). Figure 5-2 presents the crosscorrelation of three receiver pair configurations Rx1-Rx2, Rx1-Rx3 and Rx1-Rx4 shown in Figure 5-1. To assess the stationary phase conditions for well pairs, we crosscorrelate a synthetic direct wave obtained at each receiver pair and accumulate the contribution of each source to build the travel time curve of the crosscorrelation as shown in

Figure 5-2a, 5-2c, and 5-2e. The velocity model for this synthetic example is shown in Figure **5-1**. Further detailed description of the model is provided in section 5-4. The stationary phase contribution is achieved at source regions that attain a maximum in the travel time curve of the correlated traces (Figure 5-2a, 5-2c, and 5-2e). Summing the correlated traces (Figure 5-2b, 5-2d, and 5-2f) generates a new trace corresponding to the signal that would be recorded at receivers Rx2, Rx3 and Rx4 as if there was a source excitation at receiver position Rx1. The VS trace is provided next to the crosscorrelation panels in Figure 5-2b, 5-2d, and 5-2f. The peak of the VS trace is automatically picked using a computer-based method to find the delay time associated with the travel distance between the receiver pair. The picking method refers to as the stabilized power ratio algorithm implemented in ProMAX package (Landmark Graphics, 1995). The algorithm calculates the energy within user defined windows and search for the spike of energy that indicates the first arrival.

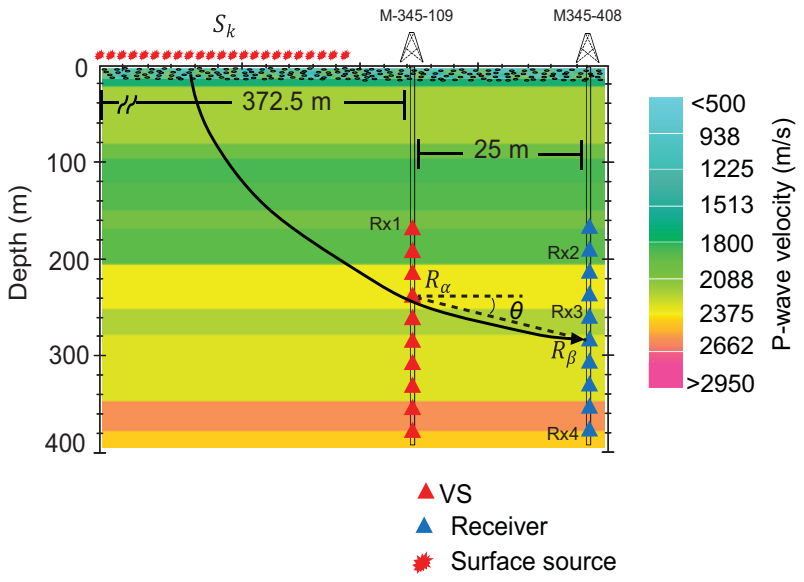

Figure 5-1. **Acquisition geometry for virtual source cross well tomography in vertical wells. The receiver R_α in well-109 is converted to a virtual source. The angle theta is the take-off angle of the ray defined between the horizontal plane and a line connecting the virtual source position at R_α and the receiver R_β.**

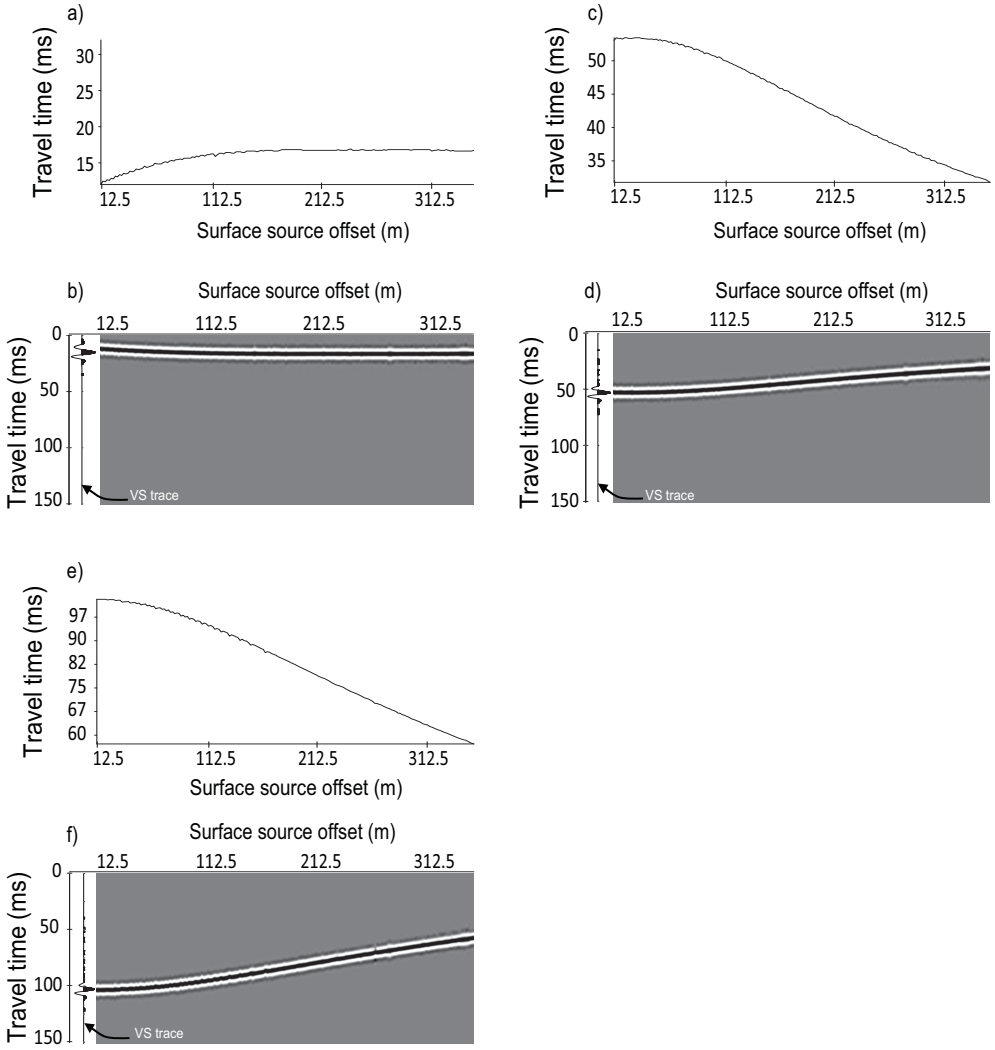

Figure 5-2. Illustration for the stationary phase region for three receiver pairs on the crosscorrelation travel time curve. Panels (a, b) show respectively the travel time curve and the crosscorrelation gather for receiver pair Rx1 and Rx2 (see Figure 5-1). The take-off angle θ for this receiver pair is approximately 38°. Similarly, panels (c, d) present the case for receiver pair Rx1 and Rx3 with take-off angle equal to 77°, and panels (e, f) for receiver pair Rx1 and Rx4 at take-off angle equal to 83° . The Rx1 is assumed to be a virtual source at a depth of 170 m in well-109 and Rx2, Rx3, and Rx4 are the receivers in Well-408 at depths 190, 280, and 400 m, respectively. The product after stacking the crosscorrelation gather is the VS trace that shows the maximum peak corresponds to the travel time associated to the travel distance between each receiver pair. Note that the amplitude of correlated traces decreases as the distance from the receiver increases.

5.3.2 Tomographic inversion

Tomographic inversion was completed with the simultaneous iterative reconstruction technique (SIRT) contained in the ReflexW software (Sandmeier, 2011). Detailed descriptions of the SIRT were provided by many authors (Ivansson, 1983; Van der Sluis and Van der Vorst, 1987; Granet and Trampert, 1989; Humphreys and Clayton, 1988). Straight and curved ray assumptions are applied in the synthetic VSCT experiments so that a comparison can be made. For application of VSCT to field data, only curved-ray tomography is used. The following describes key parameters used during travel time inversion.

The inversion process commences with setting an initial homogeneous half-space model to a constant P-wave velocity of 2000 m/s. The area between the two vertical wells is discretised to have a 0.5 m by 0.5 m grid cell size. A total of 8100 cells are used for the inversion. The same initial model is used for all tomographic inversions presented.

During the tomographic inversion, model travel times are computed and subtracted from the observed travel times. These travel time residuals are inverted for velocity changes along the raypaths. The process is iterated until a satisfactory fit is achieved. The fit is based on the standard deviation (i.e., data variance) of the travel time residuals. The residuals for each ray Δt_k^n are calculated as the square of the differences between observed (t_k) and computed (t_k^n) travel times divided by the data variance $V_n$as

$$\Delta\, t_k^n = \frac{\left(t_k^n - t_k\right)^2}{V_n}, \qquad \textbf{5-2}$$

where n and k are the iteration and ray number respectively. Data variance is given as (Peterson et al., 1985),

$$V_n = \frac{1}{I}\sum_{i=1}^{I} (S_i^n - \bar{S})^2, \qquad \textbf{5-3}$$

where $\bar{S}$ is the mean slowness value of the field, I is the total number of pixels intersected by the ray k and S_i^n is the slowness of pixel i after the nth iteration. The variance is an indicator for the quality of the observed travel times. If the variance is

high then the quality of travel time is low. Therefore the individual residuals will be decreased with increased given data variance because of the high uncertainty of the observed data (Sandmeier, 2011).

The effect of ray coverage in VSCT is explored by changing the number of simulated virtual sources and receivers in the synthetic model. For the VSCT applied with geometry shown in Figure 5-3 all rays must be down-going and have take-off angles between 20° to 80°. Ideally, the receivers in the virtual source borehole should extend to the surface to achieve the maximum range of take-off angles and ray coverage. That is, it's preferable for receivers in the virtual source borehole to go to the surface and receivers in the receiver borehole to extend to the maximum depth possible. A further improvement might be achieved by extending the line of WVSP sources out on both sides of the well pair (Minato et al., 2013).

We found that smoothing in the x- and z-directions within a window size of 4 by 4 m allows the inversion to achieve satisfactory data fitting. The inversion parameters (i.e., initial model, cell size, number of iterations, and smoothing parameters) were kept constant for all tomographic inversions present in this work.

5.4 Synthetic modelling

Synthetic shot records are computed with the comprehensively tested finite difference software, Tesseral-2D (Kostyukevych and Roganov, 2010; Kostyukevych et al., 2009). Two synthetic models are generated based on the approximate velocity distribution recovered from the wells at the Mirrabooka ASR study site (Harris et al., 2010). The surface source and in-hole receiver geometry for the synthetic models are shown in Figure 5-3a and 5-3b.

The first model consists of 14 coarse horizontal layers spanning the interval from the surface to 400 m below the surface level (Figure 5-3a). The compressional wave velocities are based on the dense zero-offset vertical seismic profiling (ZVSP) field data completed at the ASR site in the monitoring well M345-109. The ZVSP surveys were completed in such a way that data could be recovered at 0.5 m receiver intervals over the depth range from 160 to 400 m. A string of 24 hydrophones was

deployed twenty times with a shot record being recovered at 0.5 m intervals. For the depth range from 50 to 160 m, the velocity model is based on full waveform sonic (FWS) logging velocities (Harris et al., 2010). Figure 5-4 compares the velocity obtained from the dense ZVSP (black points) and FWS logging (red track) at the well M345-109. The average velocities from the ZVSP and FWS logging are used to create the coarse-layer synthetic model as shown by the grey track in Figure 5-4.

In Figure 5-4 there is some discrepancy between ZVSP and FWS velocities over interval from depths of 300 to 340 m. This may be associated with fine layering of claystone, siltstone, and sandstone (Almalki et al., 2012a). The dense ZVSP data has spectral energy centred at approximately 90 Hz, and the FWS data have spectral energy that is centred at closer to 15 kHz. The difference in the dominant acquisition frequency for these two data sets is approximately two orders of magnitude and differences in the velocities are to be expected. However, on the whole the ZVSP and the FWS velocities agree well with the difference rarely more than 4%. Together, the ZVSP and FWS data provide a detailed consistent and accurate representation of the vertical P-wave velocity for this horizontally layered formation at the study site. We emphasise that the travel time measured for both methods (ZVSP and FWS) is from the first arriving P-wave propagating vertically between receivers. Note that the surface source offset in the dense ZVSP experiment is 12.5 m from well-109. This means that if we know that the layers are horizontal and the VSCT provides an accurate estimate of the velocity between the wells, then by combining both ZVSP with VSCT experiments one could put a plausible qualitative constraint on some of the parameters needed to recover anisotropy at the study site.

We created a second detailed synthetic model with the aid of the velocity distribution obtained from the FWS logging (Figure 5-3b). This model is assigned 17 sedimentary layers, with a different P-wave velocity based on FWS measurements within the depth range from 170 to 400 m as shown in Tables 5-1 and 5-2. Note that the depth range from 170 to 400 m is selected because it spanned the critical and highly heterogeneous seal and production zone at the Mirrabooka ASR site. The reason for creating both models was to assess the ability of VSCT to recover thin layers. The formation boundaries such as Superficial, Osborne and Leederville are interpreted from Descourvières et al. (2010).

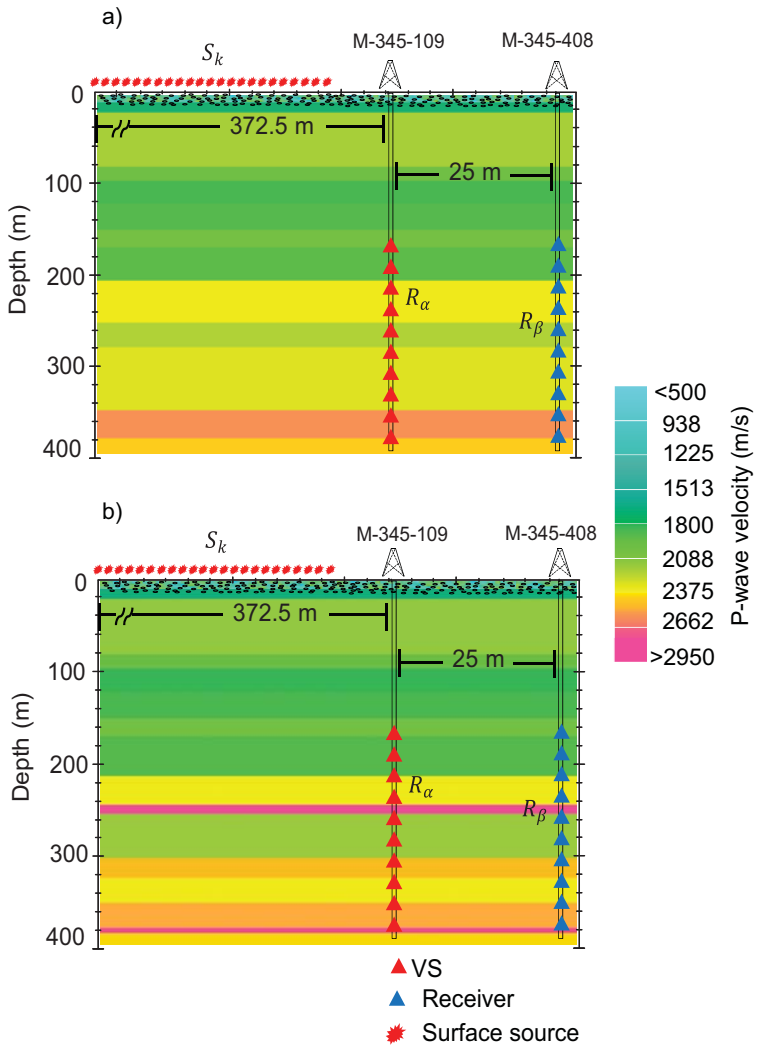

Figure 5-3. Synthetic velocity models based on ZVSP and FWS logging at the study site. (a, b) The thin and thick layer models used in our experiments, respectively. The site and model contain two vertical boreholes separated by 25 m. The synthetic experiments use line of 180 sources spaced at 2 m intervals. Data was recorded simultaneously by receivers in the wells M345-109 and M345-408.

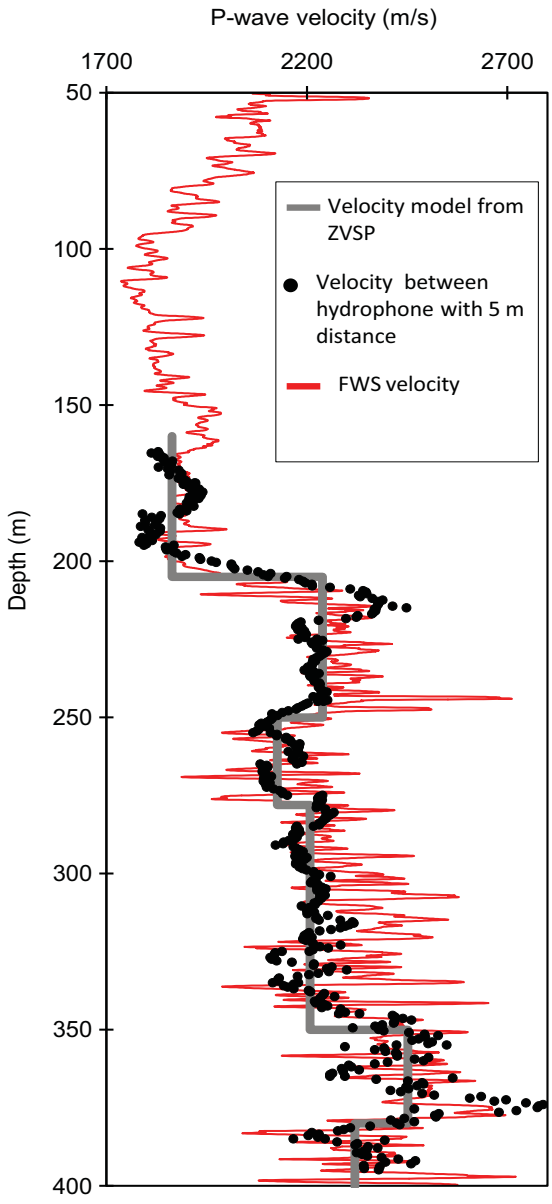

Figure 5-4. Field ZVSP- and FWS-derived P-wave velocities at the monitoring well M345-109. The black points are velocities calculated from the dense ZVSP survey with a 0.5 m spacing. The red track is the FWS-derived velocities acquired every 0.05 m with a transmitter centre frequency of 15 kHz. The ZVSP velocity is used to create a coarse-layer synthetic model, which is shown as the grey track. The ZVSP velocity is well correlated with the FWS measurements. In the depth range from 300 to 340 m the difference is on average 4%, and this difference may be associated with the heterogeneity of the sediment layering and/or the difference in the scale of penetration depth with frequency.

Table 5-1. The velocity model recovered from the ZVSP and FWS experiments at the field site. These velocities are used for the coarse layered synthetic model. Note that the shallow part of the model is similar to the thin-layer model presented in Table 5-2 (i.e. from 0 to 167.5 mbgl). The upper 6.5 m thick 500 m/sec layer is filled with small scattering polygons.

Layer depth (m)	Formation	Member	Vp (m/s)
0-6.5	Superficial		500*
6.5-20			1650
20-55			2100
55-80	Osborne	Mirrabooka	2100
80-95			1900
95-120			1800
120-150			1840
150-167.5			1960
167.5-205		Kardinya shale	1860
205-251	Leederville	Pinjar	2239
251-278		Wanneroo	2126
278-350			2208
350-380			2452
380-400			2320

Table 5-2. Thin-layer velocity model based on FWS measurements in the borehole M345-109. This model is used to test the ability of VSCT to resolve thin layers. The upper 6.5m contains small scattering polygons as described in Table 5-1.

Layer depth (m)	Formation	Member	Vp (m/s)
0-6.5	Superficial		500*
6.5-20			1650
20-55			2100
55-80	Osborne	Mirrabooka	2100
80-95			1900
95-120			1800
120-150			1840
150-167.5			1960
167.5-212.5		Kardinya Shale	1860
212.5-242.5	Leederville	Pinjar	2320
242.5-251			2870
251-300		Wanneroo	2120
300-322.50			2420
322.5-350			2300
350-375			2460
375-382.5			2800
382.5-400			2360

The synthetic dual well WVSP experiments were assigned acquisition parameters similar to the field dual well WVSP experiment completed in monitoring wells M345-109 and M345-408 at the study site. The surface source line consists of 180 shot positions with shot points 2 m apart. The source line was 372.5 m long and the first shot was located at a 12.5 m offset from the well M345-109. Source points were closely spaced to prevent spatial aliasing (Mehta et al., 2008). As shown in Figure 5-3a and 5-3b, the surface source line is located to the left of the boreholes such that the well M345-109 will contain the virtual sources. The synthetic source wavelet and other parameters for the synthetic model are presented in Figure 5-5 and Table 5-3. For the synthetic survey both wells are assigned in-hole receivers spaced at 2.5 m between depths of 170 and 400 m below the ground level. The receiver spacing was subsequently down sampled to 5 m and 10 m to assess the impact of ray coverage on the ability of VSCT to recover accurate crosswell P-wave velocity distribution.

For computation of the synthetic dual well WVSP survey a small grid cell size of 0.204 by 0.145 m is selected. This small grid cell size is needed for: (i) accurate computation of seismic wavefield propagation through the complex near-surface region, (ii) ensuring that the thin layers are suitably discretised, (iii) accommodating a maximum central source frequency on the order of 150 Hz in regions with P-wave velocity as low as 500 m/s. Note that the spectral energy of the signal recorded by hydrophones at the field study site extended above 150 Hz to a value closer to 200 Hz before tailing off into noise (see Figure 5-19). Again we would emphasise that a fine grid is necessary for accurate numerical simulation of the WVSP data.

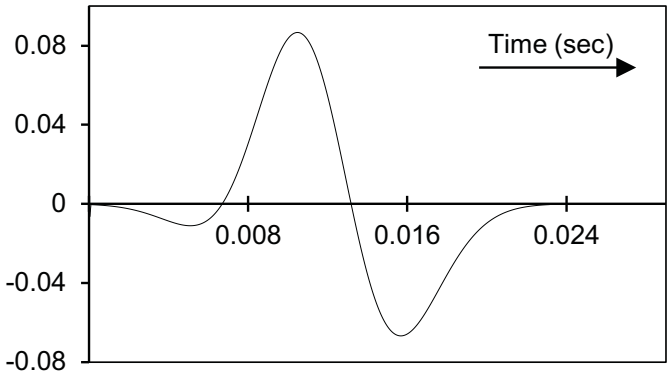

Figure 5-5. **Source wavelet used in the synthetic experiments.**

Table 5-3. The synthetic model parameters.

Model discretization	Grid points (x)	550
	Grid points (y)	450
	grid spacing in m (x)	0.204
	grid spacing in m (y)	0.145
	Grid point numbers	2696 x 3103 = 8.3 x 10^7
Geometry	Number of Sources	180
	Source spacing in (m)	2
	Total Number of Receivers	186
	Receiver spacing in (m)	2.5
	Number of boreholes	2
Source parameter	Type	Wavelet shown in Figure 5-5
	Peak frequency	150
Recording parameters	sample interval	0.25 ms
	Record length	0.5 sec
	Wave equation calculation	FD calculations using velocity and stress in a discrete grid implemented in Tesseral-2D software.

A key part of the synthetic model is inclusion of shallow scattering points within the top 6.5 m. The scattering points were polygons with size distributed from 2 to 4 m in x- and z-directions. Velocities assigned to polygons ranged from 100 to 800 m/s. These are included to simulate effects of a heterogeneous near surface zone as

shown in Figure 5-3a and 5-3b. This heterogeneity in the near-surface represents the velocity distribution in the low-velocity vadose zone at the M345 test site. This zone is highly variable and contains a patchy water-retentive "coffee-rock" (i.e., variably cemented concretionary rocks) within and just below the vadose zone (Strobach et al., 2010). Shallow highly variable layers such as coffee rock are often the result of post deposition processes spatially linked to ancient paleosols (Kraus, 1999), and/or water tables. They may also relate to dissolution of calcium carbonate material during weathering processes or old lake deposits (Strobach, 2013). A photograph of the first few metres of soil profile below the study site is illustrated in Figure 5-6. The subsoil profile in Figure 5-6 contains four horizons; A, B, C and D. Horizon A represents soft leached sand containing organic materials including growing roots, ash, and coal. Horizons B and C are unconsolidated sand with a range of sedimentation patterns. Horizon D is cemented, iron stained, indurated sands often referred to as coffee rock. The seismic velocity of this section varies from 100 m/s to 800 m/s (Almalki et al., 2012b). Figure 5-7 shows the travel time error associated with the complex heterogeneous near-surface layer at the study site. We compute these static values by searching for RMS velocities that fit the travel time curve of WVSP assuming flat subsurface layers. Large near surface statics are not uncommon in seismic data.

In order to bring synthetic VSP data to the same signal/noise level as it is observed in the field data we introduce ~5% of the random band-limited noise (with the amplitude spectra matched to the emitted wavelet) to the synthetic seismograms. Figure 5-8 provides an example of a synthetic common-receiver gather for a receiver located at a depth of 170 m below ground level in well-408.

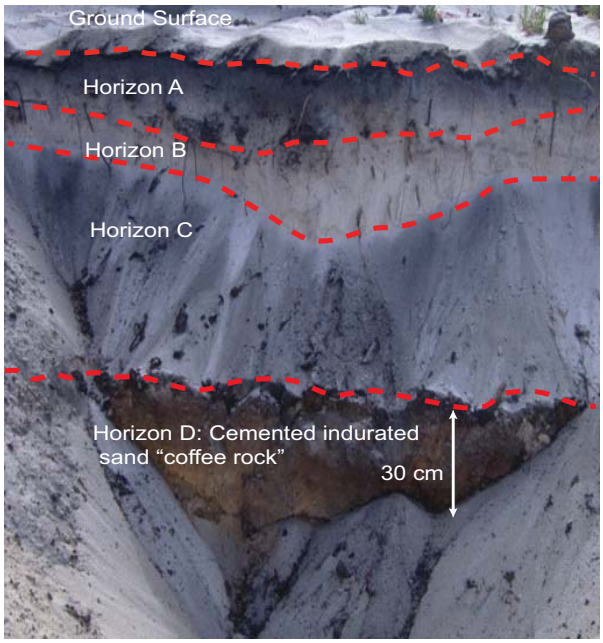

Figure 5-6. A photograph for the soil profile at Mirrabooka ASR site (Strobach, 2013). Note the four layers presented can be highly variable and in particular the cemented sands that are often called coffee-rock are patching and likely to impact on travel times. It is these near surface layers that are likely to be the cause of the statics error.

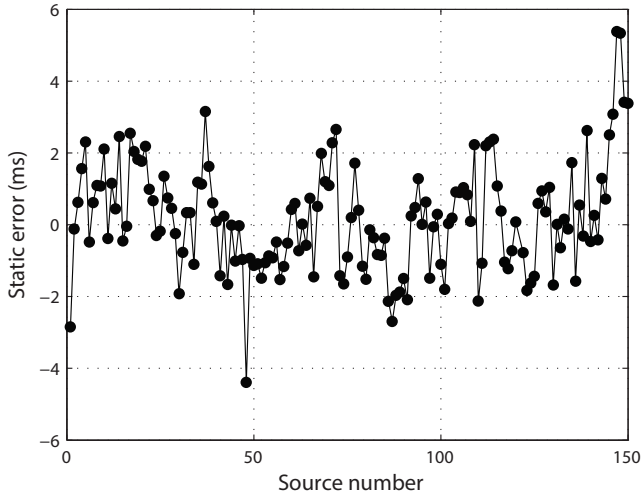

Figure 5-7. An example of travel time errors estimated from the field data (static) at each source position. These source statics affect the travel time information required for crosswell tomography.

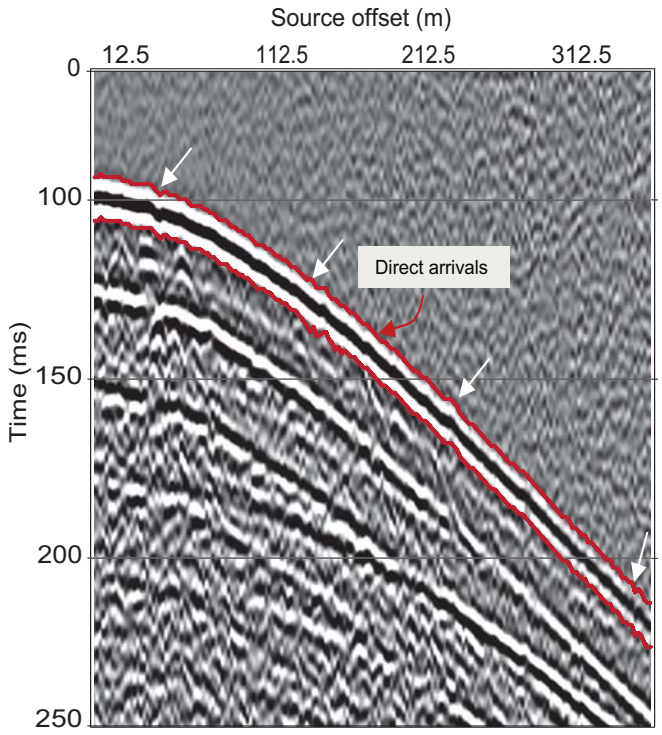

Figure 5-8. Synthetic common-receiver gather for a receiver at depth of 170 m. The red lines show the P-wave's first arrivals used for our VS computation, whereas the white arrows indicate the relative shift in travel time associated to near-surface effects.

As the VSM applied to vertical well pairs aims to create a virtual in-hole source, a reasonable cheque on the method is to forward compute the signal generated by an actual in-hole source and make a direct comparison with the signal coming from the virtual source. Figure 5-9 shows the comparison, i.e., at receiver position Rx1 shown in Figure 5-1, between the direct waves from both the retrieved VS (black traces) and the computed synthetic in-hole source (red traces). One can see that the first arriving pulses created from the virtual source and the synthetic in-hole sources are almost identical. The largest discrepancy in time and amplitude exists for near-horizontal source-receiver pairs (i.e. traces from 1 to 10 in Figure 5-9). This is because there is a finite surface source aperture such that the maximum in the travel time curve from the crosscorrelation cannot be reached as is a requirement for stationary phase. We

have excluded these near horizontal direct wave travel time information for tomographic inversion.

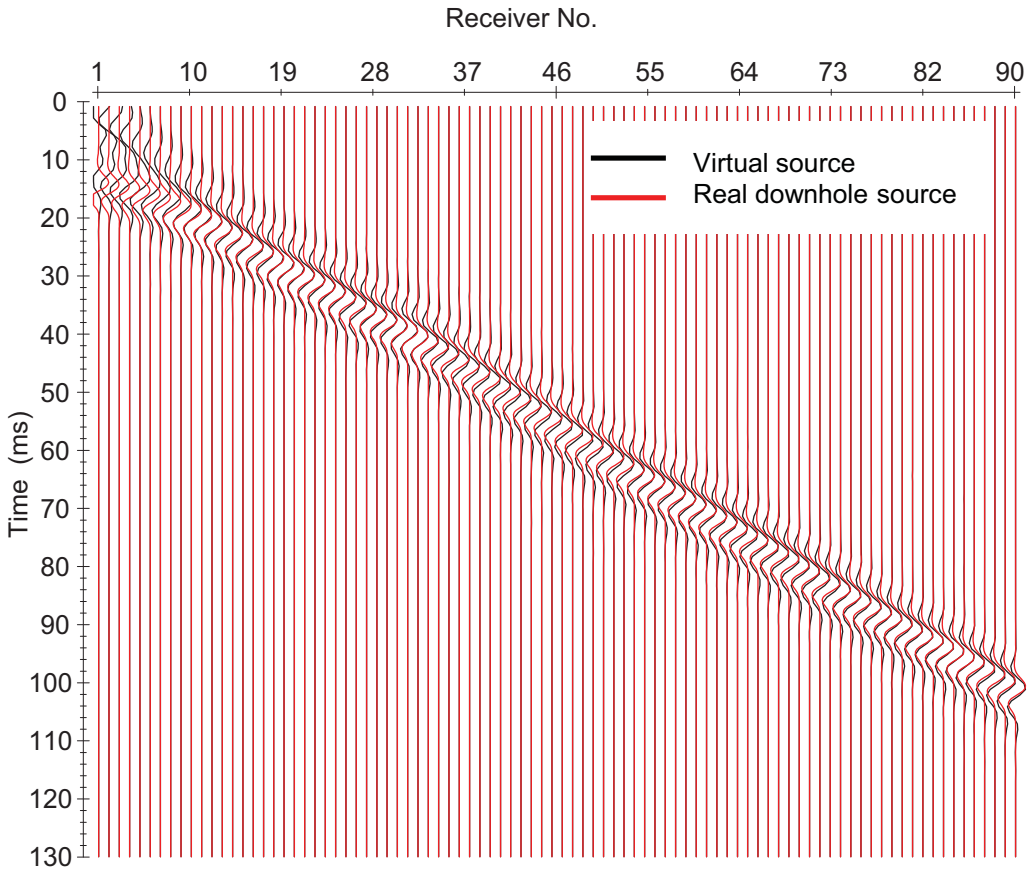

Figure 5-9. Comparison between the direct waves recovered from synthetic experiments of real (red) and virtual source (black).The direct arrivals are excited by in-hole source at Rx1 in well-109 and recorded by 90 receivers in well-408 (see Figure 5-1).

5.5 Results

5.5.1 Synthetic examples of virtual source crosswell tomography: the coarse-layered media

We selected different in-hole receiver spacings to investigate the impact of ray coverage on the accuracy of the VSCT velocities. First, we apply VSCT to the coarse-layered model. The surface source distribution and borehole configurations are shown in Figure 5-3a. All of the tomography results are compared to this original velocity model from depth 170 to 400 m. As stated earlier, all of the tomography presented commences with the same 2000 m/sec homogenous half-space as the initial model for inversion. We complete VSCT for receiver spacing of 2.5, 5, and 10 m. Raypath coverage diagrams and their associated apparent velocity are shown in Figures 5-10a, 5-10b and 5-10c. The apparent velocity is calculated from the virtual source travel times along a straight line between the in-hole VS source and the receiver. Figure 5-10a presents the case for closely spaced receivers of 2.5 m. For this configuration, there are 4005 down-going raypaths between the virtual source well on the left and the receiver well on the right. Note that even before inversion one can identify at least five layers L1, L2, L3, L4, and L5 with different ray apparent velocities in the raypath coverage diagram shown in Figure 5-10a.

Figures 5-11a, 5-11b and 5-11c show the tomographic inversion using a curved ray assumption for the coarse-layer model assigned with 2.5, 5 and 10 m receivers pair spacing, respectively. One can see that the velocity distribution remains consistent with model layers in Figure 5-11d even for a low ray coverage, i.e., at 10 m receiver spacing. This is because a sufficient number of rays pass between the wells from the virtual sources to the receivers for the thick layers to be resolved.

Figure 5-12 provides a comparison between the coarse-layer velocity model (black line) and the velocities obtained from VSCT with receiver spacings of 2.5 (red), 5 (green), and 10 m (blue) using a) straight and b) curved ray assumptions. The VSCT velocities are extracted along the vertical lines shown in Figures 5-11a, 5-11b, and 5-11c. There is an agreement between coarse-layer model velocities and the VSCT P-wave velocities. However, the curved ray computation shows more insight

to derive improved VSCT velocities, possibly because non-negligible deviation of the seismic ray properly handled using curved ray assumption. The VSCT velocities do tend to overshoot or undershoot at high-velocity contrast boundaries. Below 380 m, the VSCT velocities become unreliable due to the low ray coverage.

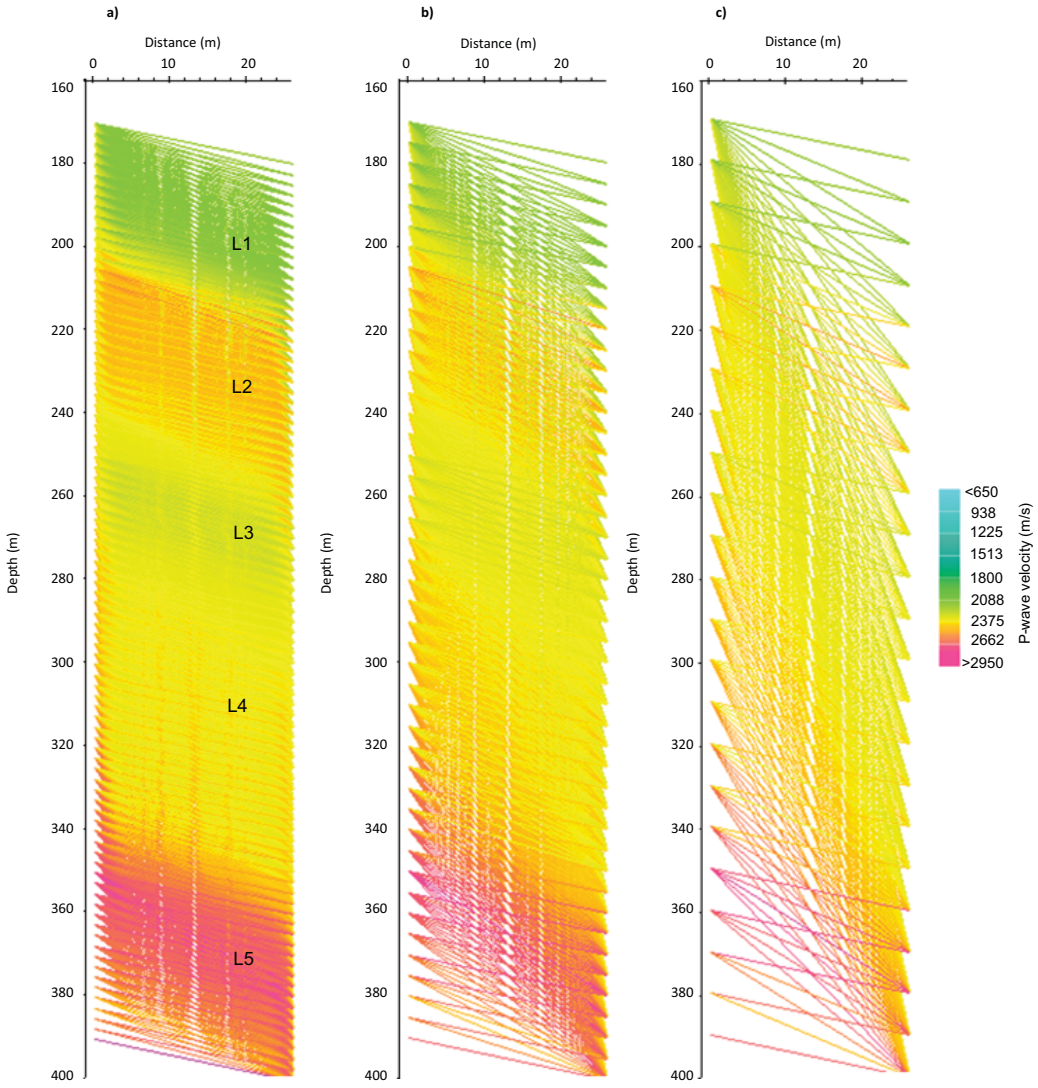

Figure 5-10. The raypaths coverage with colour corresponding to the apparent P-wave velocity for each ray. In panels (a, b, and c), the spacing between virtual sources on the left and the receivers on the right assigned with (a) 2.5, (b) 5, and (c) 10 m. The ray apparent velocity yield five layers L1, L2, L3, L4, and L5.

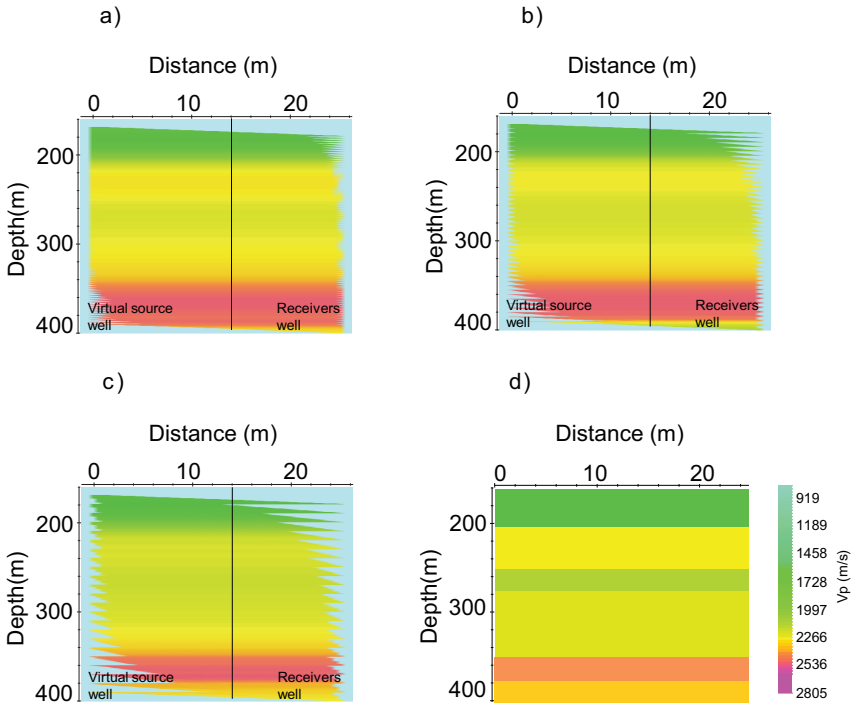

Figure 5-11. The synthetic VSCT results using the coarse-layered model, which are based on the ZVSP velocity measurements at the ASR trail site. Panels (a, b, and c) show the velocity distribution corresponding to the ray coverage in Figure 5-10. Panel d is the original synthetic model used to generate the virtual source. The lines in panels (a-c) show the area where the VSCT velocities were extracted.

Figure 5-13 shows misfit residuals for curved ray assumption presented in Figures 5-11a, 5-11b, and 5-11c. Residual of the travel times are computed from equation 5-2. The tomographic inversion using the high-density raypaths of 2.5 m receiver spacing converge at the lowest misfit of 1.5 ms as illustrated in blue line in Figure 5-13.

The significant outcome of the synthetic study using the coarse-layer model is that the original layering and their velocities are properly recovered by all receiver spacings. That is, for coarse sedimentary layers, a sparse receiver spacing may generate a reasonable velocity distribution from our VSCT with a relatively low ray density. Next, we consider VSCT applied to a model with thin layers.

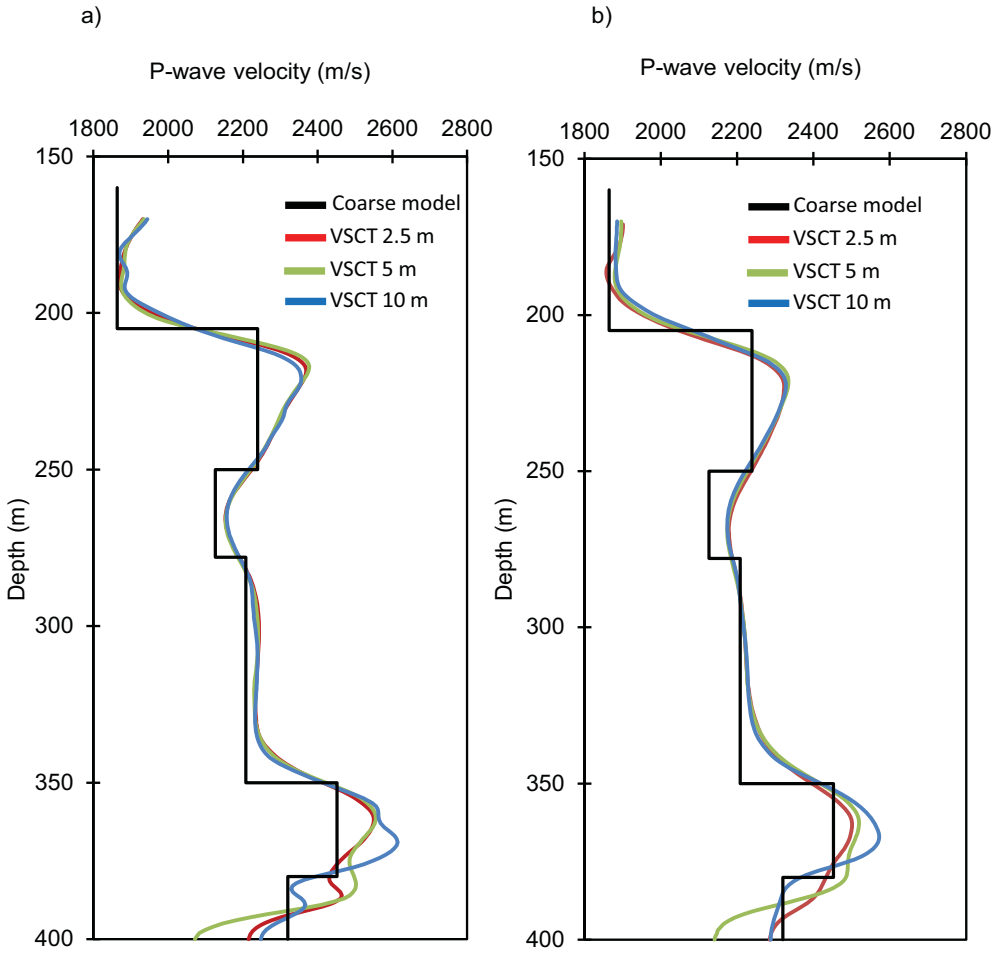

Figure 5-12. Comparison between the coarse-layer model velocities (black) and the VSCT velocities obtained by (a) straight line and (b) carved ray assumptions. The VSCT velocities are given for receiver spacings of 2.5 (red), 5 (green), and 10 m (blue). Given a homogenous initial model for inversion, the results of VSCT velocities agree with the coarse-layer model with some discrepancy at the deep section where low ray coverage area is existed.

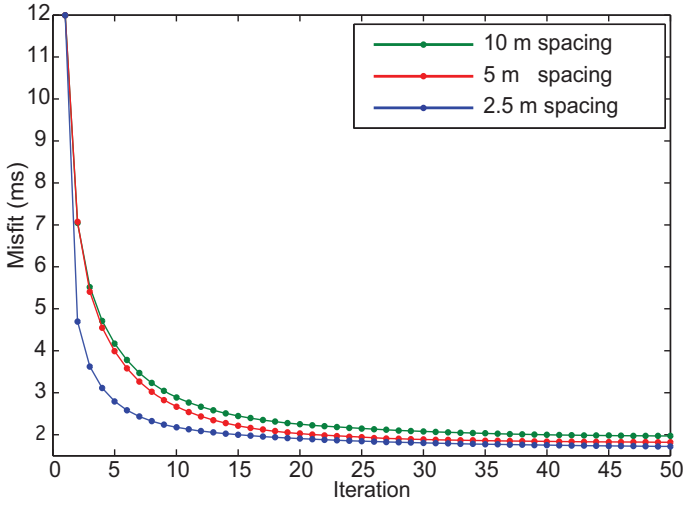

Figure 5-13. Travel time residuals versus the iteration for different receiver spacings of 2.5 (blue), 5 (red), and 10 m (green). The inversion using the higher-coverage raypaths of 2.5 m receiver spacing converge at the lowest misfit.

5.5.2 The accuracy of observed VS travel time using synthetic thin-layered model

We validate the synthetic travel times observed by our VSCT approach and compare how well the observed travel time agrees with the computed travel time if there were sources in the borehole. We generate actual crosswell experiments as if there were real sources in well M345-109.Then, the travel times for in-hole sources are computed with the finite-difference time-domain (FDTD) forward solver included in the ReflexW software package (Sandmeier, 2011). The computed travel times are then compared with the travel times observed in the VSCT approach. We determine the difference between the synthetic computed (i.e., synthetic crosswell experiment with the source actually in the borehole) and observed VSCT travel times for the thin-layered model configured with 2.5 m receiver spacing and plot the result in Figure 5-14a. The histogram in Figure 5-14b shows the distribution of the travel time differences between actual crosswell and VSCT experiments. One can see that the vast majority of the travel time differences are between +/- 1 ms. A positive travel time difference means that the computed travel time is larger than the observed

travel time, and vice versa. Higher travel time differences between computed and observed VSCT values are associated with areas where the seismic rays pass layers with large velocity contrasts illustrated by red cells in Figure 5-14a.

Figure 5-15 examines the impact of take-off angle on the accuracy of VSCT travel times. It shows the relationship between the travel time difference and take off angle. In Figure 5-15 travel time differences are given as a function of take-off angle through the colour scale associated to the depth of the virtual source. We found that the large differences between computed and observed travel times are mainly corresponding to large take-off angles (> 80°) as shown in Figure 5-15. Note that the large take-off angle in our case is corresponding to long travel path between both wells. Thus, the high travel time difference clearly relate to non-negligible deviation of seismic ray from straight line with distance**.** Furthermore, we note that the travel time difference clusters within +/- 0.5 ms in the range of take-off angles between 55° to 80°, however it is more widely spread toward more horizontal take-off angle of greater than 55°. The key point here is that the difference between computed in-hole source and VS travel time is small. Here we assume that the synthetic computed travel time from an in-hole source represents the ideal values of travel time. The difference is mostly less than +/-1 ms. Certainly this error is below travel time errors related to source statics that occur for a free-falling weight-drop source, even where the same shot locations are reoccupied. We again emphasise that the advantage of virtual source methods is greatest where the surface source line is located in highly heterogeneous near-surface conditions (e.g., the dry sands mixed with concretionary coffee rock zones in the Perth Basin).

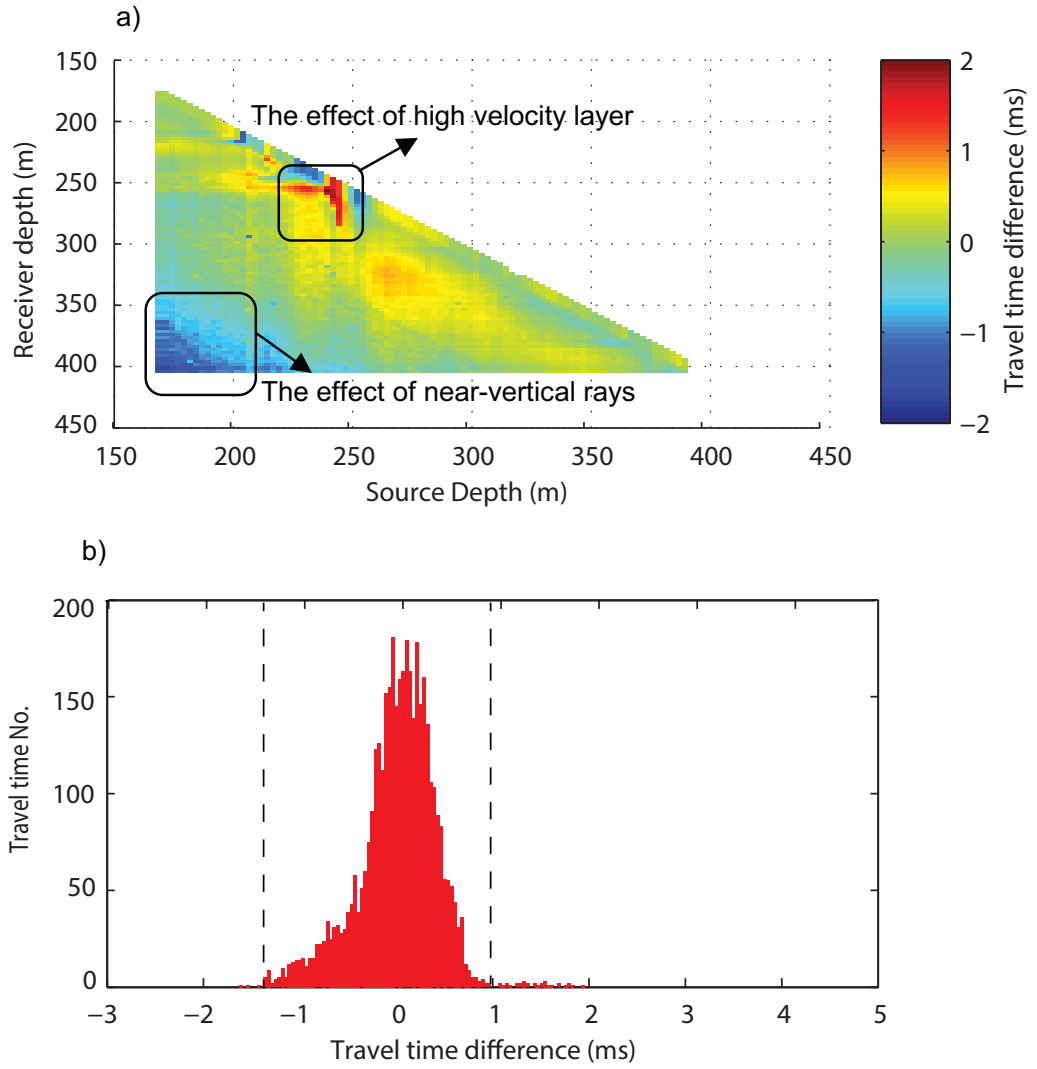

Figure 5-14. Travel time differences between computed (i.e. from computation with a synthetic in-hole source) and the observed VS travel times. (a) The travel time differences plot in colour scale for each source-receiver pair. The values of travel time differences larger than +/- 1 ms is associated with large velocity contrasts at 250 m depth. (b) A histogram for the distribution of travel time differences. The distribution of travel times differences is between +/- 1 ms (dash line).

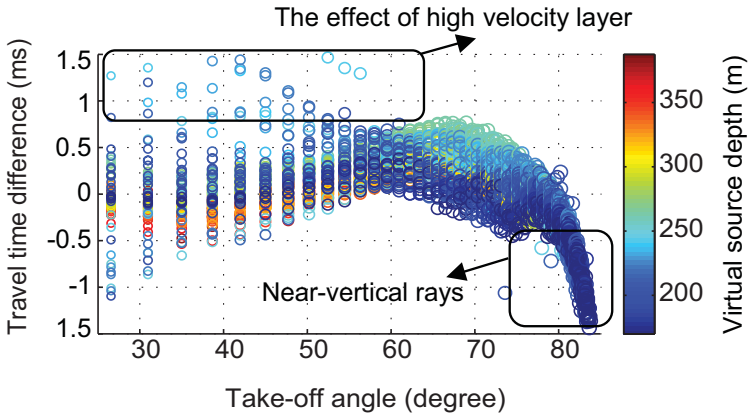

Figure 5-15. Ray take-off angles versus the travel time differences between the computed and observed travel times (also see Figure 5-14).

5.5.3 Synthetic examples of virtual source crosswell tomography: the thin-layered media

A second synthetic VSCT experiment was performed to establish the potential of VSCT for horizontal layered media containing thin layers. The thin-layer model is provided in Table 5-2. The surface source and borehole configuration are shown in Figure 5-3b. The synthetic experiment here is similar to that completed for the coarse-layer model but with different velocity and layers thickness from 170 to 400 m depth. Figure 5-16b, 5-16c and 5-16d shows the P-wave velocities obtained using curved ray tomographic inversion for the three receiver spacings of 2.5 m, 5 m and 10 m respectively. The velocities of the thin-layer model are provided in Figure 5-16a for comparison. In Figure 5-16b, we see that all the layers are resolved with a receiver spacing of 2.5 m, whereas in Figure 5-16c and 5-16d several thin layers are smeared or completely unrecovered. Additionally, as with the coarse-layer model, there is tendency to overshoot at the high- velocity contrast located at 212.5 m (i.e., L2).

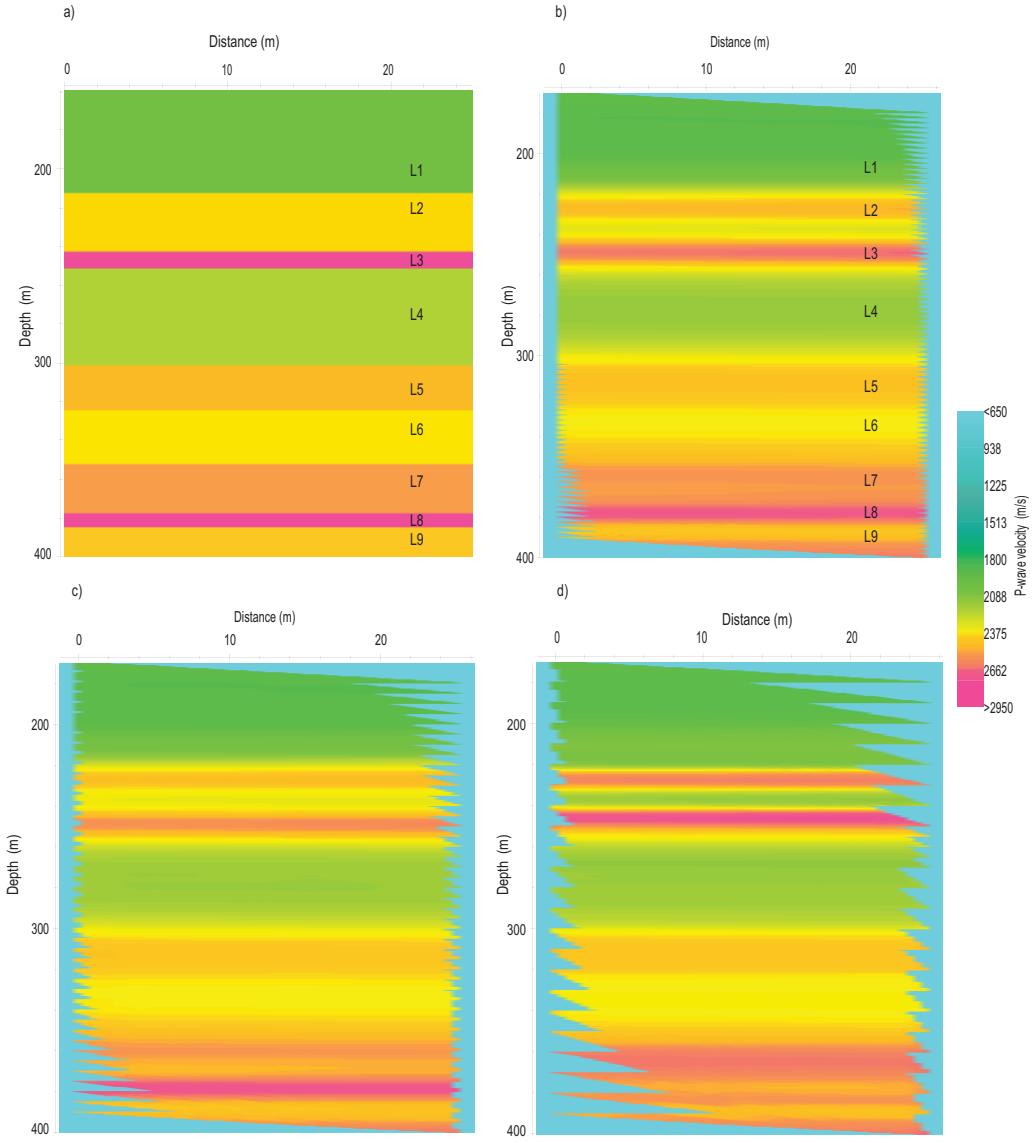

Figure 5-16. The P-wave velocity distribution obtained using synthetic VSCT for thin-layered model. (a) The synthetic model used to generate the virtual source gather. (b, c, and d) The velocity distribution corresponding to the three receiver spacings of 2.5, 5 and 10 m, respectively. The layers from L1 to L9 in the case of the 2.5 m receiver spacing are reasonably recovered.

5.5.4 Field experiment of virtual source crosswell tomography

A field experiment of VSCT was completed in two vertical monitoring wells at the Mirrabooka ASR site. The two wells are separated by 25 m. The study site is located approximately 15 km north of Perth city, Western Australia, as shown in Figure 5-17. These monitoring wells penetrate the Leederville aquifer at depths between 300 and 428 m below the surface (Rockwater Proprietary Ltd, 2009).

In this study, a walkaway VSP survey conducted using three repeated shots at 150 source locations along a 300 m straight line (i.e., 2 m source spacing). The seismic data is generated by a weight-drop source and recorded simultaneously by hydrophone strings deployed in two closely spaced wells, M345-109 and M345-408. Figure 5-18 shows photographs of the acquisition system, the monitoring boreholes, the hydrophone deployment and the weight-drop source. Sixteen hydrophones spanned depths from 170 to 320 m with 10 m hydrophone spacing in the well M345-109, and nine hydrophones distributed between 180 m and 340 m in the well M345-408. Figure 5-19a shows the geometry of the field experiment. Figures 5-19b and 5-19c display simultaneous common-receiver WVSP data recorded in well M345-109 and M345-408 respectively at depth of 180 m. The travel time error associated to complex near-surface is presented in Figure 5-7. Table 5-4 summarises the parameters used to acquire the field data. Figures 5-20a and 5-20b show flattened direct arrivals from the field experiment along with the frequency spectrum for a common depth gather for a receiver depth of 170 m in borehole M345-109. The signals spectral energy extends up to approximately 200 Hz. Note that the separation of the wavefields (up- and down-going P-wave, tube waves, converted S-wave) recorded in well M345-408 is a formidable task because the spare hydrophones spacing used in this well. This WVSP data requires sophisticated signal analysis to separate the wavefield for retrieving the reflection response.

Table 5-4. Acquisition parameters used in the VSCT field experiment.

Parameter	Value
Number of surface sources	150
Number of receivers	16 Hydrophones in well M345-109 and 9 Hydrophones in well M345-408.
Source spacing	2 m
Source type	800 kg weight-drop
Sample interval	0.25 ms
Receiver interval	10 m
Borehole spacing	25 m

Figure 5-17. Field photographs for the equipment and site layout taken during acquisition. (a) The test site, which consists of one injection borehole (M345-207) and five monitoring boreholes (i.e., M345-208, -108, -109, -308 and -408) (modified from Malajczuk, 2010). (b) Hydrophone string deployed into the well M345-109. (c) 800 kg drop source. (d) Borehole acquisition system.

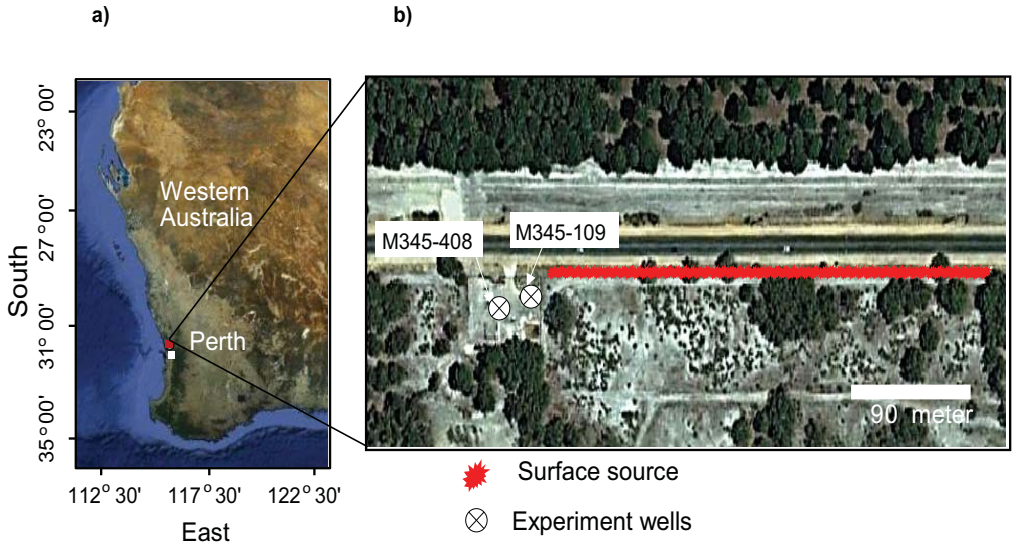

Figure 5-18. (a) A satellite view for ASR trail site. (b) The experiment monitoring wells M345-109 and M354-408 are a 25 m apart. Seismic waves were generated at 150 shot positions along a straight line with a 2 m spacing.

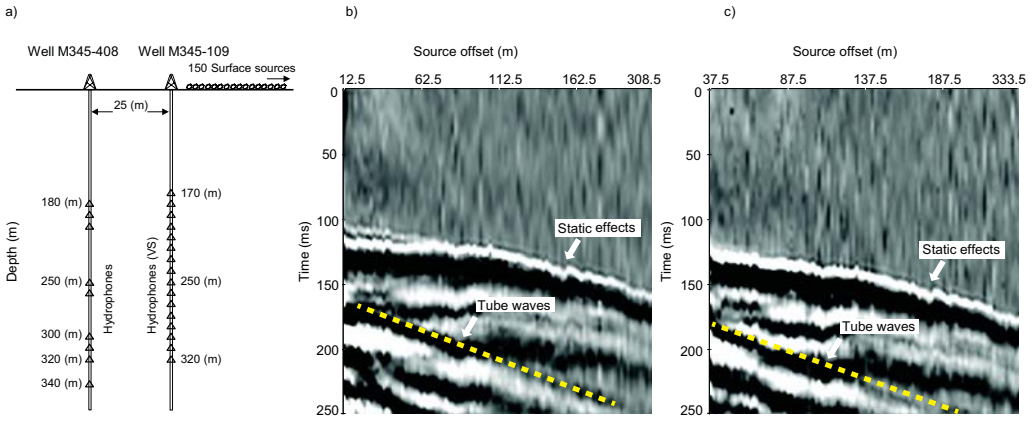

Figure 5-19. (a) The geometry of dual well WVSP field experiment. (b, c) Simultaneously common-receiver WVSP data recorded in well M345-109 and M345-408 at depth of 180 m, respectively. The source statics and tube waves are highlighted in both data sets. The separation of tube wave at well M345-408 is a challenge due to the spare hydrophones spacing.

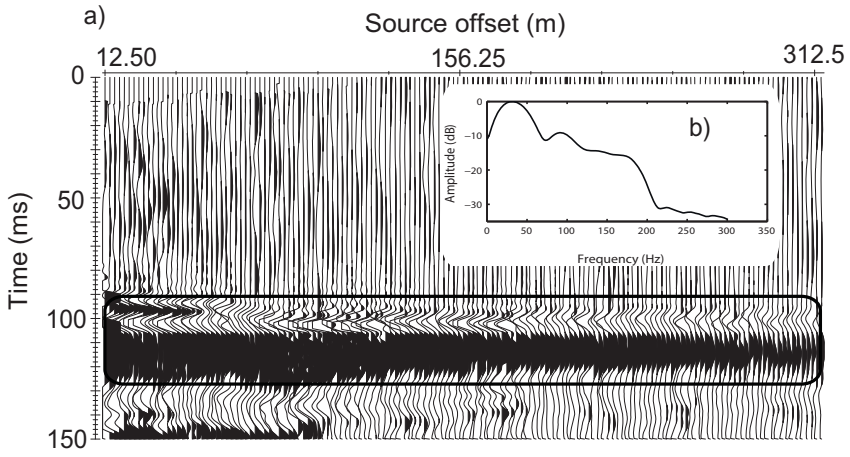

Figure 5-20. (a) Common-receiver gather for hydrophone in well M345-109 at depth of 170 m. The direct arrival is flattened at 100 ms. (b) The frequency spectra of the field data. The direct arrivals are indicated by box.

5.5.5 Virtual source crosswell tomography for field data

Once the direct arrivals are retrieved from virtual source computation, the peak on the VS traces are picked to provide the travel time for tomographic inversion. Figure 5-21 shows a crosswell receiver gather retrieved from VS computation for a receiver at 340 m depth in the well, M345-408. Figure 5-22a compares the vertical distribution of the velocity recovered from (i) the VSCT, (ii) the FWS logging and (iii) the ZVSP experiments in the well M345-109. The P-wave velocity distribution recovered from the field experiment of VSCT is presented in Figure 5-22b. The velocity distribution of VSCT is computed using a curved ray assumption. Seven layers are identified in VSCT result and labelled from L1 to L7 in Figure 5-22b. The horizontal continuity of the sedimentary layers between the monitoring wells M345-109 and M234-408 in Figure 5-22b is consistent with the previous study of wireline logging at the ASR site (Almalki et al., 2013). However vertical heterogeneity is extreme with rapid changes in rock type and seismic velocity.

In Figure 5-22b, the change in velocity at 190 m marks an important stratigraphic boundary between the Osborne and Leederville Formations. Below 190 m, the Pinjar Member of Leederville Formation extends to an approximate depth of 240 m. There is an increase in the velocity to a 10 m thick layer at the bottom of the Pinjar Member (L3 in Figure 5-22b). The Wanneroo Member of the Leederville Formation sits

below the Pinjar Member and consists of a sequence of relatively high velocity layers dominated by sand and siltstone. The discrepancy between the FWS, ZVSP and VSCT velocities in Figure 5-22a does not in any way imply that any of them are incorrect. As noted earlier, the FWS and ZVSP are acquired with two orders of magnitude difference in the dominant frequency. Furthermore, the FWS and ZVSP are clearly measures of the vertical P-wave velocity (or more correctly slowness) in a highly heterogeneous but horizontally layered media. In contrast, the VSCT velocities are a result of raypaths between two wells with take-off angles between 21° and 81°. For a horizontally layered medium, VSCT must include the influence of the horizontal component of the P-wave velocity. In this case, we expect that the VSCT-derived velocity will be higher (see Figure 5-22a). We suspect that analysis of anisotropy could be an important extension of VSCT. Certainly, for a VTI medium, it should be possible to recover the anisotropy parameters directly from the travel times derived from a combination of ZVSP and VSCT travel times; however, we leave this for future research.

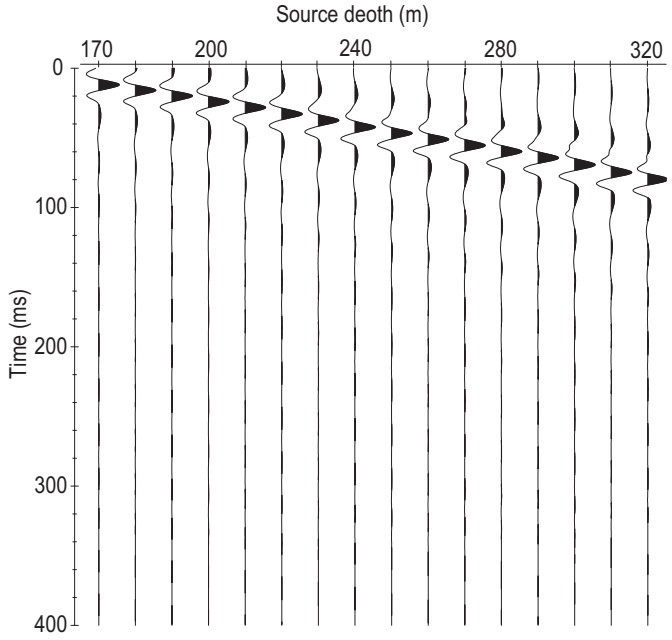

Figure 5-21. Field crosswell receiver gather retrieved from VS computation for a receiver at 340 m depth in monitoring well M345-408. The peak of the direct arrival is picked to provide the input travel times required for inversion.

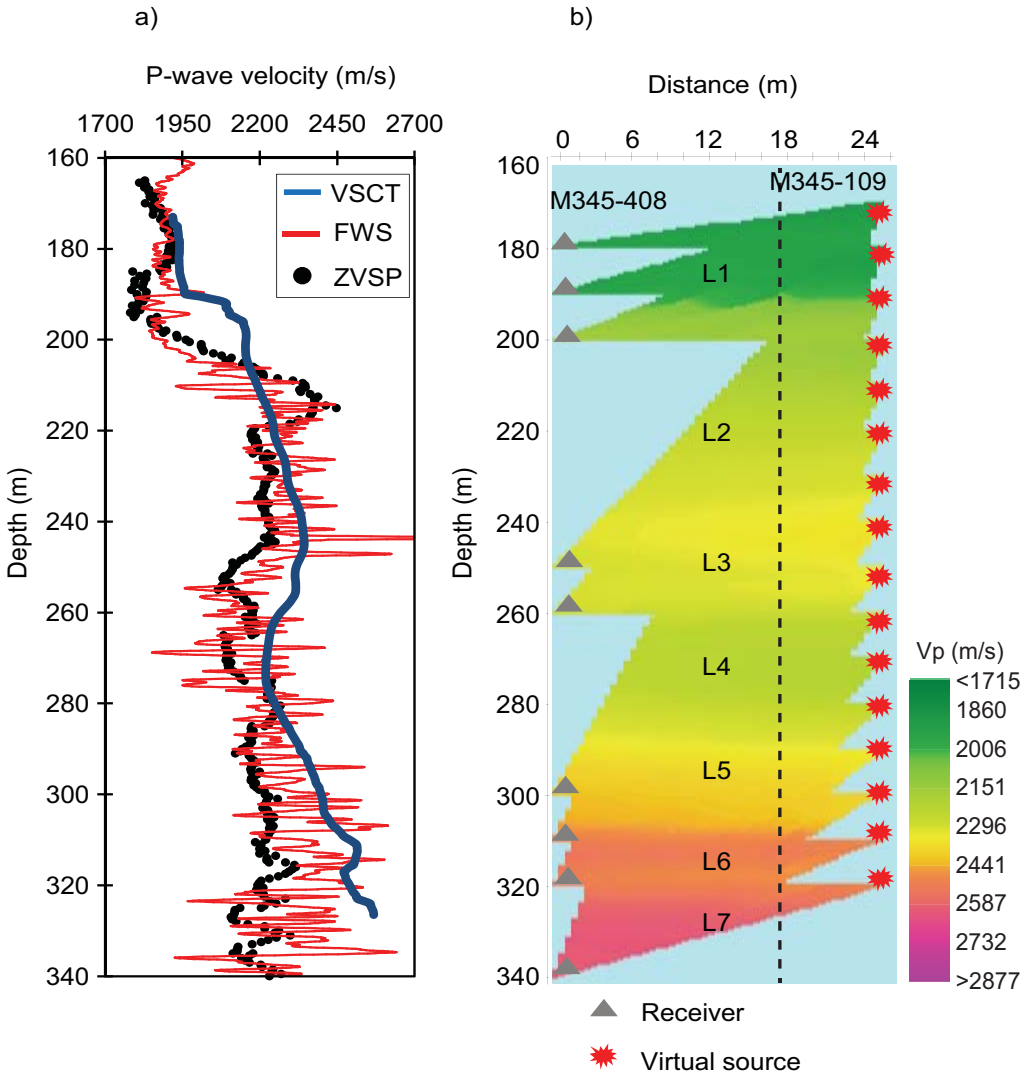

Figure 5-22. Comparison between the velocities derived from various in hole seismic surveys completed at the study site including (i) the ZVSP, (ii) the FWS logging and (iii) VSCT obtained. (a) The P-wave velocities calculated from the FWS logging (red), the ZVSP velocity (black), and the field VSCT (blue). (b) The P-wave velocity distribution obtained from VSCT field experiment computed using curved ray assumption.

To examine the validity of our VSCT field test, we obtain synthetic data identical to that used for the Mirrabooka field acquisition. That is, the field data and the synthetic data have identical ray coverage. Figure 5-23 provides the synthetic VSCT results using 81 down-going rays for tomography inversion. The synthetic survey is

completed over the thin-layer velocity model as previously shown in Figure 5-3b. Starting from homogenous initial velocity model, the velocity distribution between depths 170 to 340 m in the thin-layer model (Figure 5-23a) is reasonably recovered. A clear message from our studies is that, for VSCT, the accuracy that can be achieved in synthetic studies can often be replicated in field applications, even where there is extreme variability in the near-surface properties (e.g., extreme near-surface velocity statics).

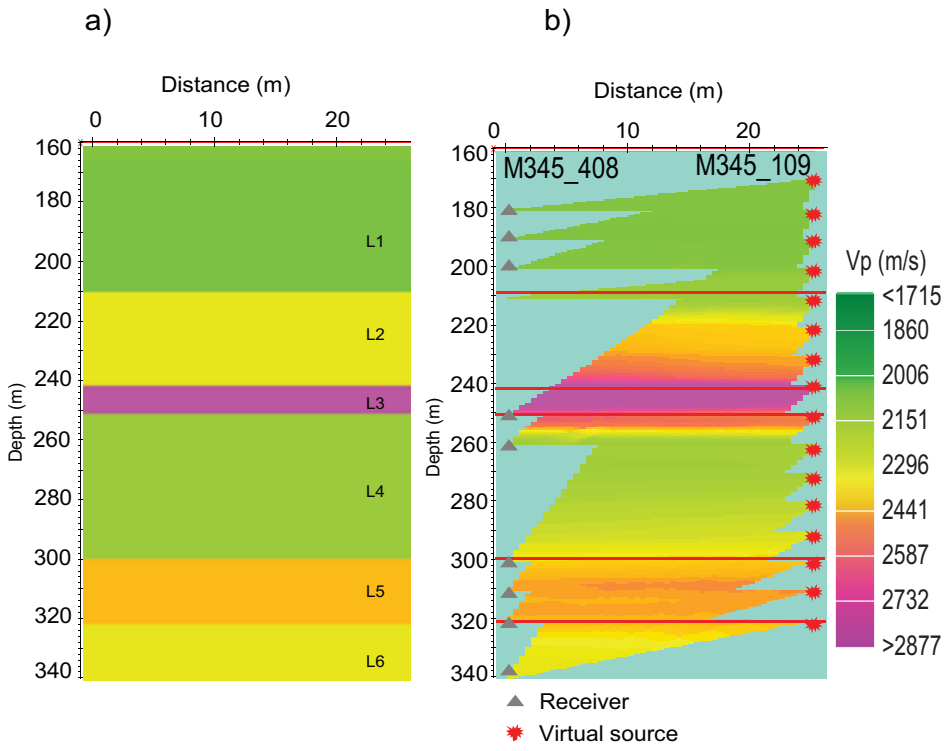

Figure 5-23. Synthetic VSCT experiment with ray coverage identical to the field experiment. (a) The thin-layer model used to generate the synthetic data. (b) The velocity information obtain from the synthetic VSCT experiment identical to the field experiment . The model layer marked as L1 ,L2, L3, L4, L5 and L6, are recovered by VSCT as indicated by the red lines.

5.5.6 The limitation and potential for the VSCT method

The application of VSCT to vertical well pairs may result in rays with a bias towards large take-off angle. This situation has the potential to result in a poor vertical resolution. Figure 5-24 provides a plot for the number of rays that pass each cell for our synthetic dual well WVSP survey (Figure 5-24a, 5-24b and 5-24c) and for the field dual well WVSP survey (Figure 5-24d). Figure 5-24a, 5-24b and 5-24c show the highest ray coverage in a diagonal between the shallowest source in the left and deepest receiver in the well since the only down-going rays are taken into account by the VSCT approach. In general, the field configuration has poor ray coverage with many cells being irregularly sampled in comparison to the synthetic survey configuration. The problem of low ray coverage in the VSCT can to some degree be assisted by application of a smoothing operator over a number of cells during inversion.

In this paper we have dealt exclusively with the first arriving pulse. We would note that producing full wavefield virtual shot records may be problematic especially where hydrophones are deployed in large diameters cased wells penetrating slow formations. In slow formations, the separation of the up-going and down-going wavefields required to generate the full wavefield virtual shot record is a formidable task. This is because large amplitude tube waves tend to mask reflections (Bois et al., 1972). For tomographic inversion, it is possible to isolate the direct arrival pulses by selectively muting the wavefield to leave only the first arrival P-wave for VS computations (Schuster et al., 2006). The effect of tube waves are even more significant in VSP surveys acquired in shallow formation because their origin is often from the shallow horizontally traveling waves such as surface waves (Bois et al., 1972).

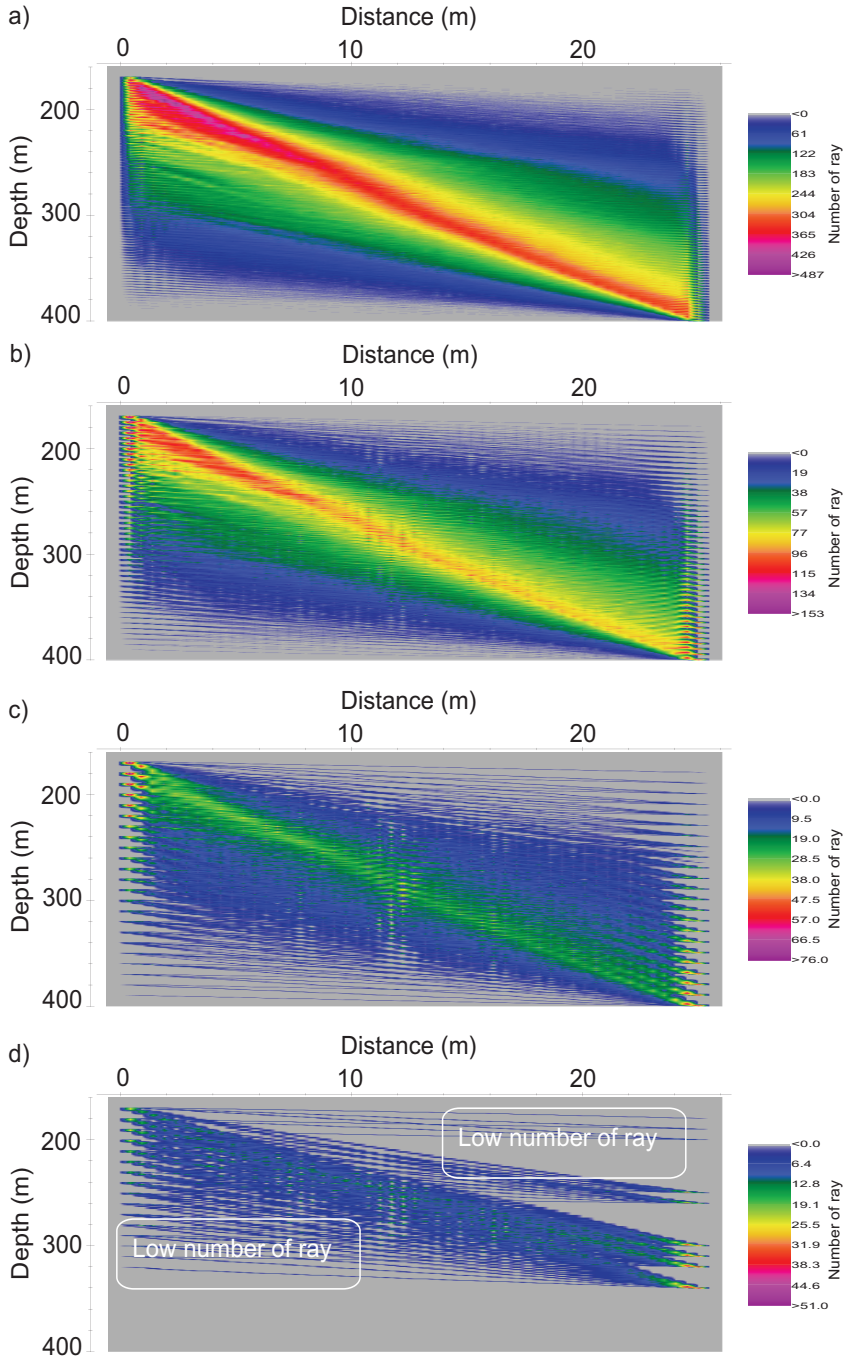

Figure 5-24. (a, b, and c) The number of ray cross each cell for the synthetic configurations run with receiver spacing of 2.5, 5, 10 m, respectively. (d) The number of ray in each cell for the field configuration. The field geometry has two low ray coverage areas (highlighted in boxes) caused by spare hydrophones spacing in well M345-408.

5.6 Conclusions

Groups of two or more closely spaced vertical wells (e.g., production and monitoring wells) are exceedingly common in hydrogeology and many forms of reservoir monitoring. Such arrangements present the possibility of applying crosswell technologies to investigate a range of earth properties between each well pair.

We use synthetic and field experiments to test VSCT in vertical well pairs. We stress that inversion methods based on the travel time difference between arbitrarily located subsurface receivers are not equivalent to our VSCT methods. Such inversion methods are only valid if the full volume of earth that may contribute to the travel time difference is incorporated in the inversion process. In contrast, the VSCT method recovers accurate travel times between receivers using virtual source computation. The obvious illustration of this point is that the creation of direct arrivals remains valid regardless of whether the first arriving wavefield originated from a surface source or from a strong diffraction below the source (e.g., a fault or near-surface boulder). Once the virtual source travel times are retrieved, these times provide input to tomographic inversion as if they were obtained from a real in-hole source.

We have considered the limitations and potential for the VSCT method in horizontal layer models. In general, we believe that receivers in the virtual source borehole can extend to the surface to achieve sufficient ray coverage. Also in most cases small in-hole receivers spacing should generate a highly acceptable result as shown in our synthetic experiments.

For the field example supplied, VSCT is combined with analysis of a dense ZVSP, to provide a high level of control over the velocities between well pairs. Our field experience is that the acquisition of dual well WVSP data does not require significant additional effort above what is required for conventional WVSP. The methods presented would be of considerable interest within the groundwater, geothermal, geotechnical and conventional/unconventional hydrocarbon industries.

5.7 References

Almalki, M., B. Harris, and J. C. Dupuis, 2012a, Stoneley wave dispersion in high permeability sandstone: Perth Basin, Western Australia: ASEG Extended Abstracts, 1-4.

Almalki, M., B. Harris, and J. C. Dupuis, 2012b, Numerical and field experiments for virtual source tomography, Perth Basin, Western Australia: ASEG Extended Abstracts, 1-4.

Almalki, M., B. Harris, and J. C. Dupuis, 2013, Multifrequency full-waveform sonic logging in the screened interval of a large-diameter production well: Geophysics, 78,10.1190/Geo2012-0328.1.

Bakulin, A., and R. Calvert, 2006, The virtual source method: Theory and case study: Geophysics, 71, SI139-SI150.

Blakeslee, S. N., and S. T. Chen, 1996, Method for simulating crosswell seismic data: Google Patents.

Bois, P., M. La Porte, M. Lavergne, and G. Thomas, 1972, Well-to-well seismic measurements: Geophysics, 37, 471-480.

Claerbout, J. F., 1968, Synthesis of a layered medium from its acoustic transmission response: Geophysics, 33, 264-269.

Descourvières, C., N. Hartog, B. M. Patterson, C. Oldham, and H. Prommer, 2010, Geochemical controls on sediment reactivity and buffering processes in a heterogeneous aquifer: Applied Geochemistry, 25, 261-275.

Granet, M., and J. Trampert, 1989, Large-scale P-velocity structures in the Euro-Mediterranean area: Geophysical Journal International, 99, 583-594.

Harris, B., C. Dupuis, M. Almalki, , Q. Li, M. Martin, and H. Prommer, 2010, Near Well Seismic Methods for Managed Aquifer Recharge: Perth Basin Western Australia: 7th Annual International Symposium on Managed Aquifer Recharge.

Humphreys, E., and R. Clayton, 1988, Adaptation of back projection tomography to seismic: J. geophys. Res, 93, 1073-1085.

Ivansson, S., 1983, Remark on an earlier proposed iterative tomographic algorithm: Geophysical Journal of the Royal Astronomical Society, 75, 855-860.

Kostyukevych, A., N. Marmalevskyi, Y. Roganov, and V. Tulchinsky, 2009, 3D–3C Full-Wave Modeling in Anisotropic 2..5 D Medium: CSEG CWLS Convention, Canada.

Kostyukevych, A., and Y. Roganov, 2010, 2.5 D Forward Modeling? a Cost Effective Solution that Runs on Small Computing Systems: ASEG Extended Abstracts, 1-4.

Kraus, M.J. 1999, Paleosols in clastic sedimentary rocks: their geologic applications. Earth-Science Reviews 47, 41-70.

Landmark Grapics, 1995, ProMax reference manual, Advance Geophysics Corp., Englewood, Colorado 80112.

Lowry, C. S., and M. P. Anderson, 2006, An assessment of aquifer storage recovery using ground water flow models: Ground water, 44, 661-667.

Malajczuk, S., 2010, Time-lapse thermal and induction logging in the near-well environment, Perth Basin WA: BSc thesis, Curtin University.

Mehta, K., A. Bakulin, J. Sheiman, R. Calvert, and R. Snieder, 2007, Improving the virtual source method by wavefield separation: Geophysics, 72, V79-V86.

Mehta, K., R. Snieder, R. Calvert, and J. Sheiman, 2008, Acquisition geometry requirements for generating virtual-source data: The Leading Edge, 27, 620-629.

Minato, S., T. Matsuoka, and T. Tsuji, 2013, Singular-value decomposition analysis of source illumination in seismic interferometry by multidimensional deconvolution: Geophysics, 78, Q25-Q34.

Minato, S., T. Matsuoka, T. Tsuji, D. Draganov, J. Hunziker, and K. Wapenaar, 2011, Seismic interferometry using multidimensional deconvolution and crosscorrelation for crosswell seismic reflection data without borehole sources: Geophysics, 76, SA19-SA34.

Peterson, J., B. Paulsson, and T. McEvilly, 1985, Applications of algebraic reconstruction techniques to crosshole seismic data: Geophysics, 50, 1566-1580.

Rockwater Pty Ltd, 2009, Mirrabooka aquifer storage and recovery trial: Bore completion and hydrogeological evaluation: Report no 236.20.4/09/01, Water Corporation.

Sandmeier, K., 2011, Windows™ 9x/NT/2000/XP/7-program for the processing of seismic, acoustic or electromagnetic reflection, refraction and transmission data, Manual for REFLEXW;3:1-177. (www.sandmeier-geo.de).

Schuster, G., M. Zhou, 2006, A theoretical overview of model-based and correlation-based redatuming methods: Geophysics, 71, SI103-SI110.

Strobach, E., B. D. Harris, J. C. Dupuis, A. W. Kepic, and M. W. Martin, 2010, Ground-Penetrating Radar for delineation of hydraulically significant layers in the unsaturated zone of the Gnangara Mound, WA: ASEG Extended Abstracts, 1-4.

Strobach, E., 2013, Hydrogeophysical investigation of water recharge into the Gnangara Mound: PhD thesis, Curtin University.

Schuster, G., J. Yu, J. Sheng, and J. Rickett, 2004, Interferometric/daylight seismic imaging: Geophysical Journal International, 157, 838-852.

Torii, K., K. Shiraishi, K. Onishi,, T.,Kimura,, S. Ito, T. Aizawa,, K. Tsukada, and T. Matsuoka, 2006, Cross-hole tomography using seismic interferometry: EAGE 68th Conference and Exhibition, A044.

Van der Sluis, A., and H. A. Van der Vorst, 1987, Numerical solution of large, sparse linear systems arising from tomographic problems, In: G. Nolet (Editor), Seismic tomography, Reidel, Dordrecht, 53-87.

Van der Neut, J., and A. Bakulin, 2008, The effects of time-gating and radiation correction on virtual source data: 75thAnnual International Meeting, SEG, Expanded Abstracts, 2922-2926.

Vasconcelos, I., and R. Snieder, 2008, Interferometry by deconvolution: Part 1—Theory for acoustic waves and numerical examples: Geophysics, 73, S115-S128.

Wapenaar, K., D. R. Draganov, X. Snieder, Campman, and A. Verdel, 2010, Tutorial on seismic interferometry: Part 1—Basic principles and applications: Geophysics, 75, 75A195-175A209.

Wapenaar, K., D. R. Draganov, and J. Robertsson, 2006, Introduction to the supplement on seismic interferometry: Geophysics, 71, SI1-SI4.

Zhou, H., 2006, First-break vertical seismic profiling tomography for Vinton Salt Dome: Geophysics, 71, U29-U36.

Zhou, M., and G. T. Schuster, 2000, Interferometric traveltime tomography: 70th Annual International Meeting, SEG, Expanded Abstracts, 2138–2141.

CHAPTER 6 : Conclusions

Slim-line borehole seismic tools are making the application of full waveform in-hole methods possible in a wide range of settings. My research explores new borehole seismic methods in complex and shallow borehole settings, where their full advantages may not previously have been recognised. For each new application, I worked through the full acquisition, processing and interpretation workflow, developing new ideas along the way. In particular, I investigated borehole applications in shallow high-permeability weakly consolidated (i.e., sometimes collapsing) formations. This thesis has presented new borehole seismic methods at different scales in shallow sands and sandstones with field examples from the Perth Basin, Western Australia.

One objective of my research was to investigate the application of FWS in the sand screened interval of a high-volume production well. My field experiments as described in Chapter 3 have demonstrated that multi-frequency full waveform sonic logging can indeed be effective in large diameter screened wells, and that new 3D phase velocity dispersion images can facilitate identification zones of higher permeability. That is, for sandstone intervals, the phase velocity dispersion characteristics of Stoneley and leaky P modes could often be empirically connected to hydraulic conductivity distribution. This sensitivity is seen at frequencies below 4 kHz.

In contrast, I showed that claystone-dominated formations are characterised by greater rates of change in phase velocity with frequency for both leaky P and Stoneley modes. The interpretation of 3D phase velocity dispersion images derived from different transmitted centre frequencies of 1 and 3 kHz revealed high repeatability of FWS in the production well. Direct comparison of dispersion images from an open drill hole with those derived from the large diameter production well showed dispersion images with similar characteristics for sand and claystone intervals. Although the shape of the phase velocity images in the open hole and production well were similar, there was an expected difference maxima of the phase velocity. There are several reasons for this difference, which can be related to differences in hole diameters in combination with the specific construction of the production well.

The most common product from a FWS survey is P-wave velocity from the first arriving pulse. However, even this common product may not be fully understood. In Chapter 4, I investigated factors affecting seismic P-wave velocity measured at different transmitted frequency in shallow, weakly consolidated sedimentary rocks in the Perth Basin. I first showed that P-wave velocity will vary slightly with changing of the transmitter frequency. That is, even the first arriving pulse of seismic energy may show the signs of different types of intrinsic and/or apparent dispersion. The repeated FWS experiments were completed at transmitter central frequencies of 1, 3, 5 and 15 kHz in an open hole that intersected weakly consolidated, highly heterogeneous friable sands and sandstone.

I mapped out empirical relationships between hydraulic permeability and P-wave velocity interpreted from logging completed with different transmitter centre frequencies for two general classes of sediment: (i) cross-bedded and (ii) non-cross-bedded sandstones. The empirical relationship was observed to be complex but clearly different for each of these sedimentary groups. This field-based research was not designed to prove or disprove rock physics models. Rather, it highlights the need to investigate the connection between P-wave dispersion and sedimentary structure in a controlled laboratory setting. For the practitioner, the research highlights the range of possible reasons why compression wave velocity expressed in the first arriving pulse may change or at least appear to change with frequency.

For any site where large volumes of fluid are injected or pumped from the subsurface, a crosswell tomogram may be highly useful as a constraint on the distribution of the mechanical and hydraulic properties within an ASR wellfield. I designed and completed simultaneous acquisition in two vertical wells to produce a dual well WVSP dataset with the information content necessary to simulate crosswell tomography. In Chapter 5, I described the methods necessary for recovering crosswell velocity distribution between vertical wells without the need for a downhole source. I validated the method with synthetic dual well WVSP data derived from an earth model based on the velocity distribution recovered from detailed zero-offset VSP and FWS experiments at the field site. These synthetic examples highlight the potential of virtual source crosswell tomography where large numbers of close-spaced receivers can be deployed to multiple wells. The final velocity distribution recovered from the field data was highly consistent with what

was expected from sonic logging and ZVSP. The virtual source crosswell travel times are useful to place a constraint on the velocity between vertical wells, as the velocity is determined from the highly accurate cross-correlated travel times.

The techniques that I have presented would be highly suitable for time-lapse applications in high-volume production wells. The methods presented are highly repeatable borehole seismic methodologies that can be applied at any point in the life of a well, without affecting the near well setting. A key driver for this research was expanding borehole seismic applications for groundwater, with a particular emphasis on aquifer storage and recovery sites. However, the research presented would also find value and application within geothermal, geotechnical, hydrocarbon and minerals industries.

6.1 Recommendations for future research

I have successfully presented the first field-based experiments for the application of multifrequency full waveform sonic logging in the sand screened interval of a large diameter production well. This thesis has considered possible reasons for variations in velocity and in particular, considered possible relationships between apparent dispersion of P-wave velocity, hydraulic permeability and broad divisions between sedimentary structures. It has detailed a new workflow demonstrating both field design and processing for virtual source crosswell tomography between vertical wells.

Based on the field experiments conducted in this study, I would suggest the fallowing investigation for future research:

- **The sensitivity of FWS modes to formation properties:**
  - I have found that the FWS dispersion images are effective for lithological discrimination, and the phase-velocity at different frequencies ranged from 2 kHz to 4 kHz could be empirically related to hydraulic conductivity where logging was in a large diameter production well and completed with stainless-steel sand screens. However, the relationships represent a starting point from which empirical and possibly later robust numerical relationships can be

established at some future time. Thus, to describe the wave propagation spanning several modes for the specific ASR well used in this study, I would likely need to obtain either a new formulation or a significant adaptation of the existing algorithms.

- **The analysis of FWS dispersion images:**
  - I have found that for several phase-velocity dispersion images in the M345-207 production well, there are small high-energy zones in the transition between low- and high-frequency modes. These transitions do not occur in the dispersion images for the open-hole M345-109. Two possible explanations have been given: the development of well annulus and the poor coupling between the formation and the wire-wound sand-screens. I suggest that new systematic field scale studies will need to be done to reveal the complex relationship between well completion and FWS wireline logs.

- **The characteristics of the first-arriving pulse (P-wave) acquired with different transmitter centre frequencies:**
  - There is some degree of dispersion evidence for the P-waves acquired at different transmitter centre frequencies. Instead of measuring the apparent dispersion, I would suggest investigating the effects of frequency-dependent attenuation or any changes in the frequency content of P-waves, then correlating the results with the permeability measurements.

  - The observation of the apparent negative dispersion may also associate with the attenuation of different frequencies, wavelengths and thicknesses of thin layers. It is expected that the effect of these factors on negative dispersion observed within the receiver set used for analysis could only be fully understood with physical or numerical modeling.

- **Alternative approach to virtual source crosswell tomography:**
  - In the analysis of virtual source crosswell tomography VSCT, I dealt exclusively with the first-arriving pulse. However, an interesting alternative approach to the virtual source method that I proposed would be to use up-

going waves generated from reflections and/or diffractions to create a new set of upward-looking virtual sources. The problem with this concept would be isolating the up-going P-waves from the down-going waves and the other borehole modes within the wave train.

- I suspect that the analysis of anisotropy could be an important extension of VSCT. Certainly, for a VTI medium, it should be possible to recover the anisotropy parameters directly from the travel times derived from a combination of ZVSP and VSCT; however, I leave this for future research.

Appendix

Copyright Release Information

Every reasonable effort has been made to acknowledge the owners of copyright material. I would be pleased to hear from any copyright owner who has been omitted or incorrectly acknowledged.

Fwd: Permission

Ted Bakamjian <Tbakamjian@seg.org>

Tue 8/10/2013 8:12 PM

To:Majed Ahmed Almalki <m.almalki3@postgrad.curtin.edu.au>;

Cc:Jennifer Cobb <jcobb@seg.org>;

Dear Majed,

You have SEG's permission to use the Geophysics article you authored in your thesis. Please identify SEG as the copyright owner, and please provide a permalink to the SEG version of the article with republication:

http://dx.doi.org/10.1190/geo2012-0328.1

Best of luck with your thesis. Thank you for publishing in Geophysics.

Sincerely,

Ted

Ted Bakamjian
Director, Publications
Society of Exploration Geophysicists
P. O. Box 702740, Tulsa, OK 74170-2740 USA
Shipping: 8801 S. Yale Ave., Suite 500, Tulsa, OK 74137
Phone: (918) 497-5506; Fax: (918) 497-5557
E-mail: tbakamjian@seg.org; Web: http://www.seg.org/

Majed Almalki <malmalki@gmail.com>

RE: Elsevier.com permissions query

1 message

Permissions Helpdesk <permissionshelpdesk@elsevier.com> Fri, Nov 1, 2013 at 3:13 AM
To: "malmalki@gmail.com" <malmalki@gmail.com>

Dear Majed:

Permission is covered by the rights you retain as an Elsevier journal author as outlined at http://www.elsevier.com/journal-authors/author-rights-and-responsibilities, which include Inclusion in a thesis or dissertation, provided that proper acknowledgement is given to the original source of publication. Should you require any further clarification, please let me know. Best of luck with your thesis.

Regards,
Hop

Hop Wechsler
Permissions Helpdesk Manager
Global Rights Department
Elsevier
1600 John F. Kennedy Boulevard
Suite 1800
Philadelphia, PA 19103-2899
Tel: +1-215-239-3520
Mobile: +1-215-900-5674
Fax: +1-215-239-3805
E-mail: h.wechsler@elsevier.com
Questions about obtaining permission: whom to contact? What rights to request?
When is permission required? Contact the Permissions Helpdesk at:
. +1-800-523-4069 x 3808 . permissionshelpdesk@elsevier.com

-----Original Message-----
From: Elsevier Customer Service [mailto:noreply@elsevier.com]
Sent: Wednesday, October 30, 2013 12:06 AM
To: Permissions Helpdesk
Subject: Elsevier.com permissions query

RightNow Reference Number: 131030-000610

First Name: Majed
Last Name: AlMalki
Email Address: malmalki@gmail.com
Customer Type: Individual
Website: Elsevier.com
Country: AU
Customer Supplied Reference Number: APPGEO 2352
Subject Level 1: Permissions and Legal

Re: Permission

Mark Lackie <mark.lackie@mq.edu.au>

Wed 9/10/2013 11:04 AM

To:Majed Ahmed Almalki <m.almalki3@postgrad.curtin.edu.au>;

Hi Majed,
that is fine.

cheers

Mark

On 8 October 2013 22:19, Majed Ahmed Almalki <m.almalki3@postgrad.curtin.edu.au> wrote:

Dr Mark Lackie
Senior Lecturer in Geophysics
Department of Earth and Planetary Sciences
Macquarie University
North Ryde NSW 2109
Ph 61-2-98508377 Mob 0425237899
Fx 61-2-98506904
Building E7A Room 514

CRICOS Provider Number 00002J

Please consider the environment before printing this email.

This email (including all attachments) is confidential. It may be subject to legal professional privilege and/or protected by copyright. If you receive it in error do not use it or disclose it, notify the sender immediately, delete it from your system and destroy any copies. The University does not guarantee that any email or attachment is secure or free from viruses or other defects. The University is not responsible for emails that are personal or unrelated to the University's functions.

Dear Dr Mark

I am a PhD student at Curtin University in Australia and I am planning to include in my thesis the manuscript EG 13037, entitled 'Apparent P-wave velocity dispersion in shallow high-permeability sandstones', which I submitted to Exploration Geophysics for publication. I am in the progress to respond to the comments of the reviewers. However, in order to include this work in my thesis, I would like to ask your permission to do so.

Thank you very much and appreciate your help.

Best regards

Majed